VIBRATION ATTENUATION FOR HIGH-SPEED TRAINS USING MAGNETORHEOLOGICAL (MR) DAMPERS

SHUQIN YE

PhD

The Hong Kong Polytechnic University

2017

The Hong Kong Polytechnic University

Department of Civil and Environmental Engineering

VIBRATION ATTENUATION FOR HIGH-SPEED TRAINS USING MAGNETORHEOLOGICAL (MR) DAMPERS

Shuqin Ye

A thesis submitted in partial fulfillment of the requirements

for the Degree of

Doctor of Philosophy

January 2017

CERTIFICATE OF ORIGINALITY

I hereby declare that this thesis is my own work and that, to the best of my knowledge and belief, it reproduces no material previously published or written, nor material that has been accepted for the award of any other degree or diploma, except where due acknowledgement has been made in the text.

______________________________ (Signed)

Shuqin Ye ____________________ (Name of Students)

To my parents

ABSTRACT

The past two decades witness the rapid expansion of high-speed rail. However, as the rail service experiences a step-change increase in operating speeds, the vehicle vibration response, especially in the lateral direction, become more important. The subject of vibration mitigation for high-speed train has been under studied for many years. Modern control theory and advanced actuator technology enables the train suspension to consider a wide variety of innovative possibilities. More recently, magnetorheological (MR) damper emerges as a promising semi-active actuator for vibration control for high-speed trains. This research focuses on advanced secondary suspension for high-speed train using MR dampers in the interest of lateral ride comfort improvement.

Firstly, an experimental study on incorporating MR damper in a secondary suspension is conducted. The rail vehicle in tests is full-scale carriage of high-speed train CRH3 electric multiple unit (EMU). Three types of MR dampers with different control force range are designed, fabricated, and incorporated into the EMU secondary suspension, to account for the lateral vibration mitigation. The integrated vehicle is tested at speeds in a wide range, with random track irregularities. The performance of the MR suspension is tuned by a driven current switching between passive-off and passive-on states. The dynamic behaviour of the integrated vehicle system and the ride comfort at each state is evaluated, and thus the potential of the MR suspension is demonstrated.

Secondly, according to the previous rolling-vibration experiment results, a new type of MR damper with more suitable control force range is selected to replace the lateral damper of high-speed train secondary suspension. The dampers are equipped with strain gauge for force sensing and LVDT for displacement motion sensing. The modelling of the new dampers is conducted. A viscoelastic-plastic (VEP) based model which is only current dependent is employed to represent the dynamic characteristics of the MR dampers. However, the dynamics of the MR dampers obtained through a MTS test system shows that the damper response is related not only to the applied current (or magnetic strength), but to the frequency and displacement amplitude, or rather the velocity amplitude. Therefore, an enhanced model that consists of ten parameters is ultimately formulated to characterize the inherent nonlinear hysteresis of the MR dampers. In addition, since the governing equations explicitly contain the applied current to the damper, the inverse model which expresses the relationship between the command current and the desired damper force can be devolved directly from the forward model.

Thirdly, the effectiveness of negative stiffness superimposed with simple damping models for vehicle vibration mitigation is interpreted by examining the negative stiffness component incurred in the skyhook damping. The negative stiffness tends to increase the damper motion, thereby facilitating the energy dissipation. Therefore, it is straightforward to impose a negative stiffness component into a vehicle system in an effort to mitigate the unwanted vibration of the car body. A negative stiffness with viscous damping and friction damping is emulated by the MR damper respectively. It is should be noted that, the MR damper is a semi-active device that cannot produce fully active control forces. The lower force bound of the MR damper is identified, and then compiled to the damper controller to emulate the unclipped negative stiffness and the clipped negative stiffness, respectively. Then, a fifteen degree-of-freedom model for the high-speed train EMU is established in MATLAB SIMULINK. The model consists of four wheelsets and two trucks which are characterized by lateral and yaw motions respectively, and a car body represented by lateral, yaw and roll motions. The model is used to reproduce the lateral vibration response of the car body of the vehicle subjected to the random track irregularities. Three suspensions, i.e., passive suspension with existing hydraulic dampers, MR suspension with emulated negative stiffness with viscous damping (NSV, or semi-active skyhook damping) and MR suspension with emulated negative stiffness with friction damping (NSF), are integrated with the vehicle model, and evaluated for the vibration mitigation performance. The simulation result shows that, the suspensions with negative stiffness component show significant capability in increasing damper motions.

PUBLICATIONS arising from the thesis

Journal Papers

Ni, Y.Q., **Ye, S.Q.**, and Song, S.D. (2016), "An experimental study on constructing MR secondary suspension for high-speed trains to improve lateral ride comfort", *Smart Structures and Systems*, Vol. 18, No. 1, 53-74. (SCI)

Ying, Z.G., Ni, Y.Q., and **Ye, S.Q.** (2014), "Stochastic micro-vibration suppression of a sandwich plate using a magneto-rheological visco-elastomer core", *Smart Materials and Structures*, Vol. 23, No. 2, Paper No. 025019 (11pp). (SCI)

Li, Z.J., Ni, Y.Q., Dai, H.Y., and **Ye, S.Q.** (2013), "Viscoelastic plastic continuous physical model of a magnetorheological damper applied in the high speed train", *Science China: Technological Sciences*, Vol. 56, No. 10, 2433-2446. (SCI)

Ye, S.Q., and Ni, Y.Q. (2012), "Information entropy based algorithm of sensor placement optimization for structural damage detection", *Smart Structures and Systems*, Vol. 10, No. 4-5, 443-458. (SCI)

Ying, Z.G., Zhu, W.Q., **Ye, S.Q.**, and Ni, Y.Q. (2011), "An accurate substructural synthesis approach to random responses", Structural Engineering and Mechanics, Vol. 39, No. 1, 47-75. (SCI)

Conference Papers

Ye, S.Q., Ni, Y.Q., and Li, Z.J. (2014), "A semi-active rail vehicle suspension incorporating negative stiffness emulated by magnetorheological (MR) damper", *Proceedings of the 6th World Conference on Structural Control and Monitoring*, 15-17 July 2014, Barcelona, Spain.

Ye, S.Q., and Ni., Y.Q. (2013), "Structural health monitoring of hanging gears for DC-3 aircraft on display at The Hong Kong Science Museum", *Proceedings of the 6th International Conference on Structural Health Monitoring of Intelligent Infrastructure*, 9-11 December 2013, Hong Kong.

Ye, S.Q., and Ni, Y.Q. (2011), "Information entropy-based algorithm of sensor placement optimization for structural damage detection", *Proceedings of the 8th International Workshop on Structural Health Monitoring*, 13-15 September 2011, Stanford, California, USA.

ACKNOWLEDGEMENTS

I would like to express my sincere gratitude to my supervisor, Professor Y. Q. Ni, for providing me with the unique opportunity to pursue my PhD degree. I have learned much from his creative thinking, hard-working and always try-to-be-perfect attitude. All of these will be beneficial my future professional life. I would like to thank my co-supervisor, Prof. W. H. Li, from University of Wollongong, Australia, for their generous support in my research.

Gratitude goes to Professor Z. G. Ying in Zhejiang University, China, who was my supervisor when I studied for a Master degree, for his recommendation that I could study in Hong Kong and the constructive advice during the course of my PhD study.

Special appreciations are given to all the colleagues and friends I have met in the University. In particular, I would like to extend my heartfelt gratitude to Dr. Z. H. Chen, Dr. X. H. Zhang, Dr. W. Lin and Dr. J. Li for their consistent friendship, support and experience sharing, which enrich my life in Hong Kong.

My thanks also go to my beloved family. It is their love that makes it happen.

I would like to dedicate this work to my parents for their sustained love, encouragement and support. I shall be more obliged to all of them than I can express, yet I know that this achievement will fill them up with sincere happiness.

Finally, the financial supports from The Hong Kong Polytechnic University are gratefully acknowledged.

TABLE OF CONTENTS

LIST OF FIGURES

Figure **Description** **Page**

LIST OF TABLES

LIST OF SYMBOLS

Symbol	Description
Chapter 3	
a_{XP}	RMS values of the accelerations obtained at the measured point in the longitudinal direction
a_{YP}	RMS values of the accelerations obtained at the measured point in the lateral direction
a_{ZP}	RMS values of the accelerations obtained at the measured point in the vertical direction
W_d	Horizontal frequency weighting
N_{MV}	Lateral component of ride comfort
Chapter 4	
k	Stiffness in the pre-yield region
c	Viscous damping coefficient in the post-yield region
f_c	Yield force
d_1, d_2	Positive constant delivering the linear rise of yield force
f_0	Offset
α	Scale factor that determines the pre-yield hysteresis slope
α_0, α_1	Positive constant adjusting the decreasing curve α
v_m	Maximum velocity
i	Current command of MR damper
Chapter 5	
2-DOF quarter car	
m_s, m_u	Mass of sprung mass and unsprung mass
x_s, x_u	Displacement of sprung mass and unsprung mass
$\dot{x}_s$, $\ddot{x}_s$	Velocity and acceleration of sprung mass
$\dot{x}_u$, $\ddot{x}_u$	Velocity and acceleration of unsprung mass
x_t	Track irregularities
f_{des}	Desired control force of MR damper
f	Actual control force of MR damper
c_p	Primary suspension damping of quarter car
c_{sh}	Skyhook damping
c_{nsv}	Viscous damping component of emulated negative stiffness with viscous damping
c_{nsf}	Friction damping component of emulated negative stiffness with friction damping
k_s, k_p	Secondary suspension stiffness and primary suspension stiffness of quarter car
k_{nsv}	Stiffness component of emulated negative stiffness with viscous damping

k_{nsf}	Stiffness component of emulated negative stiffness with friction damping

15-DOF full-scale vehicle model

m_c	Mass of car body
m_{t1}, m_{t2}	Mass of front truck and rear truck
m_{w1}, m_{w2}	Mass of front truck leading and trailing wheelset
m_{w3}, m_{w4}	Mass of rear truck leading and trailing wheetset
I_{cz}, I_{cx}	Inertia moment of car body
I_{t1}, I_{t2}	Inertia moment of front and rear truck
I_{w1}, I_{w2}	Inertia moment of front truck leading and trailing wheelset
I_{w3}, I_{w4}	Inertia moment of rear truck leading and trailing wheetset
y_c	Lateral translational motion of car body
φ_c	Yaw motion of car body
θ_c	Roll motion of car body
y_{t1}, y_{t2}	Lateral translational motion of front and rear truck
φ_{t1}, φ_{t2}	Yaw motion of front and rear truck
y_{w1}, y_{w2}	Lateral translational motion of front truck leading and trailing wheelset
y_{w3}, y_{w4}	Lateral translational motion of rear truck leading and trailing wheelset
F_{sxll}, F_{sxlr}	Secondary suspension force of front truck in the lateral direction
F_{sxtl}, F_{sxtr}	Secondary suspension force of rear truck in the lateral direction
f_{sxll}, f_{sxlr}	Damper force of MR damper that connects front truck and car body
f_{sxtl}, f_{sxtr}	Damper force of MR damper that connects front rear and car body
F_{px1l}, F_{px1r}	Lateral force of primary suspension component that connects front truck and front truck leading wheelset
F_{px2l}, F_{px2r}	Lateral force of primary suspension component that connects front truck and front truck trailing wheelset
F_{px3l}, F_{px3r}	Lateral force of primary suspension component that connects rear truck and rear truck leading wheelset
F_{px4l}, F_{px4r}	Lateral force of primary suspension component that connects rear truck and rear truck trailing wheelset
F_{py1l}, F_{py1r}	Vertical force of primary suspension component that connects front truck and front truck leading wheelset
F_{py2l}, F_{py2r}	Vertical force of primary suspension component that connects front truck and front truck trailing wheelset
F_{py3l}, F_{py3r}	Vertical force of primary suspension component that connects rear truck and rear truck leading wheelset
F_{py4l}, F_{py4r}	Vertical force of primary suspension component that connects rear truck and rear truck trailing wheelset
y_{e1l}, y_{e2l}, y_{e3l}, y_{e4l}	Track irregularities transmitted from four wheelsets

LIST OF ABBREVIATIONS

Abbreviation	Description
EMU	Electric multiple unit
LQG	Linear quadratic Gaussian
LQR	Linear quadratic regulator
MR	Magnetorheological
NSF	Negative stiffness superimposed with friction damping
NSV	Negative stiffness superimposed with viscous damping
RMS	Root mean square

CHAPTER 1

INTRODUCTION

1.1 Research Background

High-speed railway now is busier than any time in the past. Many countries have built or continue to invest in high-speed rail networks, and now high-speed rail is considered as a viable option to improve the public transport service, taking people off from the air and congested roads. The first modern high-speed rail Shikansen was built in Japan in 1964, which operated between Tokyo and Osaka at speeds of 210 km/h. So far, the high-speed rail network in Japan has reached 2,616 km. In Europe, the extensive high-speed rail networks deliver convenient and efficient intra-national transport service. Moreover, the cross-boarder high-speed rail links connect several countries like France, Germany, Italy, Switzerland and Britain etc., to enable passenger service that span the continent. AGV Italo is currently the fastest operating train in Europe. It runs between Napoli and Milano, with a commercial speed of 360 km/h. However, Britain plans a new high-speed line HS2, from London to Birmingham. The train will operate at speeds up to 560 km/h, faster than any current commercial speeds in Europe. More recently, China is witnessing a surge in high-speed rail service. The first high-speed line, Beijing-tianjing intercity rail, only began service in 2008. The operating line now in China is over 19,000 km, more kilometers than any other country in the world. Amongst, Beijing-Shanghai high-speed line is the longest high-speed corridor that was built in a one single phase, up to 1,318 km. Beijing-Guangzhou high-speed line is the world's longest high-speed line. The 2,298 km line runs between Beijing and Guangzhou, and will eventually connect Hong Kong via Shenzhen. The general benefits of high-speed train are well understood. It is capable of providing the step-change capacity, meeting the long-term passenger and freight growth. Moreover, the high-speed rail brings cities closer together, which is a catalyst to boost economic growth, and help to balance the economy between cities. Although the cost of a high-speed line is huge, its impact to the entire society knows no bound. It is believed that the current expansion of high-speed rail is just a starting point.

Speed is the key to the high-speed rail revolution. The state-of-the-art rail system, including vehicle structure, traction system, track, bed, and route etc., is to guarantee that the train operates up to high-speed standard, and even much faster. It should be noted that, as train speeds increase, problems of vehicle vibrations, particularly in the lateral direction, become more vulnerable, posing risks of deteriorated ride quality, vehicle stability and even safety issue. Isolation of vibrations transmitted from the tracks is the essential task of the suspensions. Conventional suspension employs dissipative elements to mitigate vibration from the vehicle structure. It is simple in design, cost-effective, and reliable. However, passive solution usually fails to obtain levels of dynamic performance encompassing high speeds, ride quality and vehicle stability, since there are always trade-offs between these issues. The inherent limitations of passive suspension stimulated more viable approaches, controllable suspensions.

Modern control theory and advanced technology of actuators and sensors make possible the practical, high-integrity and sophisticated controlled suspensions for railway vehicle. It has been only a few decades since the first full-scale demonstration of an actively controlled suspension reported by British Rail Research in 1970s (Goodall et al. 1981). Since then, railway industrial has experienced an explosive development from purely passive system to deliberately controlled system. A great variety of tilting trains went into service in 1980s, e.g., the Talgo Pendular in Spain, the APT in the UK, and the ETR 450 Pendolino in Italy (Iwnicki 2006). The first fully active secondary suspension using hydraulic actuators for JR East series E2 and E3 Shinkansen trains (Tahara et al. 2003) has been in service in Japan since 2001. The system has been upgraded to the Shinkansen Fastech 360-S and 360-Z having an electro-magnetic active suspension and a tilting system with a maximum tilt of 2o for passenger ride comfort (Hughes 2006).

Recently, semi-active suspension with magnetorheological damper (short for MR damper) emerged as a promising alternative of fully active solution, since it is much less demanding in power supply, more reliable and fail-safe, while the MR damper can generate high and high bandwidth damper force and achieve dynamic performance that closely approaches the active actuators. However, although increasing amounts of semi-active suspension for railway vehicle have been reported in more recent years, the impact is principally limited to numerically analysis and validation, whereas elsewhere, the introduction of MR damper has made much more fundamental changes, such as in automobile community (Choi et al 2001.), and in civil engineering field (Dyke et al. 1996). In view of that high-speed train is a one of the most complicated dynamic system, which exhibits a variety of motions, i.e., translations, yaw, rolling and pitching, and involves nonlinear wheel-rail interaction, in-depth insights into practical and high-integrity semi-active controller is vital, so as to maximize the suspension dynamic performance by only controlling a subset of degrees of freedom. Among these, a few important issues are highlighted as follows.

Nonlinear damper dynamics

Actuator is one of the most important elements for control system. High-speed rail saws increasingly step-up actuation requirements, which progresses from hydraulic or pneumatic, to electro-mechanical or electro-magnetic technologies (Bruni et al. 2007). However, these advanced actuators usually exhibit certain nonlinear dynamics, such as saturation and hysteresis. Among these, MR damper is a strongly nonlinear hysteretic device, though its potential for control is profound. Adequate and efficient representation of direct input/output relationship and its invert is very challenging, but yet is implicitly crucial for system analysis and controller construction. Additionally, MR damper is essentially a dissipative element that cannot produce active forces. And abrupt clipping would result in energy spillover, and therefore excite nonlinear system vibrations (Weber et al. 2010).

System nonlinearity

The interaction between wheel and rail introduces nonlinear dynamics to the rail vehicle system, or uncertain changes in the system parameters. This effect would be magnified when dealing with an accelerating train (Cheli and Corradi 2011). However, the control of the vehicle system is usually formulated within the linear optimal control framework, such as LQR (Zhao and Cao 2012) and LQG (Wang and Liao 2009a, b). The nonlinearity or the uncertainty would largely compromise the suspension performance and even endanger the vehicle stability (Zhao and Cao 2012).

Experimental demonstration

Even though the general benefit of controlled suspension for high-speed train is well recognized, few of these have been applied in service operation, and there have not been any experimental demonstrations of semi-active suspension for high-speed train reported so far. An effective controlled suspension generally involves dampers with sophisticatedly designed control force ranges, high frequency performance and geometrical deployment (i.e., control subset), and highly integrated feedback network.

1.2 Research Objectives

This research program primarily focuses on the development of semi-active MR suspension for high-speed trains. The specific objectives of this research are in what follow.

(1) To conduct the full-scale demonstration experiment to verify the effectiveness of MR suspension on vibration attenuation for high-speed trains using deliberately designed MR dampers;

(2) To formulate the direct and inverse dynamic models of the developed MR damper. It is desirable that the representation models are adequate and efficient for numerical analysis and controller construction;

(3) To develop a semi-active system controller that is effective and robust for high-speed trains negotiating on the random track irregularities;

(4) To numerically validate the effectiveness of the proposed system controller on an integrated full-scale high-speed train depicted by 15 degrees-of-freedom.

1.3 Thesis Organization

The thesis organized in six chapters. Each chapter is briefed as follows.

(1) Chapter 1 introduces the research background, and identifies the research objectives to be solved in this research project.

(2) Chapter 2 primarily presents the state-of-the-art research dealt with MR damper modeling and train control system. A brief introduction to the MR fluids and MR devices is firstly presented, then followed by a detailed review on the direct and inverse modeling of the MR damper, and the damper controller fabrication. Secondly, a concise survey on the control system of railway vehicle is presented. Lastly, the control methodologies for semi-active suspensions over the past decades are summarized.

(3) Chapter 3 summarizes the full-scale demonstration experiments on the MR secondary suspension of high-speed train. Three types of MR dampers with different force ranges are investigated, respectively. The experiment setup is briefly described, including damper geometry and installation, sensor deployment and vehicle operations, e.g. track irregularities and running speed levels. The dynamics of the passive-on damper is then depicted. And the performance of the derived passive-on MR suspension is finally assessed.

(4) Chapter 4 presents the methodology of modeling the forward and inverse dynamics

of the newly designed MR damper. Firstly, the forward dynamics of the MR damper is described using an existing visco-elastic plastic based model. The model parameters are minutely examined, and the effect of the current input and damper motions is identified. Subsequently, the existing model is extended to take into account all these three factors as variables. The inverse model is obtained by analytically solving the direct model.

(5) Chapter 5 presents the simulation study on the influence of negative stiffness properties on vibration attenuation of high-speed trains. The emulated dynamics is integrated into a full-scale high-speed rail EMU portrayed by fifteen degrees of freedom. The vibration attenuation performance of the developed suspension is assessed numerically.

(6) Chapter 6 summarizes the findings accomplished in this research program.

CHAPTER 2

LITERATURE REVIEW

2.1 MR fluids and MR devices

MR fluids are a kind of smart materials whose characteristics can be changed rapidly and reversibly by an external magnetic field. The discovery of MR fluids dates back to 1940s (Rabinow 1948). The fluids consist of magnetically polarizable micron-sized particles dispersed in a non-magnetic carrier liquid. In the presence of an applied magnetic field, the fluids become a semi-solid, and exhibit the viscoplastic behavior. The primary appeal of MR fluids is the capability to produce a high yield stress, up to 100 kPa (Weiss and Duclos 1994). Additionally, MR fluids can operate stably at temperatures from -40 to 150 ^{o}C with only slight variations in the yield stress (Carlson and Weiss 1994). It is insensitive to impurities (Jolly et al. 1999). Moreover, controlling the MR fluids only requires a relatively low power supply, e.g., a battery of 12 to 24 V. Owing to these significant potentials for mechatronic system, the MR fluid have attracted considerable attentions, with major surveys presented by Ashour et al. (1996), Spencer et al. (1997), Jolly et al. (1999), Wang and Gordaninejad (1999), Carlson and Jolly (2000) and Choi et al. (2005), Wang and Liao (2011), etc.

The controllable MR devices can work in different modes, i.e., the flow mode (Carlson et al. 1996; Wang and Gordaninejad 2000), the direct shear mode (Carlson and Jolly

2000; Werely et al. 2008), the combination of the two (Hong et al. 2008) and the squeeze mode (Jolly and Carlson 1996; Wang et al. 2005a). Over the years, a number of innovative devices on the basis of the MR fluids have been developed, for example, MR brakes and MR clutches (Li and Du 2003; Kavlicoglu et al. 2007; Karakoc et al. 2008), MR fluids seals (Kurdonski and Gorodkin 1996; Saito et al. 2006), MR valves (Ai et al. 2006; Hirani and Manjunatha 2007), active MR bearings (Agrawal et al. 2002; Hesselbach and Abel-Keihack 2003), smart rehabilitation devices (Carlson et al. 2001; Dong et al. 2006; Avraam et al. 2008), human prosthetic knees (Herr and Wilkenfeld 2003; Chen and Liao 2010; Gao et al. 2017) and MR dampers (Carlson et al. 1996; Kelso and Gordaninejad 1999; Yang et al. 2002; Ciocanel et al. 2006; Choi and Wereley 2009; Tu et al. 2011). Specially, MR dampers are emerging as popular semi-active actuators for vibration control, such as buildings and bridges (Gordaninejad et al. 2002; Loh et al. 2007; Aly et al. 2010; Rodriguez et al. 2012), automobiles (Choi et al. 2000; Gopala Rao and Narayanan 2008), heavy trucks (Simon and Ahmadian 2001; Guglielmino 2005; Eslaminasab et al. 2007) and railway vehicles (Wang and Liao 2005, 2009a, b).

2.2 Modeling of MR damper

An effective dynamic model of MR damper is a key to the achievement of a practical high-integrity semi-active control system. It is essential for system response prediction and analysis, and control system design, establishment and implementation. In general, MR damper modeling involves two aspects: forward model and inverse model. Forward model is to predict the damper force according to the damper dynamics (i.e., the displacement and velocity across the damper) and the current input to the damper, while the inverse model is to determine the current (or voltage) to the MR damper to track the desired damper force according to the damper displacement and velocity. It is well known that the MR damper is a strong nonlinear device. Additionally, its dynamic behavior is dependent on not only the applied current level, but also the excitation displacement and frequency amplitude. Therefore, the description model usually involves sophisticated mathematical equations or/and too many model parameters to be adopted. It is still a challenging task to establish an accurate model that fully captures the nonlinear hysteresis exhibited by the MR damper, and yet is operation-friendly for engineering application. The following sections summarize the MR damper models developed over the last few decades. The content unfolds in two main categories: forward modeling including parametric and non-parametric modeling, and inverse modeling which also introduces the damper controller construction.

2.2.1 Forward models for MR damper

According to the methodology that proposes the characterization model, the forward model can be categorized into parametric model and non-parametric model. The parametric model is a combination of mechanical elements, such as springs and dashpots. On the other hand, nonparametric model make use of polynomial approximation or black-box modeling techniques, to represent the direct dynamics of MR dampers.

2.2.1.1 Parametric models

Bingham model based models

Stanway et al. (1987) proposed Bingham plastic model (simply Bingham model), which only consists of a Coulomb friction element in parallel with a viscous damper, to characterize the damping mechanism of electrorheological (ER) fluids, a counterpart of MR fluids. Later Spencer et al. (1997) adopted it to portray the dynamic behavior of a MR damper. Bingham model assumes that the MR fluid is rigid at the pre-yield state, and it only accords with the viscous damping that the MR damper exhibits at the post-yield state. Although the model can reasonably reproduce the force-displacement trajectories of the MR damper, it fails to capture the damper hysteresis at the low velocities, which is important for control applications. Gamota and Filisko (1991) proposed an extended Bingham model for ER fluids characterization by connecting a standard linear solid model in series with the Bingham model. Spencer et al. (1997) applied it for MR damper modeling. The extended model can portray the hysteretic behaviors of force-displacement and force-velocity trajectory well. However, the governing ordinary differential equation is extremely stiff due to the Coulomb friction element. It requires very small time steps to simulate the system, making it very difficult to deal with numerically (Spencer et al. 1997).

Biviscous models

By assuming that the fluids is plastic in both the pre-yield and post-yield region, Stanway et al. (1996) proposed a nonlinear biviscous model that uses the piecewise linear function to fit the force-velocity hysteresis loop. Observing the distinct pre-yield hysteresis of the force-velocity trajectories, Wereley et al. (1998) improved the nonlinear biviscous model by shaping a hysteresis cycle in the pre-yield force-velocity trajectories. The extended model can adequately describe the nonlinear force-velocity characteristics. However, it is inadequate for random oscillations since the piecewise linear describing function is non-differentiable equations. Ang el al. (2004) proposed a nonlinear hysteretic arctangent model by employing an arctangent function to combining the linear describing equations of the pre-yield and post-yield regions.

Viscoelastic-plastic models

It is reported that, three distinct rheological regions in which the MR damper operates can be identified as pre-yield, yield and post-yield (Gamota and Filisko 1991). By using Kelvin chain element to represent the viscoelastic behavior over the pre-yield domain, using current-dependent Coulomb force to represent the yield, using viscous damping to represent the viscous behavior in the post-yield region, and paralleling the three together, a viscoelastic-plastic model can be obtained (Pang et al. 1998). Li et al. (2000) presented enhanced viscoelastic-plastic model for MR damper by serializing a three-parameter solid model and a viscous damper. In particular, it introduced friction force to the pre-yield damper force which results from the piston seal, and inertial component to the post-yield force. While a work by Li et al. (2013) reported a four-parameter viscoelastic-plastic model by serializing a Kelvin model and a viscous damper, and using a tangent function as a transition, from which the salient dynamic behavior of MR damper, such as pre-yield hysteresis width and inclination, yield force, and post-yield viscosity, can be explicitly expressed.

Bouc-Wen model based models

In view of that Bouc-Wen hysteresis operator (Bouc 1971; Wen 1976) is capable of representing a large class of hysteresis behavior (Ismail et al. 2009), Spencer et al. (1997) paralleled it with a spring and a viscous damper for MR damper modeling. This simple Bouc-Wen model can predicts the force-displacement behavior of the MR damper well, but it is not able to describe the force-velocity roll-off effect in the yield region due to bleed or blow-by of fluid between the piston and the cylinder (Spencer et al. 1997). To better characterize the nonlinear hysteresis in this region, a modified Bouc-Wen model (Spencer et al. 1997), also known as phenomenological model, was proposed by serializing a dashpot with the simple Bouc-Wen model and then paralleling a spring. In addition, the model parameters are formulated as a current-dependent linear function so as to account for the fluctuating magnetic field strengths. Later, Yang et al. (2002) enhanced the formulation as a third-order polynomial of the current input to address the time-varying effect of the command current. To apply to a large-scale 20 ton MR damper, Yang et al. (2004) improved the phenomenological model to take into account the MR fluid stiction phenomenon and the inertial and shear thinning effects. Dominguez et al. (2006a) introduced the frequency, amplitude and current as independent variables to the simple Bouc-Wen model, to generate a more accurate and generalized hysteresis model against varying excitation inputs. Ismail et al. (2009) verified that the Bouc-Wen model was functionally redundant, and therefore proposed a normalization scheme to reduce the number of the model parameters to be adapted. Bai et al. (2015) introduced this scheme to the phenomenological model for the MR damper. In their work, a modified phenomenological model was derived through model normalization and reconstruction, which was more straightforward and explicit for hysteretic dynamics characterization, computationally efficient, and yet maintained adequate level of accuracy.

Dahl model based models

Dahl model (Dahl 1976) was developed to express the friction behavior of a control system. Zhou et al. (2006) proposed a modified Dahl model to represent the MR dampers. The obtained model can capture the force-velocity hysteresis in the low velocity well. Besides it involves only eight parameters to be identified. Ikhouane and Dyke (2007) reported a viscous Dahl model that consists of a Dahl hysteresis operator and a dashpot in parallel, to model the shear mode MR dampers. Recognized as a simplified version of Bouc-Wen model, the viscous Dahl model was applied to small-scale MR damper modeling (Tsouroukdissian et al. 2009; Aguirre et al. 2010) amd large-scale MR damper modeling (Aguirre et al. 2012).

LuGre model based models

LuGre hysteresis model (Canudas-de-Wit et al. 1995; Lischinsky et al. 1999) is capable of capturing most of the friction behavior, including Stribeck effect, hysteresis and stiction etc. The basic idea for MR damper behavior characterization using LuGre hysteresis operator is that the MR particle chains are modeled as the brushes with sticking and sliding against the damper housing. Jimenez and Alvarez-Icaza (2005) proposed a modified LuGre model that consists of a current-dependent LuGre hysteresis component and the linear spring and residual force due the damper accumulator, to describe the MR damper dynamics. On the other hand, Sakai et al. (2003) and Terasawa et al. (2004) reported a simplified LuGre model of MR damper and the accordingly online estimation scheme for model parameters. The proposed method works for both the forward and the inverse modeling, but since the describing model ignores the Stibeck effect given in the internal variable, the behavior of the damper at the low velocities is not captured.

Hyperbolic tangent function based models

Modeling of MR damper can make use of hyperbolic tangent function. Guo et al. (2006) serialized a Kelvin model with a hyperbolic tangent shape function, and then paralleled another Kelvin model, to model the dynamic behavior of the MR damper. Kwok et al. (2006) proposed a hyperbolic tangent function based model for MR damper, which consists of a dashpot, a linear spring and a hyperbolic tangent function in parallel. Owing to its purely algebraic expression, the model was much numerically convenient and efficient. Due to its numerical stability, hyperbolic tangent model was adopted to capture severe nonlinear behavior of large-scale MR damper. Bass and Christenson (2007) proposed a hyperbolic tangent model to capture the salient dynamics of a large-scale 200 kN MR damper. In their work, two sets of spring-dashpot elements stimulated the pre-yield and post-yield viscoelastic behavior, respectively; an inertial mass represented the MR fluids and piston, and connected to a Coulomb friction element that was expressed in hyperbolic tangent form to resist motion. To fully capture the time-varying effect of the command current for a large-scaled MR damper, Jiang and Christenson (2012) formulated the model of the pulse-width modulated (PWM) power amplifier which outputted current to damper and the model of the time varying inductance of the damper coils and surrounding the MR fluids. The proposed models were serialized with the hyperbolic tangent model by Bass and Christenson (2007), to describe the dynamics of the 200 kN MR damper.

2.3.1.2 Non-parametric models

Polynomial models

Choi et al. (2001b) identified two branches of force-velocity trajectories with the positive accelerations and the negative accelerations, and then built a sixth order polynomial function to fit the two branches respectively. The main challenge of this model is that there are usually too many parameters to be adopted in the modeling process, since at least fifth order polynomial is adequate to capture the hysteresis of the MR damper. Since it is quite easy for implementation, this model has been widely applied for MR damper modeling (Ubaidillah et al. 2011). Song et al. (2005) adopted a series of numerically efficient mathematical functions to characterize the MR damper dynamics, including a polynomial function to represent the saturation, a modified hyperbolic tangent function to capture the transition of the MR damper from the pre-yield region to the post-yield region, a nonlinear first-order filter to create the hysteresis, and an offset function for the residual force due to the damper accumulator. Metered et al. (2009, 2012) employed three-dimensional interpolation of Chebyshev polynomial to model the MR damper dynamics with measured displacement, velocity and input voltage.

Neural network models

Since the groundbreaking research in the 1950s (Von Neumann 1958), neural network theory has formulated dozens of models for learning and adaptation, including feed forward network, recurrent neural network, back propagation neural network, cellular neural network, radial basis function, etc. In the past decades, it has demonstrated the excellent potential to support fundamental theoretical research and engineering applications. Chang and Roschke (1998) represented the MR damper dynamics in terms of a multilayer perceptron neural network. The model was trained by a Gauss-Newton based Levenberg-Marquardt method, and optimized by an optimal brain surgeon strategy. Wang and Liao (2001, 2005) trained a feed forward neural and a recurrent neural network for the direct and inverse dynamic modeling of the MR damper. The validation indicated that the recurrent neural network model can predict the damping force accurately and generate the commanded current that closely tracks the desirable control force. Du et al. (2006) represented the dynamic behaviors of the MR damper by an evolving radial basis function network. The model was trained by combining the genetic algorithms and other standard learning algorithms. Wang et al. (2009) reproduced the force-displacement and force-velocity trajectories of the MR damper using a back propagation neural network approach.

Although the neural network approaches have demonstrated their advantages in solving nonlinear problems, most of the proposed neural network models were trained using simulated data generated by the phenomenological model (Chang and Roschke 1998; Wang and Liao 2001, 2005; Du et al. 2006; etc.), rather than experimental data, since the system noise and knocking effect would make the training much more difficult. Metered et al. (2010) trained the feed forward and recurrent neural networks to model the forward and inverse dynamics of the MR damper using experimental data generated through dynamic tests, and studied the effect of the surface temperature of the damper cylinder on the damper dynamics. Bhowmik et al. (2013) presented a training scheme for the feed-forward back-propagation neural network for a rotary MR damper modeling using experimental data. The training was done by a limited number of harmonic displacement cases, and constant and half-sinusoidal current cases. Chen et al. (2015) presented a NARX (nonlinear autoregressive with exogenous inputs) modeling and neural network technique for the MR damper modeling using experimental data generated under harmonic loading. The model was trained by the Bayesian regulation to avoid the overfitting problem and improve the generalization.

Fuzzy-neural models

Fuzzy-neural theories are a combination of fuzzy logic theory and neural network technique. Won and Sunwoo (2009) developed a fuzzy model for MR dampers by characterizing their nonlinear behaviors as a linear system model in each operating regime. Du and Zhang (2008) developed an evolving Takagi-Sugeno fuzzy model to emulate the dynamics of an MR damper. Askari and Markazi (2010) obtained a similar evolving Takagi-Sugeno fuzzy model of compact size and acceptable accuracy, by which the rule structure, the input structure and the membership function parameters can be optimized simultaneously. Ahn et al. (2009) proposed a self-tuning fuzzy technique combined with neural network to on-line train the fuzzy parameters. The result showed that, the modeling accuracy was significantly improved. Truong and Ahn (2010, 2011) modeled MR damper dynamics using fuzzy-neural technique. In their work, centre-average defuzzification architecture was employed to build the black-box relationship between inputs, i.e., displacement/velocity and current and output (damper force).

2.3.2 Inverse dynamic models

The MR damper inverse model represents the relationship between the applied current/voltage and the displacement and velocity across the damper and the damper force. It is important for a control system, due to the fact that it is the applied current/voltage to be directly commanded, rather than the force generated by the MR damper. However, an accurate yet practical inverse model is always difficult, since the MR damper is a highly nonlinear hysteretic device. The representation is usually obtained by deriving from the forward model, or by soft computing techniques, such as neural networks and fuzzy logic models.

2.3.2.1 Inverse function models

Inverse Bingham and piecewise models

Due to model simplicity, the inverse models of MR damper were often obtained by the Bingham representation (Tsang et al. 2006; Reader et al. 2006). These kinds of inverse models are generally not adequate for high performance control systems or for high fidelity simulations, since they ignore the hysteresis dynamics in the pre-yield regions or at low velocities.

Inverse Bouc-Wen models

Tsang et al. (2006) proposed a simplified inverse dynamic model for the MR damper based on the Bouc-Wen hysteresis model, by formulating the MR fluid yield stress as an exponential function of the applied current. This inverse model was inadequate in the low velocities, since it neglected the pre-yield hysteresis of the damper behavior.

Inverse model can also be obtained by normalized version of Bouc-Wen model (Ismail et al. 2009). Bahar et al. (2009) performed the linearization scheme to the current-dependent parameters of the normalized Bouc-Wen model. In this way, the describing equations were linear in parameter, and thus inverse model was derived directly. Qian et al. (2016) proposed a modified phenomenological model where the damper force can be expressed by algebraic equations, in contrast to the phenomenological model involving nonlinear differential equations. The field current can be obtained directly by solving the governing equations. The developed model illustrated excellent force tracking capability, however, one shortcoming was that it required damper force feedback.

2.3.2.2 Soft computing models

The forward and inverse models of MR damper usually work as a pair. Therefore, only not forward modeling, but inverse models of MR damper are of great interest in soft computing community. Zong et al. (2012) represented the inverse behavior of the MR damper by adaptive neuro-fuzzy inference system (ANFIS). The model was trained using simulated data generated by phenomenological model. In the work by Bhowmik et al. (2013), the feed-forward back-propagation neural network was trained using experimental data to represent the forward and inverse dynamics of a rotary MR damper. Although superior accuracy was illustrated in predicting the forward dynamics, for inverse dynamics, significant local spikes occurred at zero-crossings of the velocity because of the force knocking effect induced by the bearing plays of the damper rod joints. It was indicated that, the neural network is quite sensitive to the high frequency signal components and hardly able to filter out those low frequency signal inputs (Bhowmik et al. 2013).

2.3.2.3 Force feedback based controller

An accurate inverse model of MR damper is an effective tool to construct the damper controller. However, the inverse dynamic behavior in terms of the control current is usually difficult to obtain, due to its intrinsic nonlinear characteristics. Therefore, efforts have been made to make use of external feedback to track the damper force. Dyke et al. (1996) designed a Heaviside step function controller with force feedback for MR damper for seismic response reduction. The commanded voltage switched between two states: zero and the (allowable) maximum by comparing the measured damper force with the desired one. Yoshida and Dyke (2004) enhanced the controller performance by modifying the control voltage as a linear function of the optimal damper force. The proposed scheme can avoid the high local accelerations induced by the large changes in the forces generated by the damper. Liao and Wang (2003, 2009a,b) constructed a signum function based force feedback controller that was also capable of continuously varying current command. It was validated that the proposed controller can generate the damper force that resembles the desired force. The force feedback controllers usually require force sensor, which increases cost and complexity, and induces uncertainties to control system. Truong and Ahn (2010, 2011) presented a novel closed-loop self-sensing controller for MR dampers. In their work, a direct MR damper model established by fuzzy-neural technique worked as a virtual force sensor, instead of a real one, to feed back the damper force. Weber (2013) proposed a feed-forward force tracking scheme for a rotational MR damper. The scheme estimates the damper force by the Bouc-Wen model, and compares the estimated force with the desired force to determine the current input to the damper.

2.3 Train control system

The railway train runs along a track. Before dealing with dynamics of high-speed train, it has to understand the irregularities of tracks. There are mainly two types of track features, i.e., curve (also intended or deterministic track) and straight track (unintended or indeterministic track). With respect to different track features, the railway vehicle would exhibit different dynamic behaviors. However, the both tracks can introduce significant vibrations to the car body, thus affecting what is perceived by the passengers sitting or standing in the car body. The primary concern of the train suspension is to attenuate these unwanted vibrations from the car body, meanwhile to obtain acceptable levels of vehicle dynamic stability and wheel-track interaction etc. There are three major mechanical sub-systems in railway vehicle control system to deal with the mentioned track features, i.e., tilting suspension, secondary suspension, and primary suspension, which are

2.3.1 Tilting trains

Tilting trains are now well recognized as an effective means to negotiate curve (deterministic track) at higher speeds. The idea is quite straightforward that, tilting the vehicle body inwards on the curve would reduce the large lateral acceleration that is perceived by the passenger in the car body. Early passive tilting trains solely relied on the natural pendulum motions, which might cause safely issue, such as vehicle overturning (Persson et al. 2009). Afterwards, active system was introduced, which has become a standard railway technology worldwide (Goodall and Brown 2001). An active system usually involves a tilt mechanism, mostly tilting bolster which is connected to the bogie, and actuators installed between the bogie and the bolster, to generate the large angles inwards. One type example is that, Swedish X2000 tiling train is able to provide a maximum tilt up to 10^{o} (Zhou et al. 2011). There are also studies of limited angle tilting without bolster. Sumitomo, a new airport express in Nagoya, is able to give a 2^{o} tilt using the airsprings alone (Shinoda et al. 2003). FlexCompact produced by Bombardier employs an active anti-roll bar to provide a larger tilt angle of around 4^{o} (Jakob 2007).

The control objective of tilting is to improve the vehicle response (i.e., roll motion) to the deterministic track inputs, i.e., the curves, without affecting the ride comfort (i.e., lateral) on the straight tracks, i.e., the random track irregularities. They are usually two separate objectives in a railway vehicle, one for tilting suspension and the other for secondary suspension. More recent studies reported the possibilities of incorporating the two together. In the work by Zhou et al. (2011), the tilting suspension was combined with lateral centering device and semi-active damper as an integration to fulfill the two objectives. Another trend for tilting train development is an entirely feed-forward control concept, where the tilting action is commanded by feeding the vehicles with track information from a track database just before the train enters the curves (Hauser 2006; Zamzuri et al. 2006), in contract to the common tilt train, which signals the tilting action according to the accelerometer mounted on a non-tilting part of the bogie. However, the accurate positioning of the rail vehicle along the track and the reliable track database are still challenging.

2.3.2 Secondary suspensions

In contrast to tilting suspension which concerns the ride quality on curve transition, secondary suspension focuses on the straight-track ride comfort (i.e., random track irregularities). Additionally, it is also used to support the car body mass in the vertical direction, and the quasi-static curving force in the lateral direction.

The secondary suspension comprises of airsprings and dampers in the longitudinal, vertical and lateral directions, accounting for the vertical and lateral vibrations explicitly and the yaw and pitch motion implicitly. It was convinced that, the vertical ride comfort is less of a problem since the introduction of self-leveling airsprings in the 1960-70s (Bruni et al. 2007), which are themselves a kind of active suspension. Recent studies related to controlling car body flexible modes revealed that, the car body elastic vibration, particularly the first bending mode, becomes a problem for light-weight vehicles, e.g., Shikansen vehicles in Japan, which are designed as light-weight as possible to achieve high operating speed (Sugahara et al. 2011). The experimental research projects on Japanese Shikansen reported the uses of variable axle dampers in conjunction with a LQG controller to selectively suppress the first bending mode vibration of the car body (Sugahara et al. 2008, 2011).

Secondary suspension design is commonly more difficult in the lateral direction, since there is strong coupling between the lateral and yaw motions. The first full-scale demonstration of an actively controlled lateral secondary suspension was reported by British Rail Research in 1970s, which claimed that, up to 40-50% reduction in root-mean-square (RMS) acceleration of car body was reliably achieved (Goodall et al. 1981). Afterwards, different forms of active secondary suspension were investigated, e.g., the electro-mechanically controlled system for French TGVs which focuses on centering of the car body (Briginshaw 2000), the pneumatic control system for JR East series E2 and E3 Shikansen trains which provides improved performance of the yaw and roll motions of the car body (Tahara et al. 2003), and the electro-magnetic control system for Shikansen Fastech 360-S (Hughes 2006). Semi-actively controlled system emerges as a simpler solution, which is capable of comparable performance without needing a large amount of power supply, as described by the demonstration research (Stribersky et al. 1998). Taking advantage of the innovative technology of semi-active actuators such as ER and MR dampers, semi-active suspension has attached considerable attentions recently (Choi et al. 2001; Liao and Wang 2005, 2009a, b). Another trend for secondary suspension development relates to the control of multiple vibrating modes, as demonstrated by the RailCab system, which involves tilt and fully active secondary suspension to obtain the performance improvement less sensitive to track irregularities (Liu-Henke et al. 2002), and the integrated tilting and lateral secondary suspension as mentioned previously (Zhou et al, 2011).

2.3.3 Primary suspension

Primary suspension deals with controlling the vehicle running behavior, i.e., stability and guidance, induced by wheel-rail contact. The basic unit of a vehicle primary suspension is wheelset. And thus, the different control challenges of primary suspension are unfolded with respect to the different wheelset types, i.e., solid axle wheelset (SAW) and independently rotating wheels (IRW). The traditional wheelset of today is solid axle wheelset, which has self-steering ability, but is inherently unstable and requires stabilization control. Especially at sufficiently high running speeds, self-excited hunting motion would occur, which might lead to safety issues, such as derailment or vehicle body overturning. Shen and Goodall (1997) proposed an actively controlled concept – actuated solid wheelset (ASW), for the closed-loop control of the solid axle wheelsets to improve the vehicle stability and curving performance. The control action can be realized either by a lateral force or yaw actuation upon the solid axle. Later, it was illustrated by Mei and Goodall (1999), the yaw actuation is superior to the lateral actuation, since it requires a lower control force to achieve the same level of stability and the better ride experience. Tanifuji et al. (2003) proposed two methods to enhance the running stability of ASW, i.e., by adding a feedback of wheelset lateral velocity, or by giving some time delay to the control force. Additionally, there are also yaw dampers for stability control, also called Secondary Yaw Control (SYC), which are installed at the secondary suspension level in the longitudinal direction, imposing a yaw torque indirectly, to resist the hunting motion (Diana et al. 2002).

Independently rotating wheelset (IRW) removes the rotational constraint between the two wheels on the axle, therefore there is no longitudinal creep force on the wheels, and stability is less of a problem in this case. On the other hand, guidance and steering control becomes a major issue. In general, there are three control configurations for

IRW, which are actuated independently rotating wheel (AIRW), driven independently rotating wheel (DIRW), and directly steered wheels (DSW). The concept AIRW was introduced by Mei and Goodall (1999), considering the lateral or yaw actuation in the form of a steering torque applied on the axle. Gretzschel and Bose (1999, 2002) presented the mechatronic wheelset concept DIRW with regard to high-speed/long-distance vehicles, where a relative torque interacting with the relative rotation of the wheels is applied to the wheels of the axles. This configuration not only provides marked steering performance without increasing friction, but ensures vehicle stability at high speeds. Aknin et al. (1991) first introduced the concept of DSW, where a pair of IRWs is actively steered to achieve guidance and curving. Wicken (1994) integrated the DSW to the railway vehicle and conducted the stability analysis, in which the DSW was guided by using feedback on lateral wheel/rail displacement. The result demonstrated the excellent steering performance together with dynamic stability at high speeds.

2.4 Vibration control of secondary suspension

Secondary suspension, which is composed of springs and dampers, connects vehicle car body and bogie. It is primarily concerned with the passenger ride quality for train vehicle associated with the indeterministic track, i.e., the straight track with stochastic irregularities, in contrast to tilting suspension which focuses on the ride comfort from the viewpoint of the deterministic curving, and primary suspension which deals with the stability and guidance. However, as mentioned in the last section, whereas controlled technologies are here to stay for practical implementation of both tilting and primary suspension, it is much less widely in service operation for controllable secondary suspension. It is also noteworthy that, vibration control for secondary suspension in the lateral direction is much more important than that in the vertical direction, since the airsprings installed between are themselves self-leveling devices that actively perform according to the vertical motion of the car body, while the lateral deployed hydraulic dampers are essentially passive components that are solely effective in terms of a narrow frequency bandwidth.

Robust and reliable actuators and their accompanying control strategies are still under development. According to structural control concept, strategies for suppressing vehicle vibration can be categorized into passive control, active control and semi-active control.

2.4.1 Passive system

Passive systems are the most common type of suspensions, which use passive elements (i.e., springs and dampers) between the car body and bogie (secondary suspension) and between the bogie and axles (primary suspension) to support the car body and isolate the vibrations from the tracks. The development of the passive suspension has been focused on the optimal design of the railway vehicle suspensions according to design objectives such as suspension maximum stroke, natural frequency of vehicle, and acceleration of car body and so on (Mastinu and Gobbi 2001). Moreover, the suspension optimization is usually difficult, since there are usually conflicting objectives, for example, the compromise between the ride quality design involving car body frequency and acceleration and the suspension compactness involving suspension deflection.

To date, the development of passive suspensions has been moving forward to some extent due to recent advances on computing techniques and application of mechanical devices. For example, introduction of soft computing theory enabled those conflicting objectives formulated and solved in one search space. Shieh et al. (2005) developed a constrained multi-objective evolution algorithm for the optimal design of a light rail vehicle suspension, so as to attain the best compromise between the car body acceleration (i.e., ride comfort) and the suspension deflection (i.e., suspension compactness). On the other hand, great effort has been made on the performance improvement of the passive components. Jiang et al. (2012) incorporated a newly developed mechanical device, the inerter, into the railway vehicle suspension, which has the properties that the force is proportional to the relative acceleration. The constructed suspension can provide more favorable performance of car body ride comfort as well as lateral vehicle response to curving, compared with the traditional passive suspension only with spring and damper. A stability study (Wang et al. 2012) on a 28-DOF full-train system with inerters also demonstrated the significant benefits of the incorporated devices to the critical speed, settling time and passenger ride comfort. However, it should be noted that, the input/output relationship of the captured passive system still depends on the system properties, such as masses, springs, dampers and geometrical arrangement, and it cannot be changed once the system is determined. In this sense, the passive system usually fails to obtain the multiple performance in one ride, which encompasses high speeds, ride quality and dynamic stability, because there are always trade-offs between various such others, e.g., the trade-off between the straight track ride quality and the curve performance. This intrinsic problem for rail vehicle, especially in nowadays high-speed transportation, has motivated research towards controllable solutions.

2.4.2 Active control

Actively controlled suspension is able to provide encompassed performance that is not possible with purely passive system in one ride, e.g., facilitating high speeds, improving passenger ride comfort and enhancing vehicle dynamic stability despite difficult track condition. The dynamic performance of active system strongly relies on the configuration of actuators, feedback systems, and the accompanying control strategies. The past few decades have witnessed the tremendous progress in railway vehicle active suspension, in terms of not only the development of modern control theory, but the advances on innovative actuator technology, such as hydraulic actuators (Shimamune and Tanifuji 1995; Foo and Goodall 2000), electro-mechanical actuators (Goodall 1997; Kjellqvist et al. 2001), electro-magnetic actuators (Goodall et al. 1993; Foo and Goodall 2000), servo-pneumatic actuators (Hirata et al. 1995; Norinao 1997; Sammier et al. 2000), etc. These active actuators are deployed laterally in secondary suspension of railway vehicle, to effectively suppress the translation and yaw modes of the car body which would greatly influence the passenger ride quality. It should be noted that, the rolling motion of the car body, as the response to the lower frequency deterministic track irregularities, is principally mitigated by the tilting action of the vehicle. The active actuators can replace the passive dampers to construct a fully active system. However, that would introduce stability problem due to the active forces directly imposed onto the vehicle, and even safety issue, especially in the event of actuator failure. Therefore, it is more beneficial to combine the active components with the passive components as a group to work together. The configuration could be fitting in parallel or in series (Bruni et al. 2007).

On the other hand, investigations on active control strategies for railway vehicle have also been considerably undertaken. Over the year, the outcomes greatly help address the fundamental problems of actively controlled secondary suspension, for example, to maintain the low-frequency characteristics of the car body, and yet to attenuate the high-frequency vibrations transmitted from the track irregularities, so as to improve the ride experience of the passenger standing or sitting in the car body (Thompson 1976; Hedrick 1981). And to date, some of the active control technologies have become part of high-speed trains in service, e.g., Shinkansen trains in Japan (Tahara et al. 2003; Hughes 2006).

There are a variety of control techniques for active suspensions for railway vehicle and automobiles so far. The early investigation on active control of vehicle suspension started with skyhook control by Karnopp (1983, 1995). It is well recognized that, the use of skyhook damping is a simple but effective tool in suppressing the absolute vibrations of the car body. However, skyhook damping can radically increase the suspension motions. In view of this, many work have been conducted to improve the control law in some manner. Novak and Valasek (1996) proposed groundhook control to decrease the suspension dynamics and improve the vehicle stability. However, it would considerably increase the car body dynamics. Afterwards, hybrid control (Ahmandian and Simon 2002; Ahmandian and Vahadi 2006) reported a compromise between skyhook control and groundhook control. Li and. Goodall (1999) improved the skyhook controller by filtering out the absolute velocity which is associated with deterministic track. The described active secondary suspension exhibited a better ride comfort in terms of both straight track and curve in a run.

The designs of active suspension were often approached from optimal control theory. Raju and Narayanan (1991) designed a linear quadratic Gaussian (LQG) controller with limited state feedback to actively control the non-stationary response of a 2-DOF vehicle model. Elmadany and Abduljabbar (1999) presented a LQG controller with a Kalman filter estimator in frequency domain for a quarter car. Later, Elmadany and Al-Majed (2001) presented the linear quadratic regulator (LQR) controller with full-state feedback for a full vehicle suspension.

Yoshimura et al. (1993) described an active suspension with preview for a 3-DOF rail vehicle (i.e., bounce, roll and pitch modes). The active control was determined by using stochastic optimal theory and with measurement of the vehicle body velocities and the irregular track inputs at the preview locations. Metin and Guclu (2010) presented a comparative study on fuzzy logic and PID actively controlled suspension of an 11-degree-of-freedom rail vehicle. The simulation verified that the fuzzy logic suspension was more effective and efficient, generating less control force and yet deriving better vibration suppression performance. Sezer and Atalay (2011a, b) designed a fuzzy logic controller for the active secondary suspension of a full-scale 54-DOF railway vehicle model subjected to different track irregularities (i.e., sinusoidal and random), to suppress the vertical and lateral vibrations of the car body.

2.4.3 Semi-active control

Semi-active control is halfway between passive and active suspensions. Semi-active control varies rapidly the properties of a tunable passive element according to the measurements of variables within the vehicle system. It is relatively simple to implement, and less demanding in power supply, but the performance is usually not as significant as fully active suspension, since it somehow just provide energy-dissipating force. Tremendous strikes have been made on effective strategy development that approach actively controlled system.

Skyhook control

Since great success and potential of skyhook control for vibration suppression have been demonstrated in active suspensions, research interest has been given to that respect. Karnopp et al. (1974) firstly introduced semi-active skyhook damping to automobile for ride comfort improvement. It was shown that, semi-active solution can achieve the performance comparable to that of fully active vibration control systems. Stribersky et al. (1998) presented the pioneer research on the semi-active damping system for a high-speed train (operating speed 250 km/h). In their work, the orifice hydraulic dampers were integrated into the rail vehicle and continuously controlled by the semi-active skyhook controller. Both the numerical and experimental validation showed the great potential of the semi-active suspension for vehicle ride quality improvement. Heo and Park (2000) proposed a modified skyhook control for a semi-actively controlled suspension, with which ride comfort is significantly upgraded while maintaining a certain level of vehicle safety. Choi et al. (2001a) conducted an experimental study on a semi-active ER suspension with skyhook controller for a passenger car. The field test illustrated the improvement of the ride comfort as well as the steering stability in the vertical direction. Reader et al. (2009) improved the performance of the semi-active skyhook control for a quarter car, by incorporating a modified controller of MR damper that enables the precise force tracking. Sun et al. (2013) found that, the secondary suspension has a great effect on vehicle stability. They tuned the MR dampers within the secondary suspension on the basis of the skyhook control, to improve the critical speeds of a high-speed train.

Linear optimal control

Liao and Wang (2003) investigated a semi-active MR suspension accounting for the vertical vibration suppression of a 9-degree-of-freedom railway vehicle of. In their study, LQG control with the acceleration feedback was adopted to determine the optimal damper force, and a signum function based damper controller was established to command the voltage to the damper. Later, Liao and Wang (2009a, b) extended the study to account for the lateral dynamics control of a full-scale railway vehicle of 17-degree-of-freedom. The evaluation indicated that, the semi-active suspension was beneficial for car body vibration attenuation, although it also resulted in the increase in accelerations of the bogie to some extent. Zhao and Cao (2012) conducted a simulation study on the lateral stability of a nonlinear Cooperrider bogie. The bogie was controlled by the LQR and clipped LQR law to enhance the critical speed of the vehicle, respectively. Both the controlled bogie illustrated superior performance, compare to the uncontrolled one.

Robust control

Owing to its inherent robustness against system uncertainties, H-infinity controller has been substantially applied for structural vibration control. In the work by Choi et al. (2002), an H-infinity controller was constructed for a full vehicle suspension which was equipped with four independent MR dampers incorporating a Bingham model. Particularly, the sprung mass of the vehicle (the car body) was treated as uncertain parameter. Shin et al. (2014) performed the numerical and experimental research on railway vehicle secondary suspension with MR damper. In their work, H-infinity control was applied to suppress the car body yaw mode. The weighting function was determined by repeated analysis so as to improve the vibration attenuation performance of car body and while attained certain level of vehicle stability of bogie. The control performance was verified by the scaled rig test on a half vehicle.

Soft computing techniques

To enhance the effect of PID control, Yang et al. (2011) trained the system performance of a quarter car by using back-propagation neural network. In their work, the coefficients of the proportional, integral and differential components were optimized to obtain the best combination of the three. Bakar et al. (2011a, b) proposed a fuzzy semi-active damping force estimator for vehicle ride comfort improvement. Ubaidillah et al. (2011) constructed a skyhook-based fuzzy logic controller for a semi-active quarter car. In contrast to the conventional skyhook damping, the controller identified four cases of motions that the car body and suspension occurs, and determined the outputting damping accordingly. Both the simulation and experiment verified that the fuzzy logic controller outperformed the on-off and continuous skyhook controller.

2.4.4 Negative stiffness

Application of negative stiffness provides innovative insight into vibration reduction strategies. Several novel negative stiffness devices were designed and fabricated. Carrella et al. (2007, 2008) reported a quasi-zero-stiffness mechanism which can be attached to lower the natural frequency of the system. Le and Ahn (2011, 2013) proposed a vibration isolation system with a negative stiffness structure for driver seats in low frequency vibration conditions. The experimental investigation showed that the resonance phenomenon almost didn't occur. Later, they conducted a comparative investigation of an active pneumatic vibration isolation system for a vehicle seat with and without negative stiffness structures (2014). It was validated that, the isolation effectiveness of the active system with negative stiffness structure was better than that of the one without the proposed structure. Fulcher et al. (2014) investigated the negative stiffness behavior of a buckled beam mechanism for passive vibration and shock isolation systems.

Semi-active control devices for negative stiffness have been investigated. Iemura and Pradono (2009) found the negative stiffness characteristics within skyhook algorithm, and proposed pseudo-negative-stiffness semi-active dampers for seismic response. Hogberg (2011) introduced the equivalent negative stiffness to buildings vibration suppression. The equivalent negative stiffness was generated by MR damper. The results demonstrated a potential increase in damping efficiency with negative stiffness. Weber et al. (2011) presented an innovative tuned mass damper for cable control with positive/negative stiffness. Weber (2014a) proposed a semi-active vibration absorber to reset the stiffness properties of the structure. Later, Weber (2014b) realized the emulation of negative stiffness by real-time controlled MR damper. Yang et al. (2014) proposed a novel magnetorheological elastomer isolator with negative changing stiffness for automobile suspension.

CHAPTER 3

AN EXPERIMENTAL STUDY ON MR SECONDARY SUSPENSION FOR HIGH-SPEED TRAIN FOR RIDE COMFORT IMPROVEMENT

3.1 Introduction

The past few decades have witnessed the tremendous development of high-speed train worldwide. However, as the train speeds increase, the problem of passenger ride comfort, particularly in the lateral direction, becomes more vulnerable to track irregularities. Advanced suspensions have been under investigated for mitigating vibration from train carriage for many decades. The passive suspension is here to stay (Fujimoto et al. 1996; Shieh et al. 2005; Jiang et al. 2012). However, its dynamic performance is solely dependent on the inherent dynamic characteristics, and thus it cannot provide satisfactory performance over the whole range of working conditions. The active suspension (Hedrick and Wormley 1975; Goodall and Kortum 1983; Goodall 1997, 2011; Bruni et al. 2007) is capable of obtaining levels of dynamic performance encompassing high speeds, passenger ride comfort and vehicle stability, etc. However, it usually requires a substantial amount of energy and advanced actuators of high frequency performance (Bruni et al. 2007), which indicates a complicated and costly system with large power consumption and corresponding reliability issues. Thus, it is usually limited in service. MR suspension utilizes MR dampers instead of active component to construct controllable suspension. The incorporated MR dampers are able to vary their dynamic characteristics in a wide range, and to response continuously, rapidly and reversibly by a driven voltage or current (Carlson et al. 1996; Spencer et al. 1997; Or et al. 2008; Yazid et al. 2014; Chen et al. 2015; EI Wahed and Balkhoyor 2015). Due to their higher reliability, less demand in power consumption and potentially superior performance, MR suspension is emerging as a future trend for high-speed trains (Wang and Liao 2009a, b; Hudha et al. 2011; Sun et al. 2013). Yet, whereas in automobile community – analogue of railway industrial, the introduction of MR dampers has made much more fundamental changes in operation, the MR suspension for high-speed trains is still the pioneer research whose effectiveness is illustrated principally by theoretical study.

This chapter presents an experimental study on incorporating MR dampers in a secondary suspension in an effort to improve the lateral ride comfort of high-speed trains. The rail vehicle in tests is full-scale carriage of CRH3 electric multiple unit (EMU) high-speed train. Three types of MR dampers with different control ranges are designed, fabricated, and incorporated into the carriage secondary suspensions. The integrated system runs on a roller rig at speeds in a wide range and with random track irregularities. The performance of the MR suspension is tuned by a driven current switching among passive-off and passive-on states. In this chapter, the details on the experiment setup are firstly described. The dynamic behavior of the integrated vehicle system and ride comfort at each control state is then evaluated.

3.2 Experimental setup

The high-speed rail vehicle in tests is CRH3 electric multiple unit, as seen in Figure 3.1. The high-speed vehicle consists of a carriage, two trucks, i.e., leading truck and trailing truck, and four wheelsets, i.e., front and rear wheelsets in leading truck, and front and rear wheelsets in trailing truck. There are air springs and dampers between the car body and the bogie to construct the secondary suspension (**Figure 3.2**) accounting for the passenger ride experience, while use of the primary suspension which comprises springs and dampers (**Figure 3.3**) principally secures the stability and guidance of the vehicle.

In the existing secondary suspension, four passive hydraulic dampers connecting bogie with car body are laterally equipped for transverse vibration attenuation (**Figure 3.4**), two in the leading truck and the other two in the trailing truck. During the full-scale rolling-vibration experiments, three types of current-driven MR dampers (type-*A*, type-*B* and type-*C*) with different control ranges replace the existing hydraulic dampers one type a time. And the aim of these experiments is to assess the possibilities of practical controllable suspension using MR dampers. The detailed specifications of the three types of MR dampers are presented in the following sections. For each series of experiments, the damping properties of the MR dampers are simultaneously varied by tuning the current input to the dampers via a linear voltage/current converter (VCC) (**Figure 3.5**), so as to construct the changeable secondary suspension. For ease of interpretation, the three MR secondary suspensions are simply short for Suspension *A* (the secondary suspension with type-*A* MR dampers), Suspension *B* (the secondary suspension with type-*B* MR dampers) and Suspension *C* (the secondary suspension with type-*C* MR dampers).

The rolling-vibration experiments are conducted on a full-scale roller rig (**Figure 3.6**) in the Traction Power State Key Laboratory of Southwest Jiaotong University, China. The testing vehicle is placed on and driven by the supporting rollers underneath (**Figure 3.7**). Each roller can vibrate in the lateral and vertical directions independently. In this way, the testing plant is able to simulate the motions of the vehicle running on different conditions (i.e., tracks and speeds). Particularly, the train is constraint at the front and back (**Figure 3.8**), therefore only the vertical and lateral translations, and the yaw and rolling are allowed during the train is running, while the longitudinal motions and pitching of the vehicle are restraint.

The EMU vehicle incorporated with MR dampers is tested on the roller rig at a broad range of running speeds from 40 to 380 km/h with random track irregularities. It should be noted that, the performance of the MR secondary suspension is tested during the experiments, which is associated with the car body motion, or equivalently, the passenger ride comfort; therefore, only the indeterministic track condition (i.e., straight track with random irregularities), rather than the curves, is considered. The random track irregularities which are collected from the straight track of Guangzhou-Wuhan high-speed rail line in China, are generated by executing the vertical and lateral motions of the rollers underneath the vehicle wheels. In this way, the dynamic behavior of the train vehicle which is running on a straight track is reproduced. Particularly, the EMU prototype is tested without passenger-equivalent vehicle loading. It makes sense because generally the vehicle loading would lower the natural frequency, and thus deliver a better ride comfort level (Iwnicki 2006).

Additionally, acceleration measurement is made during the experiments. **Figure 3.9** shows the measuring points at the floor level and at the bogie. Three optical fiber accelerometers are deployed at the center and the two ends on the car body floor to obtain the lateral accelerations of the car body, and the lateral accelerations of the bogie are also measured by the optical fiber accelerometers deployed in diagonal on each truck, seen in **Figure 3.10**. The interrogator SM130 is deployed on site for data acquisition (**Figure 3.11**). The sampling frequency of the accelerometers is set as 1,000 Hz. In the experiments, it is the optical fiber accelerometers, rather than the conventional electric-type transducers, to be used for acceleration measurement, since there are strong electromagnetic fields around the operating high-speed train, and optical fiber sensors are immune to electromagnetic interference. The obtained accelerations would go into dynamic evaluation for train vehicle including car body and bogie afterwards. In particular, the ride of the passenger is determined by UIC Code 513, which aims to identify the specific level of damper input (i.e., current) that causes the passenger ride discomfort.

The rolling-vibration experiments are conducted in terms of types of dampers, current input of dampers and running speeds, respectively. Specifically, for each type suspension, the vehicle would run at a series of standard operating speed levels; moreover, at each speed level, the damper would be imposed with a variety of current inputs. Calculating the ride comfort index for each scenario would give the best damper input for each operating speed level; equivalently, it would reveal the worst suspension properties for that specific speed level. This evaluation is reasonable, because the nonlinearity stemming from the wheel-rail contact usually causes diverse dynamic responses of a rail vehicle under different operating speeds, delivering a conclusion that, the vibration behavior of a rail vehicle is strongly related to the operating speeds (Iwnicki 2006; Cheli and Corradi 2011). With the determined optimal input of the MR dampers, a switchable MR suspension can be readily constructed to adjust itself to the prescribed damper input level on the basis of the operating speed.

In order to thoroughly investigate the suspension behavior regarding a variety of vehicle operating speeds, the experiments are arranged as follow: for each type of MR suspension (i.e., suspension *A*, suspension *B* and suspension *C*), the current input to the incorporated MR dampers is tuned from 0 A to the allowable maximum; in terms of each specific suspension (i.e., type of MR suspension and damper input level), the vehicle runs at a wide range of standard speeds, primarily from 40 km/h to 380 km/h. At each scenario, the dynamics of the vehicle is measured, and the ride comfort is evaluated. Afterwards, the optimal damper current input for a specified speed is determined as the one with the best ride comfort. On the other hand, the utilized MR dampers can be judged on their applicability to the tested EMU prototype. The rolling-vibration experiments on suspension *A* are presented immediately, followed by suspension *B*, and suspension *C*, respectively.

3.2.1 Rolling-vibration tests on suspension *A*

Four type-*A* MR dampers (**Figure 3.12**) are installed laterally in the EMU secondary suspension, as shown in **Figure 3.13**, replacing the existing hydraulic passive dampers, to account for the lateral vibration attenuation of the carriage. The power supply of the dampers is 24 V, and the maximum current is 3.6 A. **Figure 3.14** shows the hysteretic behavior of type-*A* MR dampers at a frequency of 5 Hz with an amplitude of 10 mm, and current inputs of 0, 0.5, 1.0, and 1.5 A respectively. The hysteresis trajectories of the captured damper are obtained by the displacement-controlled dynamic tests on a MTS test system under a variety of working conditions, i.e., frequencies, amplitudes, and damper current inputs (**Figure 3.15**).

In the rolling-vibration experiments, the four MR dampers are connected to the linear VCC by the wire cables. The tests on the integrated system are conducted at ten standard service speeds, i.e., 40, 80, 120, 160, 200, 250, 280, 320, 350 and 380 km/h. For each speed level, the current input I of the four MR dampers is simultaneously tuned from 0 A to the allowable maximum 3.6 A in eight stages, i.e., 0, 0.5, 1.0, 1.5, 2.0, 2.5, 3.0, and 3.6 A.

3.2.2 Rolling-vibration tests on suspension *B*

Rolling-vibration tests are then conducted on the integrated suspension *B*. Similarly, four type-*B* MR dampers (**Figure 3.16**) substitute the original passive dampers to construct the tunable MR secondary suspension, which connect the bogie and the car body in the lateral direction, two in the leading truck and the other two in the trailing truck, depicted in **Figure 3.17**. The power supply is 12 V, and the allowable maximum current input is 2 A. In particular, the saturation current is around 1.4 A, according to the dynamic characterization on the type-*B* dampers which are conducted before the experiments. Thus, the type-*B* dampers are tuned from 0 to 1.4 A in the rolling-vibration experiments. **Figure 3.18** provides a group of hysteretic loops of type-*B* dampers at a frequency of 5 Hz with an amplitude of 10 mm and current inputs of 0, 0.2, 0.4 and 0.6 A.

In the rolling-vibration tests, the EMU prototype runs on the roller rig at seven operating speeds, namely, 120, 160, 200, 250, 280, 320 and 350 km/h. The experiments stop at a speed of 350 km/h where excessive vibrations are observed. At each operating speed, the dynamic performance of the suspension *B* is switched among eight stages, i.e., damper inputs of 0, 0.2, 0.4, 0.6, 0.8, 1.0, 1.2 and 1.4 A, respectively.

3.2.3 Rolling-vibration tests on suspension *C*

Lastly, secondary suspension *C* equipped with four laterally-deployed type-*C* MR dampers (**Figure 3.19**) takes part in the rolling-vibration tests, as shown in **Figure 3.20**. The power supply of the dampers is 12 V, and the maximum current is 2 A. **Figure 3.21** presents the hysteretic loops of type-*C* dampers at a frequency of 3 Hz with an amplitude of 4 mm and current inputs of 0, 0.6, 1.2 and 1.8 A. It can be seen from the dynamic characterization conducted by MTS test system that, type-*A* MR damper can provide the largest control force, up to 20 kN; type-*B* MR damper can only provide smallest control force, which peak damping force is only around 2.5 kN; while type-*C* MR damper come in between, which is capable of peak damping force around 5 kN.

The rolling-vibration tests on the integrated system *C* are conducted at eight standard service speeds, i.e., 80, 120, 160, 200, 250, 280, 320, and 350 km/h. The tests stop at a speed of 350 km/h, since significant oscillations of vehicle occur. For each speed level, the current input I of the four MR dampers is simultaneously tuned from 0 A to the allowable maximum 2 A in six stages, i.e., 0, 0.4, 0.8, 1.2, 1.6 and 2 A. Therefore, there are totally 48 test scenarios. At each test scenario, the vehicle prototype runs on straight track with random irregularities collected from Guangzhou-Wuhan high-speed rail line, so as to stimulate vehicle dynamic behaviors that approach those in service operation.

3.3 Ride comfort index

In order to quantify the vibration level of the carriage and assess the dynamic performance of the MR suspension, the simplified formula for evaluating passenger ride comfort stipulated in UIC Code 513 (1994) is employed. The simplified method is based solely on the accelerations measured at the center and at two ends of the carriage at the floor level, seen in **Figure 3.22**. The duration of the measuring period is 5 minutes. The root-mean-square (RMS) values of these measured accelerations are made use of to characterize ride comfort. The comfort index is formulated as:

$$N_{MV} = 6\sqrt{\left(a_{XP95}^{W_d}\right)^2 + \left(a_{YP95}^{W_d}\right)^2 + \left(a_{ZP95}^{W_b}\right)^2} \quad (3.1)$$

where a_{XP}, a_{YP}, and a_{ZP} is the RMS values of the accelerations obtained at the measured point in the longitudinal, lateral, and vertical direction, respectively; the upper index W_d relates to frequency-weighted values according to the horizontal weighting curves seen in **Figure 3.23**. The frequency weighting is made because of human physiological sensitivity to different frequency ranges, in particular in the 0.5 – 5 Hz frequency range;

the lower index 95 refers to the 95^{th} percentile. Since the vibration of railway vehicles tend to fluctuate, rather than are stationary, the weighted RMS values are calculated for a period of 5 seconds to take account of these fluctuations. The statistical values for a prescribed percentile, i.e., the 95^{th} percentile, are selected as the effective RMS values to represent the ride comfort. Therefore, calculation of the comfort index by Equation (3.1) follows the sequences as:

(i) the measured accelerations go through the horizontal frequency weighting W_d;

(ii) the RMS values are calculated every 5 seconds;

(iii) a statistical analysis of these RMS values are conducted for a period of 5 minutes;

(vi) mean comfort indices are calculated.

The comfort of the passenger is evaluated at the various operating speeds of the vehicle which actually occur in practical service. The comfort index is rated from poor to good comfort with a decreasing value. Smaller the index is obtained, better the passenger ride quality is indicated.

In particular in these experiments, since the aim is to study the impact of the laterally-deployed MR dampers on transverse motions of the rail vehicle, only the lateral component of the comfort index is devised. The obtained ride comfort index would indicate the effectiveness of the dampers on mitigating the vibration on each specified operating condition, i.e., operating speed and current input. Therefore, the ride comfort index is devolved into:

$$N_{MV} = 6\left|a_{YP95}^{W_d}\right| \tag{3.2}$$

where α_{YP} denotes the lateral accelerations measured at floor level of the carriage. In the present study, the lateral component (rating) below 1 is considered as an acceptable comfort level. It is worth noting that, the frequency responses in the frequency range of 0.4 to 5.0 Hz, especially between 0.6 and 2.0 Hz, contribute considerably to the rating index. Therefore, attenuating vibration in this frequency region is important for the constructed suspension.

3.4 Result and discussion

3.4.1 Rolling-vibration tests on suspension *A*

The rolling-vibration tests on suspension *A* are conducted at 10 speed levels from 40 to 380 km/h, with current inputs to the four type-*A* MR dampers being simultaneously tuned from 0 to 3.6 A. It is observed that, when the running speed is increased to 160 km/h and the current input is tuned to 1.0 A, the vehicle becomes unstable, which is signaled by a clearly visible periodic motion. **Figure 3.24** shows a comparison of car body acceleration response in a stable condition (I = 0.5 A) and in the unstable condition (I = 1.0 A) at a speed of 160 km/h. As the current input rises to 1.0 A, the resonant vibration at 1.9 Hz is excited. The peak acceleration of the car body rises considerably to 1.5 m/s^2. As the speed increases to 200 km/h and the imposed current is tuned to 0.5 A, the instable behavior occurs. It is indicated that, the type-*A* dampers at passive-on state are too stiff for the vehicle when the running speed exceeds 200 km/h. Therefore, the remaining tests are conducted only at the damper passive-off state, i.e., with null current input to the MR dampers.

The measured lateral accelerations of the car body are analyzed to obtain the ride comfort rating. The accelerations are filtered with a band pass filter in the frequency range of 0.4 to 80 Hz, and then weighted to calculate the UIC ride comfort index according to Equation (3.1). The rating is plotted in **Figure 3.25**. The zero values refer to the cases when rolling-vibration test was not conducted due to the potentially unstable oscillation.

Figure 3.26 demonstrates the different ride comfort rating of the car body under different running speeds at damper passive-off state. **Figure 3.27** shows the lateral acceleration amplitude spectra at the speeds of 80, 200, 320 km/h. It can be seen that, there is no dominant mode governing the car body vibration. Instead, the car body undergoes forced vibration in a wide frequency range. At speed of 80 km/h, the car body experiences much vibration in the frequency range of 0.6 to 2 Hz, thus causing a less comfortable ride. At speed of 200 km/h, high-frequency components are slightly intensified, while low-frequency components are, especially of 1.9 Hz, are mitigated, which results in a slight improvement in the comfort rating. As the vehicle accelerates to 320 km/h, the car body undergoes large vibration at the frequencies of 1.9 and 2.8 Hz, and thus a worse ride condition is devised. In summary, the operating speed has a strong and diverse influence on the vehicle dynamics. In view of the fact that human body is extremely sensitive to motions in the frequency range of 0.4 to 5 Hz, the optimal state of the MR suspension should be tuned to a level where the unfavorable frequency components is suppressed.

At the lower operating speeds (40 and 80 km/h), the vehicle generally obtains satisfactory ride comfort (lower than 0.7). At speed of 40 km/h, the rating is 0.5 at the passive-off state, and degrades to 0.7 as the current increases to 0.5 A, and then maintains around 0.5 for the remaining passive-on states. **Figure 3.28** shows the acceleration amplitude spectra of the car body at speed of 40 km/h and with 0 and 0.5 A current inputs. It is observed that, the vibration patterns are similar, both in broadband responses. As the passive-on state turns on, the oscillation aggravates in both lower and higher frequency regions. At speed of 80 km/h, the rating is generally around 0.67. The maximum (worst) one happens at the passive-on state of 2 A. **Figure 3.29** shows the comparison of acceleration spectra with null and 2 A current inputs. A similar increase in both lower and higher frequency regions is observed. At speed of 120 km/h, the best comfort rating is about 0.5 at passive-off state. The rating degrades to 0.9 as the current input increases, and reaches the peak value 1.3 with 2.5 A current input. **Figure 3.30** shows the acceleration amplitude spectra at speed of 120 km/h. It is observed that, as the passive-on state turns on, the motion responses over the whole frequency are amplified.

Since there is a potential of instability in oscillation at increasing speeds, only limited experimental data are collected to assess the dynamic performance of suspension *A*. In general, the dynamic response of the car body in both lower and higher frequency regions varies with the change in current input. However, the classic trade-off between the resonant vibrations and higher-frequency oscillation is not observed when switching the passive state of the suspension. It is probably due to little relative motions between the bogies and carriage. In other words, the type-*A* MR dampers seems to perform as the spring components, or even joints, to transmit energy from the bogies to the car bogy, rather than as the damping components to attenuate motion, which would certainly result in the degraded ride comfort. To conclude, the type-*A* MR dampers are too stiff, making them effective only at lower speeds.

3.4.2 Rolling-vibration tests on suspension *B*

The rolling-vibration tests on suspension *B* are then followed at seven speed levels from 120 to 350 km/h. The maximum operation load of the type-*B* MR dampers is around 9 kN. For each speed level, the current input to the four MR dampers is switched simultaneously between eight levels from 0 to 1,4 A. **Figure 3.31** shows the lateral ride comfort rating of the car body obtained under different operating conditions. The vehicle generally exhibits stable dynamics with the ride comfort rating below 1.2. However, as the vehicle accelerates to 350 km/h, considerably large vibration is observed, and a substantial deterioration in ride quality is obtained. Consequently, the rolling-vibration tests stop at this speed level.

Figure 3.32 illustrates the lateral ride comfort rating of the car body at damper passive-off state. In comparison to suspension *A*, suspension *B* demonstrates a more favorable performance of vibration attenuation at a speed of 320 km/h, though it turns poor at a speed of 350 km/h. **Figure 3.33** shows the acceleration amplitude spectra of the car body obtained at different speeds. It is observed that, broadband responses, rather than dominant modal vibrations, are excited. As the vehicle speeds up to 200 km/h, low-frequency vibration components become larger, resulting in a slight deterioration in ride quality. At speed of 320 km/h, the vehicle vibrates less in low-frequency region but more in high-frequency region. Since the comfort rating is more sensitive to the low-frequency components, a more favorable rating is obtained. As the vehicle speeds up to 350 km/h, however, a substantial increase in vibration in all frequency regions is observed. It is indicated that, the passive-off damping of the System B is insufficient to suppress the lateral vibration of the vehicle at speed of 350 km/h.

As the vehicle operates between 120 to 280 km/h, the ride quality exhibits variations in a narrow range when increasing the current input. For example, the comfort rating varies between 1.0 and 1.2 at operating speed of 120 km/h. It is interesting to note that, energy transmission between low and high frequency region occurs with change at passive state. At speed of 120 km/h, the vibration component in low-frequency range are aggravated as the current is tuned to 0.4 A (**Figure 3.34**). At speed of 160 km/h, the low frequency vibration component is excited as the current is tuned to 0.2 A (**Figure 3.35**). Although the high frequency vibration component is suppressed to some extent, the increased low frequency response, especially in the frequency range of 0.4 to 5 Hz, causes the deterioration in comfort rating. On the other hand, at speed of 250 km/h, resonant vibration is attenuated with current input tuned to 0.4 A (**Figure 3.36**), resulting in an improvement in comfort rating. In general, the improvement or deterioration in the ride quality is compliant with the attenuation or amplification of resonant oscillations. Although the vehicle demonstrates diverse dynamic behaviors at speeds of 120 to 280 km/h, the optimal state of the system can be determined with current input between 0 and 0.4 A.

As the vehicle runs at speed of 320 km/h, the comfort rating exhibits a rather obvious trend with regard to the current input. The optimal working condition is observed at damper passive-off state where comfort rating is only 0.5. As the damper passive-on state is on, the rating degrades at its onset and reaches its maximum (worst) value with 0.8 A current input, and then slightly improve as the current input is increased, as demonstrated in **Figure 3.37**. **Figure 3.38** shows the lateral acceleration amplitude spectra of the car body. At the passive-off state, the low-frequency vibration component is suppressed. However, as the current input is imposed, the vibration components in the frequency range of 0 to 8.0 Hz aggravate significantly, resulting in a reduction in comfort rating.

Because the vibration of the car body is transmitted from the bogie via connecting components, i.e., dampers and springs, it is reasonable to examine the bogie dynamics to complementarily assess the performance of the suspension. A statistical analysis method (Mantaras and Luque 2006) is applied to evaluate the measured acceleration of the vehicle bogies. The root mean square (RMS) of the bogie accelerations is calculated every 1 second. Then the 95 percentile value is selected to characterize the bogie dynamics. **Figure 3.39** shows the statistical histogram of the bogie acceleration at a speed of 320 km/h. It can be seen that, the effective acceleration of the bogie increases slightly from 0.36 m/s^2 at the passive-off state to 0.4 m/s^2 at the passive-on state with 1.4 A current input. It indicates that the vibrations of the car body (carriage) and the bogie are relatively independent. The lateral acceleration amplitude spectra of the bogie at speed of 320 km/h are illustrated in **Figure 3.40**. Consistent with the observed effective acceleration, the response spectra exhibit only minor fluctuations over the whole frequency range with different current inputs. No substantial variation is observed. The smallest bogie acceleration devises from the passive-off state with null current input.

As the vehicle speeds up to 350 km/h and the type-*B* MR dampers are at passive-off state, the car body experiences intense vibration. The comfort rating is evaluated to be 2.9 (**Figure 3.41**), indicating a very uncomfortable ride status. As the current input increases, a general improvement of the ride quality is observed. The best (minimum) rating is achieved with the 1.4 A current which is the saturation current of the type-*B* dampers. The lateral acceleration amplitude spectra of the car body are shown in **Figure 3.42**. A considerable variation of the frequency-domain response is observed. At the damper passive-off state, the car body motion is primarily the low-frequency components. As the current is tuned to 0.6 A, a trade-off between the low-frequency oscillation aggravation and high-frequency vibration suppression is attained. Owing to the higher weighting of low-frequency oscillation in evaluating the ride comfort rating, a slight improvement (decrease) in the comfort rating is obtained. As the current is tuned to 1.0 A, the response components in the frequency range of 0 to 10 Hz is further suppressed, resulting in an even better comfort rating. As the current input is finally increased to 1.4 A, the low-frequency motions are attenuated, while the high-frequency response components remain almost the same as the ones with 1.0 A current input. Consequently, the comfort rating is improved to be 1.2.

The dynamic behavior of the bogie at speed of 350 km/h is also evaluated. **Figure 3.43** and **Figure 3.44** show the 95 percentile RMS response and the acceleration amplitude spectra, respectively. Compared to the bogie dynamics at speed of 320 km/h, the effective acceleration of the bogie becomes larger, but is still less affected by the changing current inputs. Similarly, the vibrations of the bogie and the car body are relatively independent, indicating the insignificant transmission of vibration energy between the two vehicle parties. Therefore, it can be inferred that, the vibration energy of the car body is dissipated primarily by the incorporated MR dampers. In view of the considerable vibration of the car body at the damper passive-off state at speed of 350 km/h and beyond, the type-*B* MR dampers with lower adjustable damping forces would be more appropriate for high-speed rail applications.

3.4.3 Rolling-vibration tests on suspension *C*

Lastly, rolling-vibration tests are conducted on secondary suspension *C* equipped with type-*C* MR dampers. The system operates at a variety of standard service speeds from 80 to 350 km/h, which are 80 km/h, 120 km/h, 160 km/h, 200 km/h, 250 km/h, 280 km/h, 320 km/h, and 350 km/h. The tests stop at a speed of 350 km/h, since excessive vibrations of vehicle are observed. For each speed level, the type-*C* MR dampers is simultaneously tuned among six passive levels of current input from 0 to 2 A, i.e., 0 A, 0.4 A, 0.8 A, 1.2 A, 1.6 A, and 2 A. At each test scenario, the integrated vehicle is driven by random track irregularities collected from Guangzhou-Wuhan HSR, so that the vehicle dynamic behaviors that approach those in service can be stimulated. The car body accelerations are evaluated and analyzed in what follows.

Figure 3.45 shows the lateral ride quality rating of the test vehicle at damper passive-off states (I = 0 A) under a variety of service speeds. As can be seen from the graph, the comfort rating generally deteriorates as the running speed increases, except for that at a speed of 160 km/h where the ride experience exhibits a sharp increase.

Focus on car body dynamics of train vehicle running at a speed of 160 km/h. **Figure 3.46** shows the lateral ride quality rating of the train vehicle car body with a series of current input from 0 A to 2 A. The rating exhibits a controlled trend with regard to the increasing type-C damper, that the ride quality improves as the current is tuned bigger to 0.4 A, and then tremendously deteriorates afterwards. The optimal state of the suspension C can be observed with the current input of 0.4 A. **Figure 3.47** presents the lateral acceleration amplitude spectra of the car body with current input of 0 A, 0.4 A, 1.2 A and 2 A. It can be observed that, car body broadband responses, rather than major resonance motions, are excited. As the current input increases from 0 A to 0.4 A, the low-frequency oscillation components below 2 Hz is suppressed, resulting an improvement in the comfort rating. As the current input is tuned bigger to 1.2 A and 2 A, there is not apparent variation in the frequency-domain response. The high-frequency motions remain stable, while the low-frequency responses considerably aggravate. And accordingly, gradual deterioration in ride comfort occurs.

As the vehicle runs at a speed of 350 km/h and suspension C is at passive-off, the ride experience is much worse than those at lower running speeds. **Figure 3.48** shows the lateral ride quality rating with a series of current input from 0 A to 2 A. It is observed that, the ride experience improves as the current input of the suspension C increases, and reaches the optimal state when current input is adjusted to 0.8 A, and then degrades gradually as the current input increases subsequently. The lateral acceleration amplitude spectra of the car body with current input of 0 A, 0.8 A and 2 A are depicted in **Figure 3.49**. Dominant modal motion of train vehicle, which is around 2 Hz, is observed at the speed of 350 km/h. As the controlled current of suspension *C* is tuned from 0 A to 0.8 A, the low-frequency vibrations are slightly suppressed, yielding an improvement in the ride comfort rating. While the current is adjusted gradually to 2 A, both the low-frequency and the high-frequency vibrations increase to some extent. Accordingly, the corresponding ride comfort rating rises considerably.

3.5 Summary

As part of investigation on developing MR secondary suspension for ride comfort improvement for high-speed trains, an experimental study on three MR secondary suspensions is presented in this chapter. Three types of MR dampers (type-*A*, type-*B* and type-*C*) in different control ranges were designed, manufactured and incorporated into the EMU secondary suspension. The full-scale high-speed train vehicle integrated with the developed MR dampers was tested on a roller rig at speeds of 40 to 380 km/h and with random track irregularities collected from Guangzhou-Wuhan HSR. The acceleration responses of the car body and bogie were measured using optical fiber accelerometers. The ride comfort rating of the car body was obtained to evaluate the dynamic performance of the three MR secondary suspensions. Some findings are summarized as follows.

(i) The rolling-vibration tests on System *A* revealed that, the type-*A* MR dampers is favorable only when the vehicle operates at low speeds. When the operating speed reached 160 km/h and beyond, the vehicle tends to be unstable with the current input tuned to a certain level. In such situations, the car body is sensitive to the change in current input. Because of the little relative motions between the bogie and car body, the MR dampers perform like a spring component to transmit vibration energy from the bogie to the car body, without significant energy dissipation. Therefore, the damping of the type-A MR dampers is too hard for suppressing the lateral vibration of the rail vehicle operating at high speeds.

(ii) The secondary suspension incorporating the type-*B* MR dampers exhibits better energy dissipation capability. The optimal state of the MR suspension (the optimal current input to the MR dampers) with best ride comfort of the car body was obtained for each running speeds in tests. It is observed that, the suppression of the low-frequency response components is greatly beneficial to improving the ride quality. With the appropriate current input, the trade-off between the low-frequency and high-frequency motion can be achieved, verifying the effectiveness of the MR secondary suspension in adjusting the damping. However, the secondary suspension with type-*B* MR dampers at the passive-off state with null current input is incapable of mitigating the car body lateral vibration when the speed exceeds 350 km/h.

(iii) Type-*C* MR dampers with the more appropriate damping force range have been developed to construct a more effective MR secondary suspension. Controllable trend can be observed. Results of car body dynamics at speeds of 160 km/h and 350 km/h are presented. In both case, the ride comfort rating is firstly improved as the current input increases from 0 A, and is gradually deteriorated as the current input increases to 2 A. At a speed of 160 km/h, the optimal state where the ride comfort rating reach minimum value is identified as the current input is 0.4 A. At a speed of 350 km/h, the optimal state is identified as the current input is 0.8 A. It is implied that, type-*C* MR dampers exhibits more effective controlled capability for CRH3 vehicle.

Figure 3.1 High-speed train prototype CRH3 EMU for tests

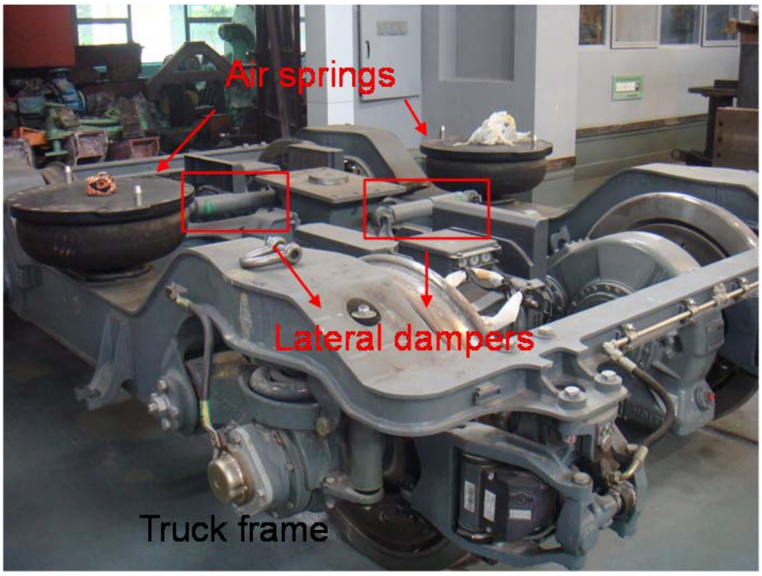

Figure 3.2 Secondary suspension

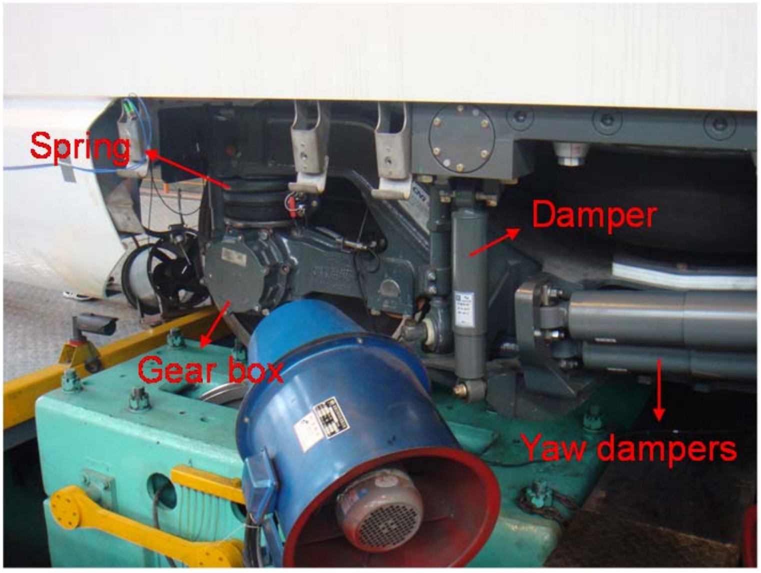

Figure 3.3 Primary suspension

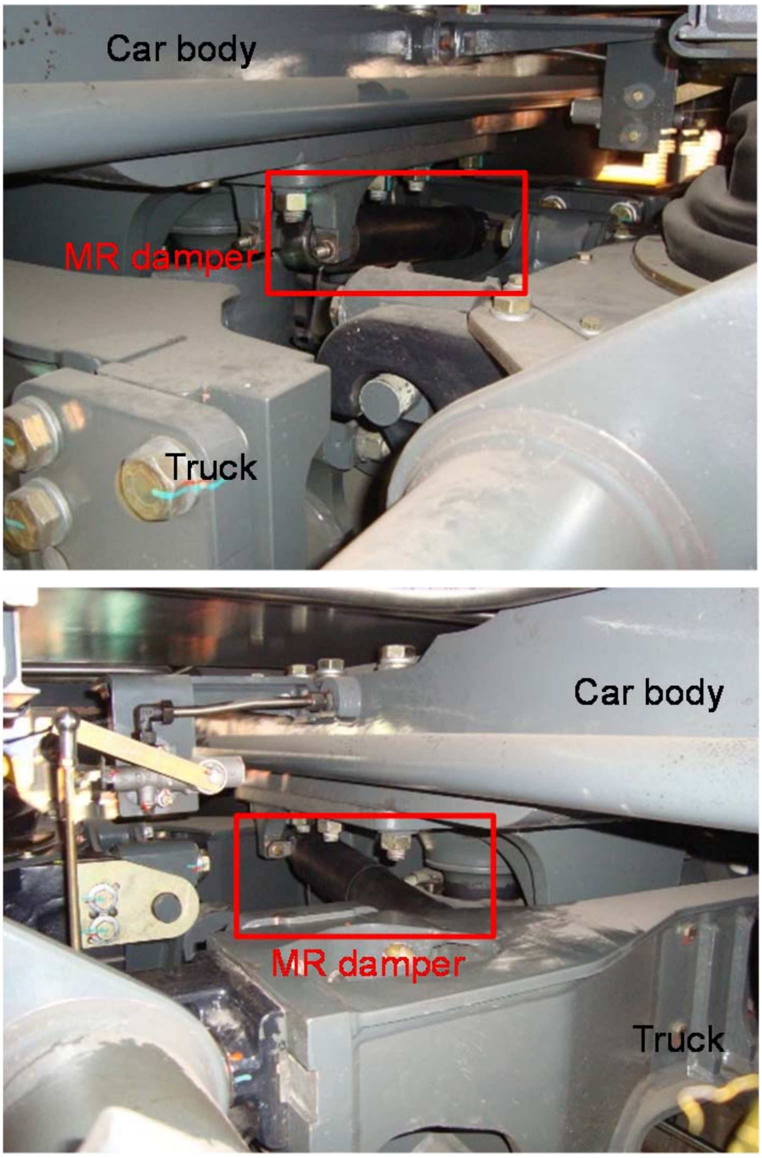

Figure 3.4 MR dampers installed in secondary suspension

Figure 3.5 Linear VCC

Figure 3.6 Test plant

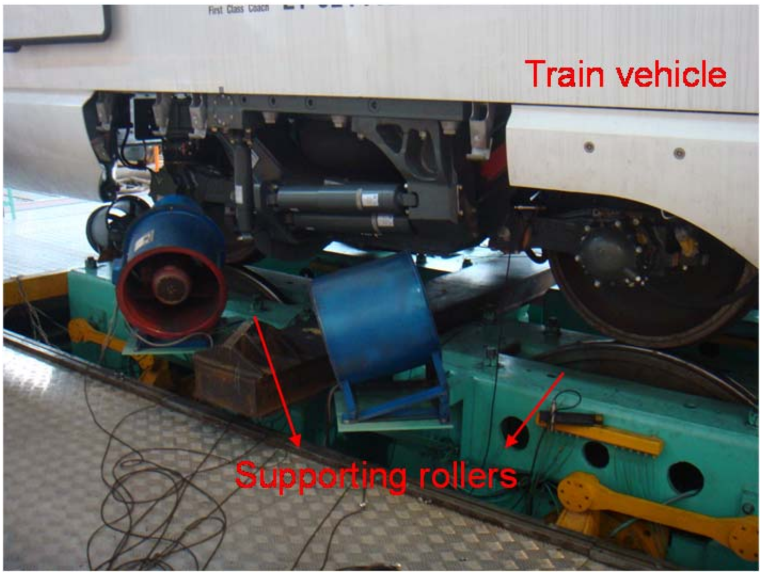

Figure 3.7 Supporting rollers underneath vehicle wheelset

(a) Constraint at the front

(b) Constraint at the back

Figure 3.8 Constraints of CRH vehicle in longitudinal direction

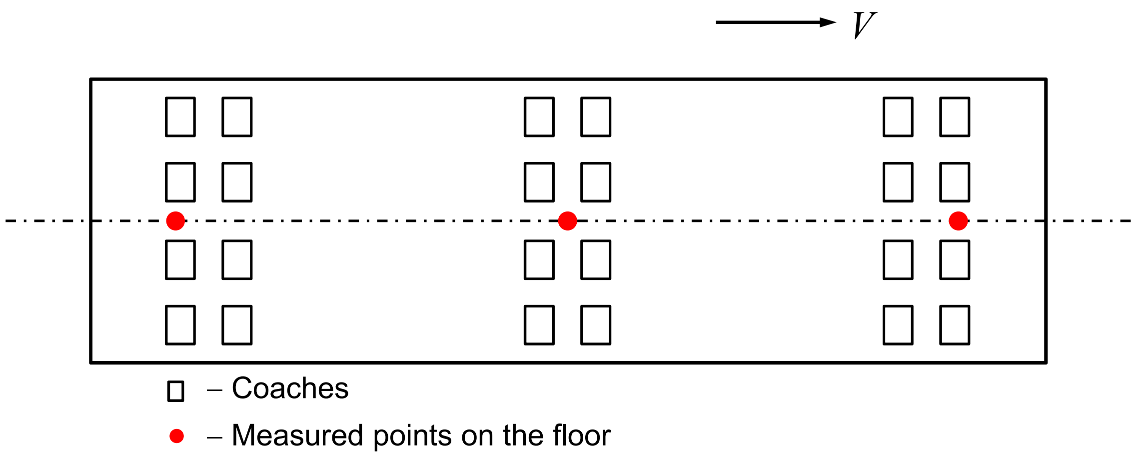

(a) Measured points in car body

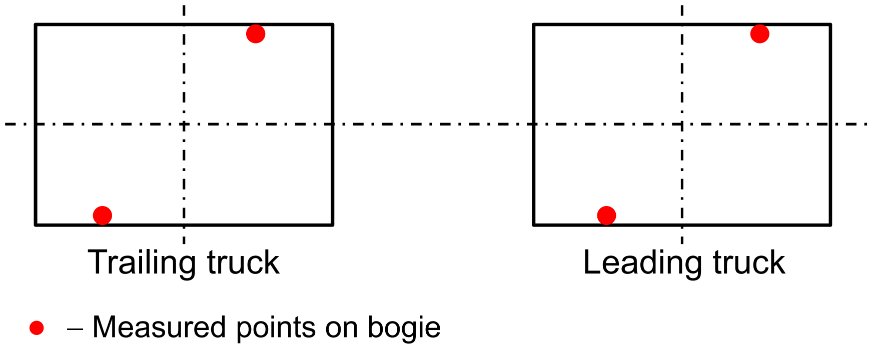

(b) Measured points on bogie

Figure 3.9 Measured points of test vehicle

(a) Accelerometer at the floor level in car body

(b) Accelerometer at the bogie

Figure 3.10 Optical fiber accelerometers deployed at car body and bogie

Figure 3.11 Interrogator SM130

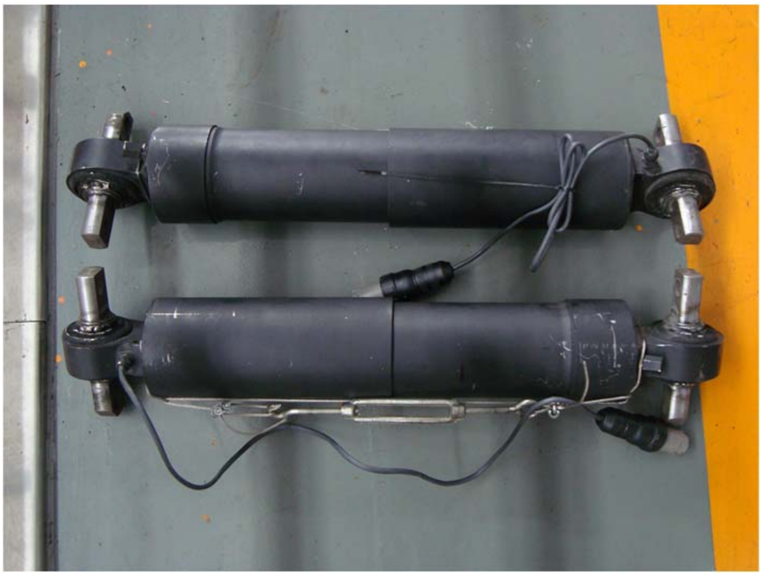

Figure 3.12 Prototypes of type-*A* MR damper

Figure 3.13 Laterally-deployed type-*A* MR damper in secondary suspension of tested EMU train vehicle

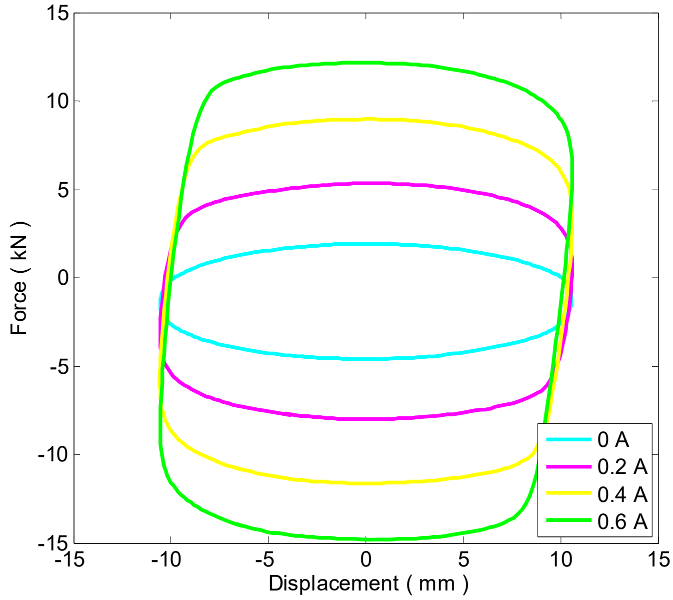

(a) Force-displacement hysteresis loops

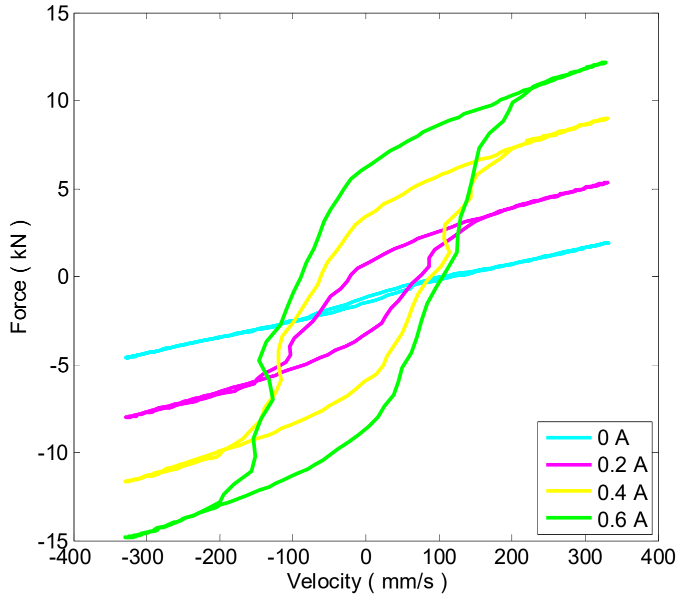

(b) Force-velocity hysteresis loops

Figure 3.14 Dynamic hysteresis behavior of type-*A* MR dampers at a frequency of 5 Hz with an amplitude of 10 mm, and current inputs of 0, 0.5, 1.0, and 1.5 A

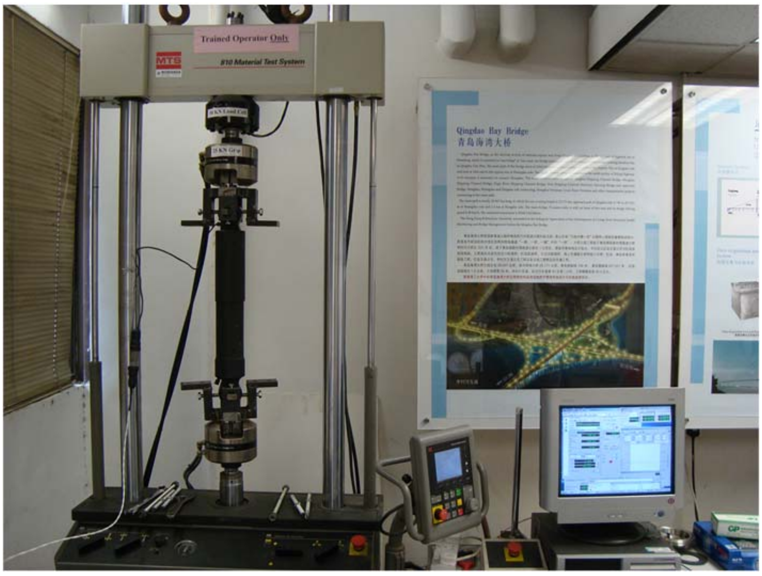

Figure 3.15 Dynamic characterization of MR damper conducted on MTS test system

Figure 3.16 Prototypes of type-*B* MR damper

Figure 3.17 Laterally-deployed type-*B* MR damper in secondary suspension of tested EMU train vehicle

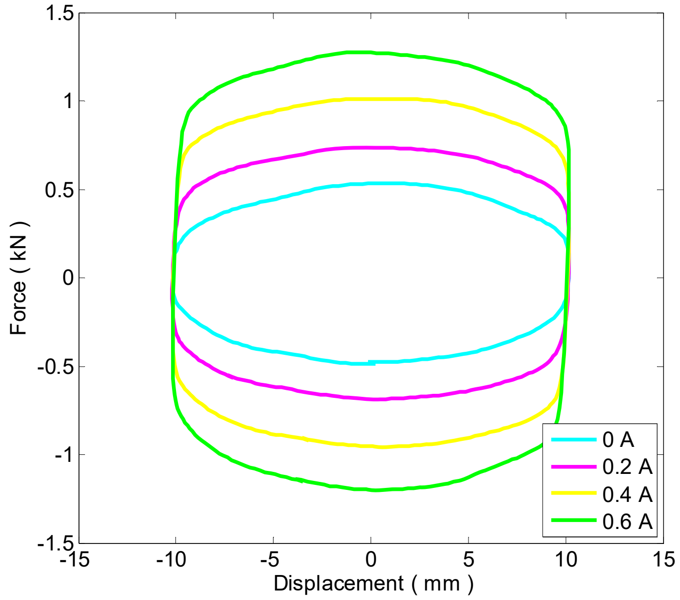

(a) Force-displacement hysteresis loops

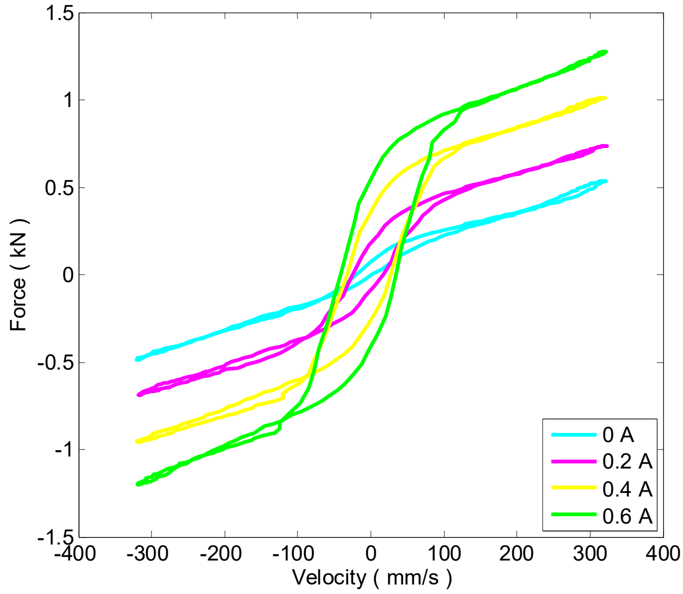

(b) Force-velocity hysteresis loops

Figure 3.18 Dynamic hysteresis behavior of type-*B* MR dampers at a frequency of 5 Hz with an amplitude of 10 mm, and current inputs of 0, 0.2, 0.4, and 0.6 A

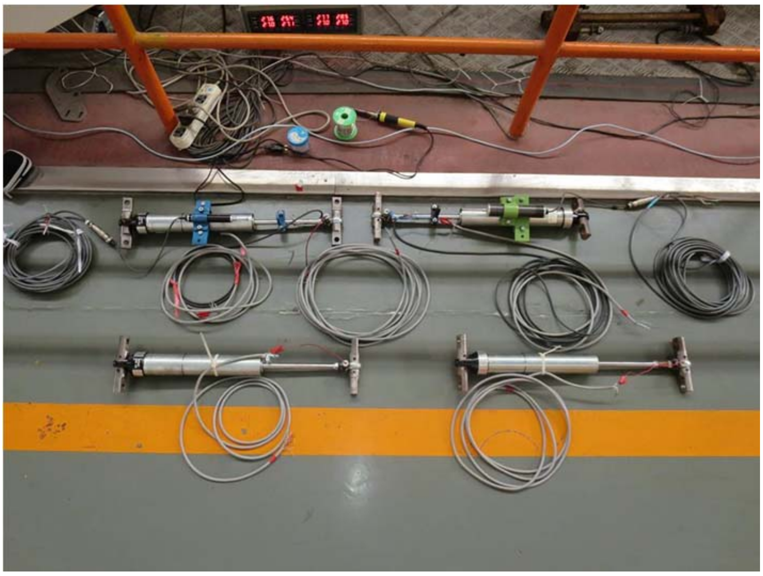

Figure 3.19 Prototypes of type-*C* MR damper

Figure 3.20 Laterally-deployed type-*C* MR damper in secondary suspension of tested EMU train vehicle

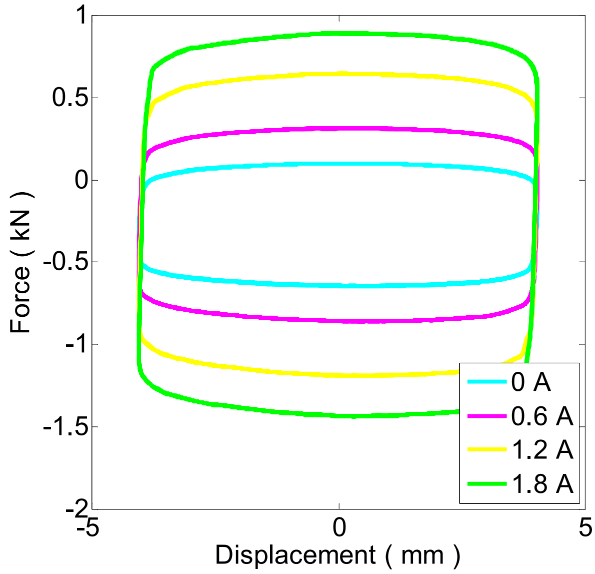

(a) Force-displacement hysteresis loops

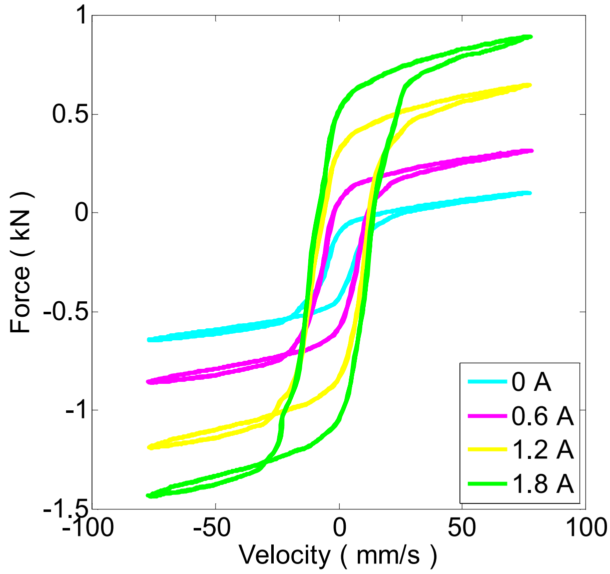

(b) Force-velocity hysteresis loops

Figure 3.21 Dynamic hysteresis behavior of type-*C* MR dampers at a frequency of 3 Hz with an amplitude of 4 mm, and current inputs of 0, 0.6, 1.2, and 1.8 A

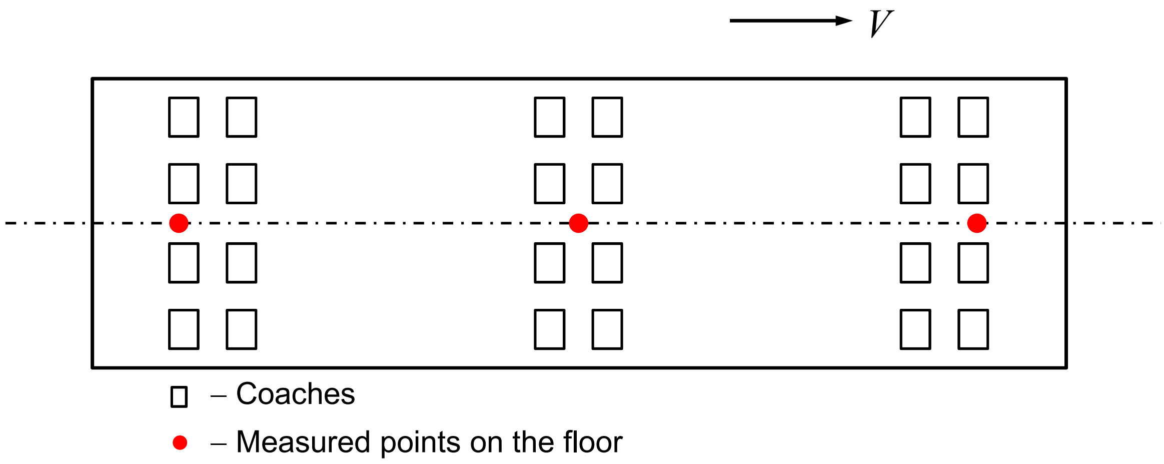

Figure 3.22 Acceleration measuring points on the carriage floor

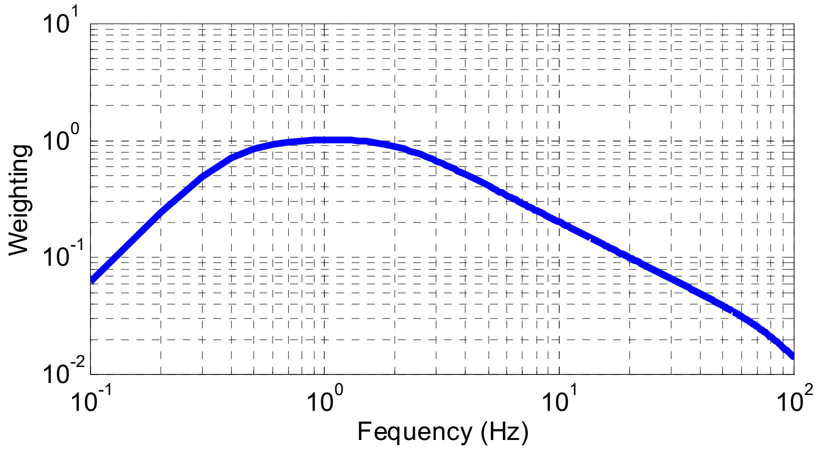

Figure 3.23 Frequency weighting filter W_d

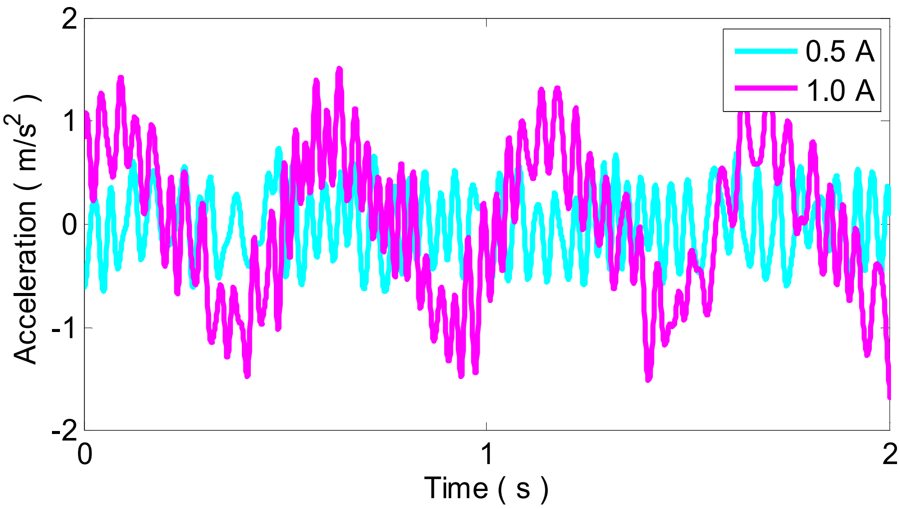

(a) Acceleration time history

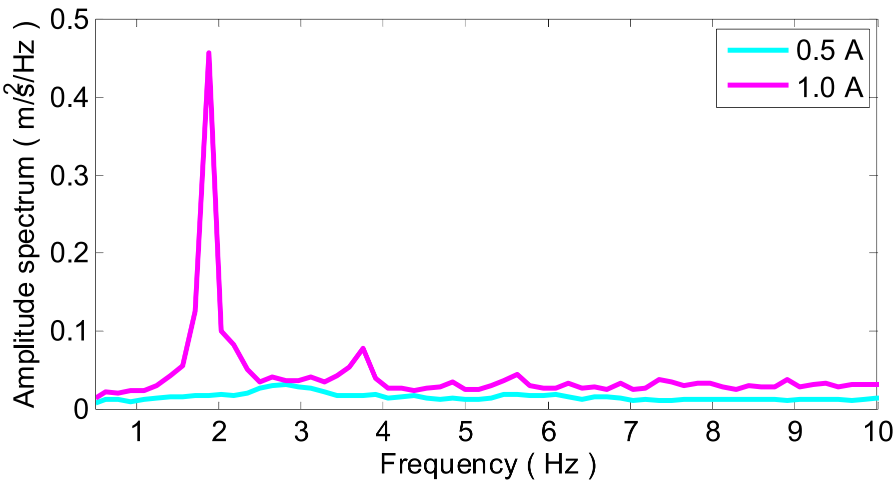

(b) Acceleration amplitude spectrum

Figure 3.24 Lateral vibration of car body at running speed of 160 km/h

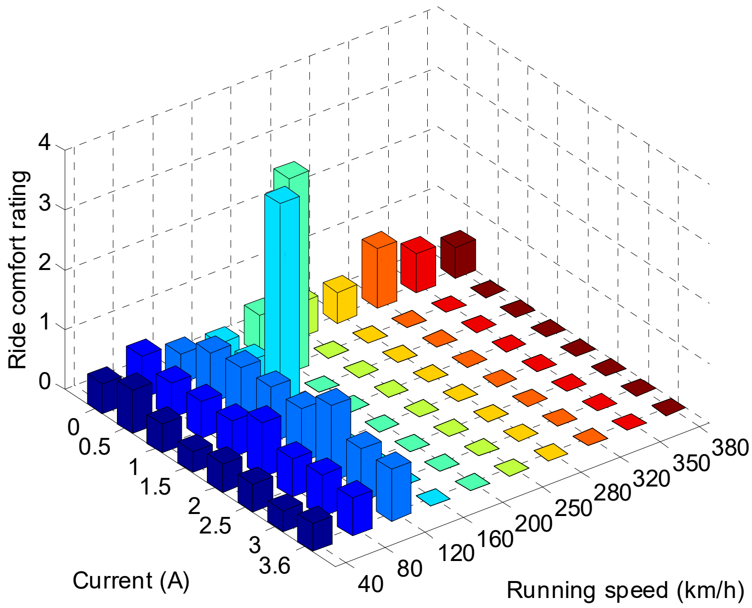

Figure 3.25 Ride comfort rating of EMU tested

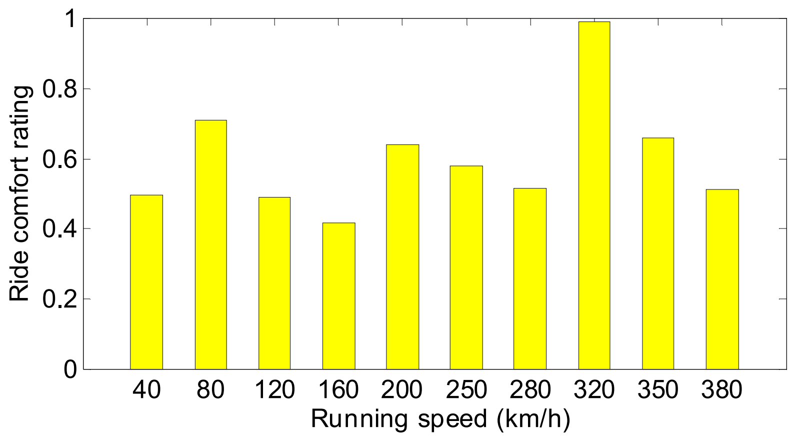

Figure 3.26 Ride comfort rating at damper passive-off state

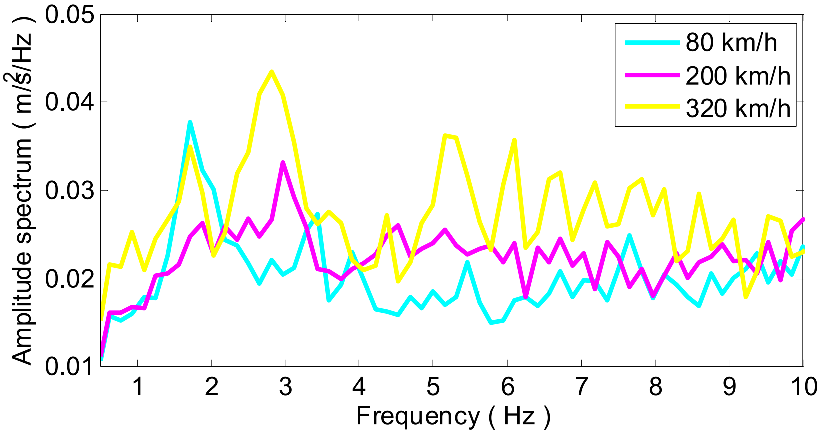

Figure 3.27 Amplitude spectrum of lateral acceleration of car body at damper passive-off state

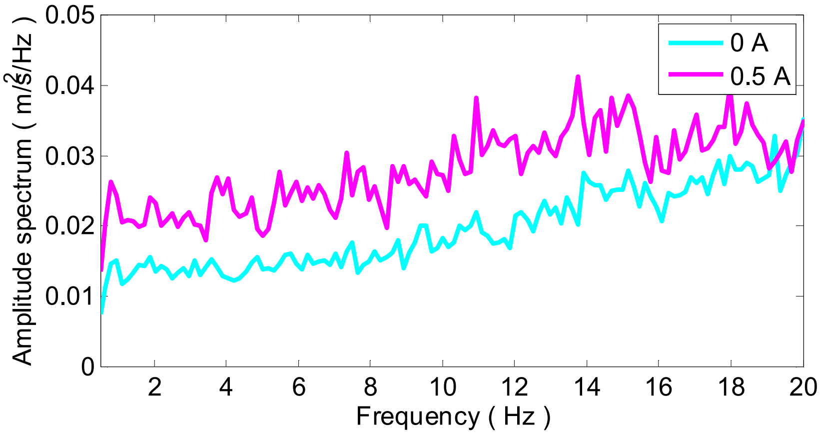

Figure 3.28 Amplitude spectrum of lateral acceleration of car body at running speed of 40 km/h

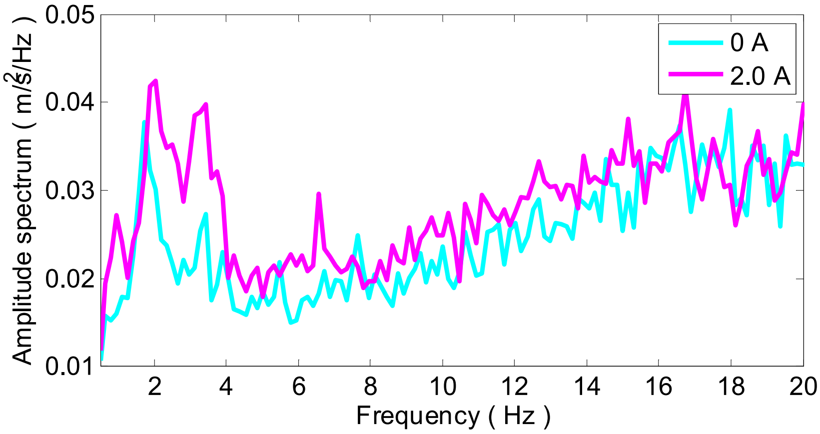

Figure 3.29 Amplitude spectrum of lateral acceleration of car body at running speed of 80 km/h

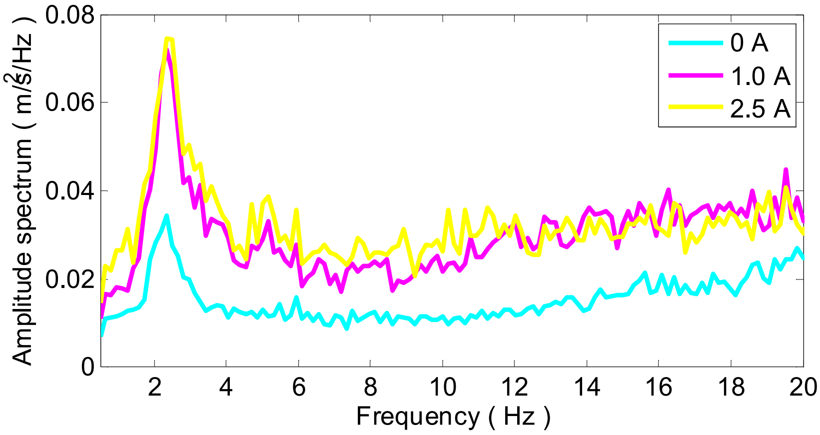

Figure 3.30 Amplitude spectrum of lateral acceleration of car body at running speed of 120 km/h

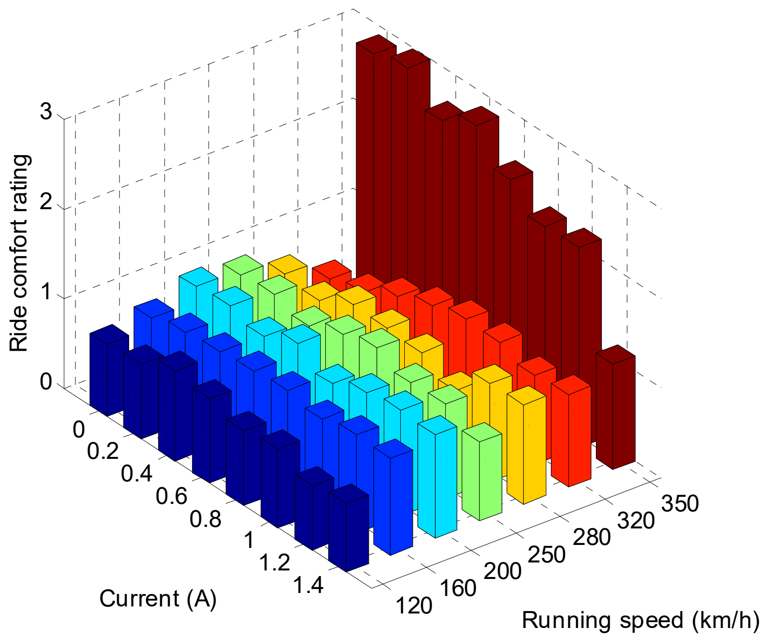

Figure 3.31 Ride comfort rating of trailer car tested

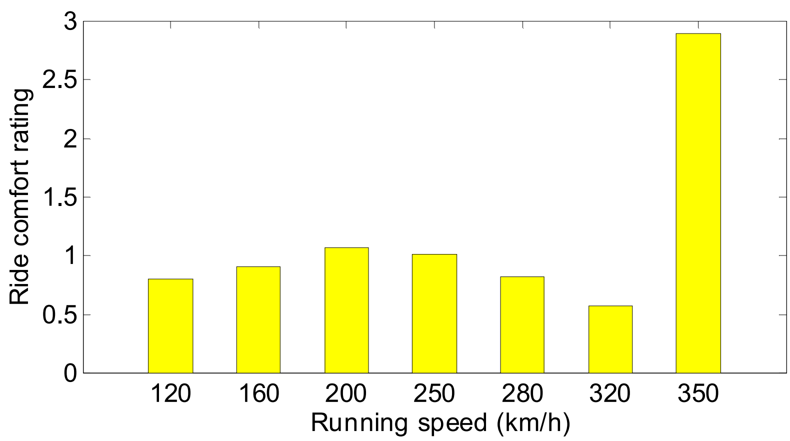

Figure 3.32 Ride comfort rating at damper passive-off state

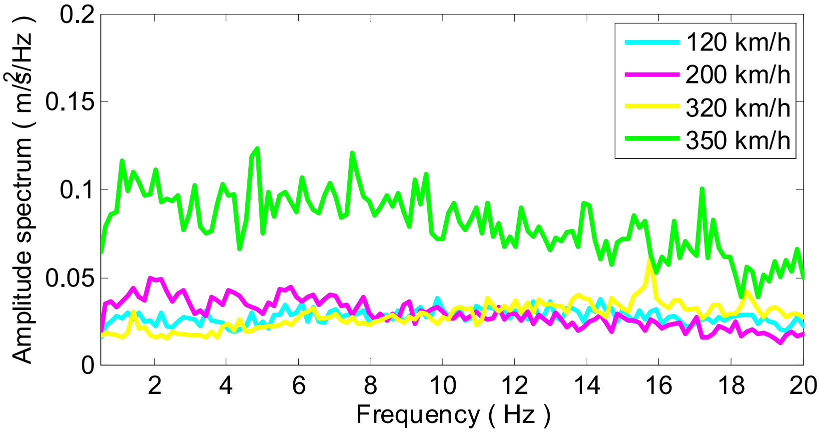

Figure 3.33 Amplitude spectrum of lateral acceleration of car body at damper passive-off state

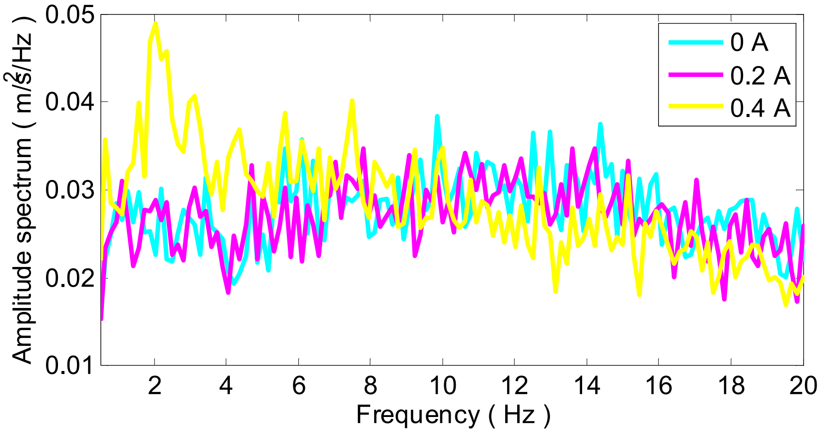

Figure 3.34 Amplitude spectrum of lateral acceleration of car body at running speed of 120 km/h

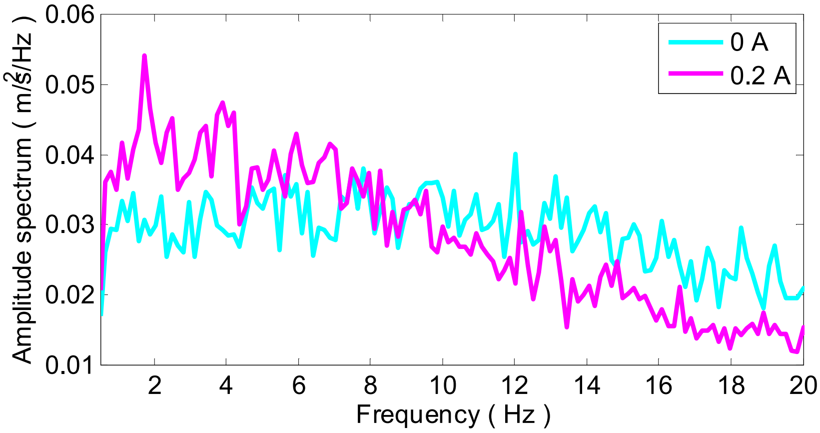

Figure 3.35 Amplitude spectrum of lateral acceleration of car body at running speed of 160 km/h

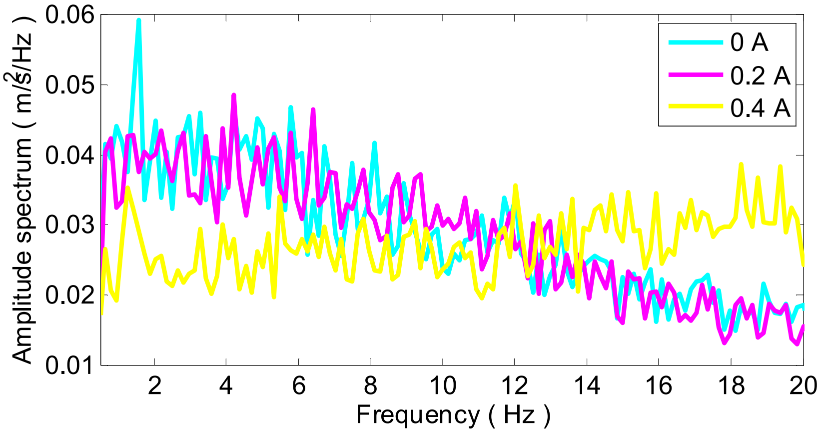

Figure 3.36 Amplitude spectrum of lateral acceleration of car body at running speed of 250 km/h

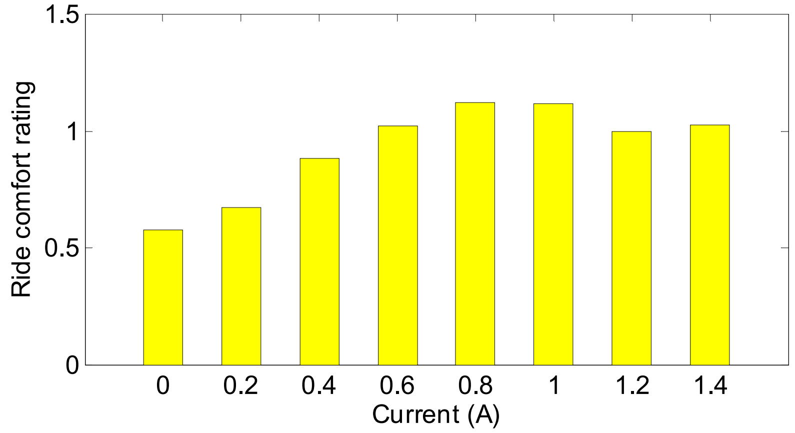

Figure 3.37 Ride comfort rating at speed of 320 km/h

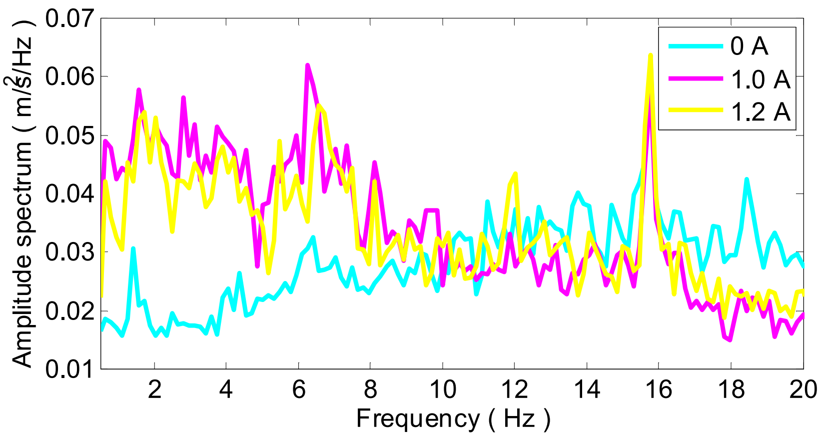

Figure 3.38 Amplitude spectrum of lateral acceleration of car body at speed of 320 km/h

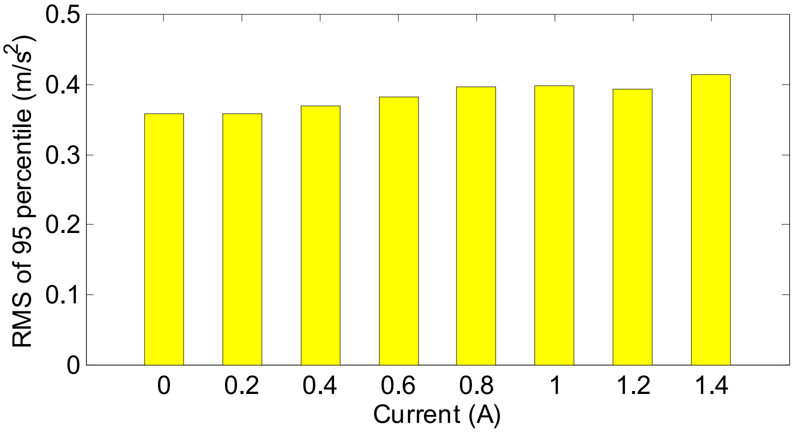

Figure 3.39 95 percentile of RMS values of bogie lateral acceleration at speed of 320 km/h

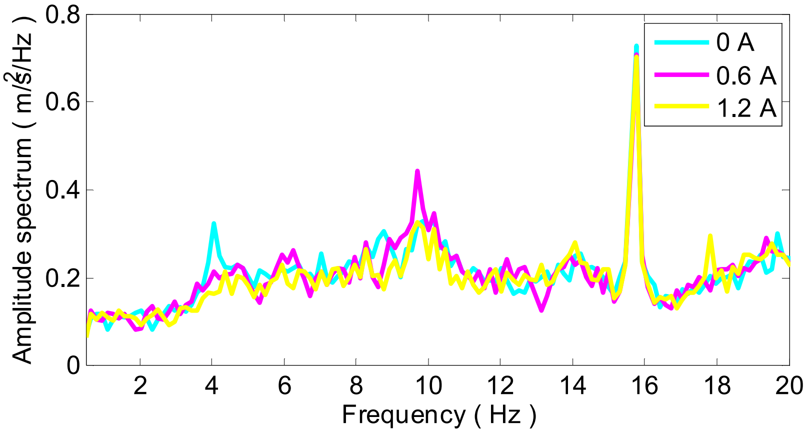

Figure 3.40 Amplitude spectrum of lateral acceleration of bogie at speed of 320 km/h

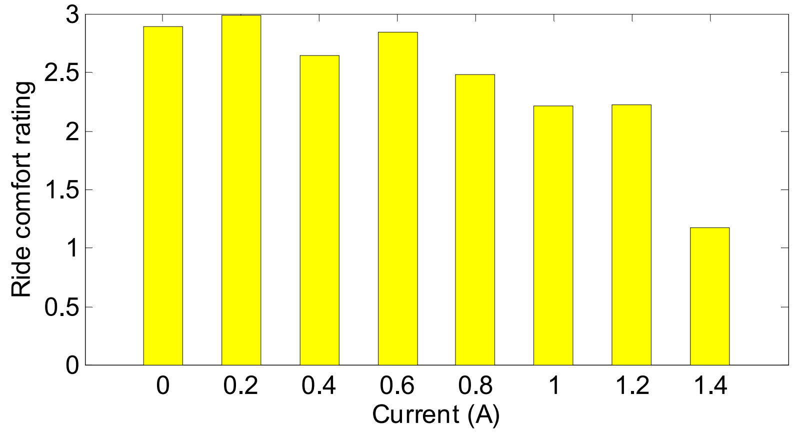

Figure 3.41 Ride comfort rating at speed of 350 km/h

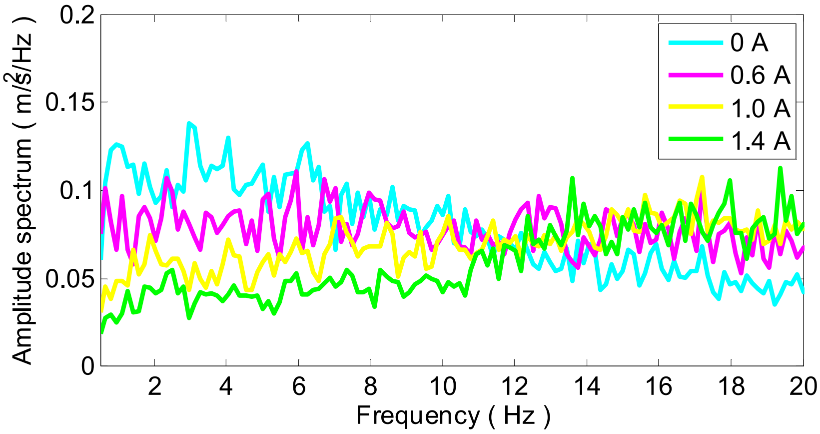

Figure 3.42 Amplitude spectrum of lateral acceleration of car body at speed of 350 km/h

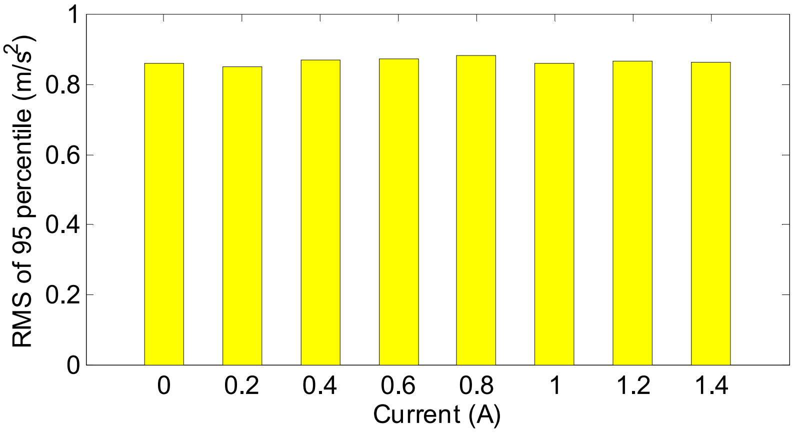

Figure 3.43 95 percentile of RMS values of bogie lateral acceleration at speed of 350 km/h

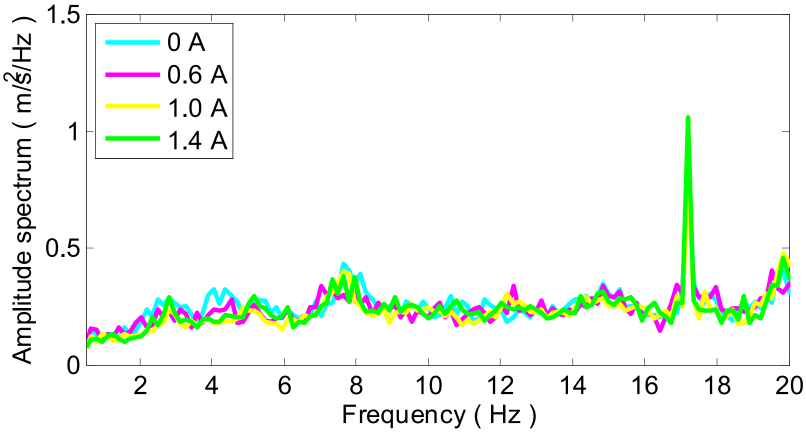

Figure 3.44 Amplitude spectrum of lateral acceleration of bogie at speed of 350 km/h

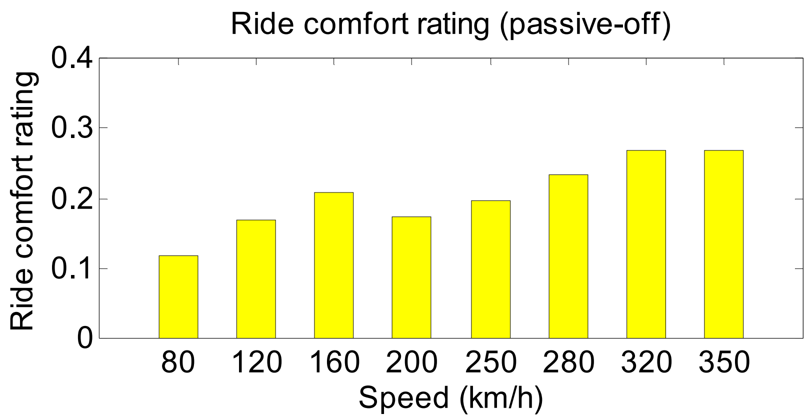

Figure 3.45 Ride comfort rating at damper passive-off state

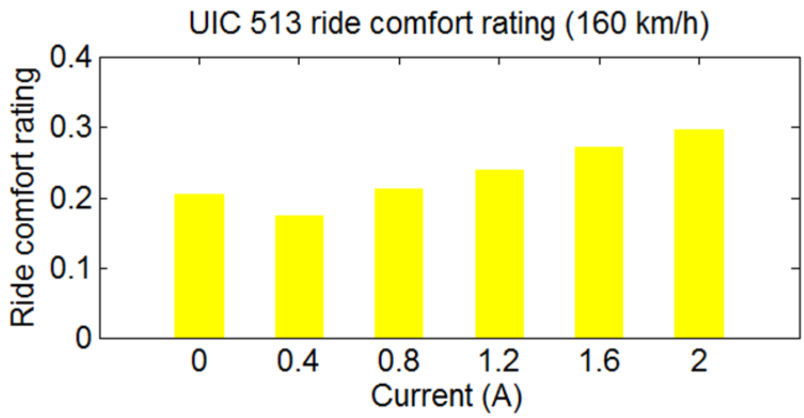

Figure 3.46 Ride comfort rating at speed of 160 km/h

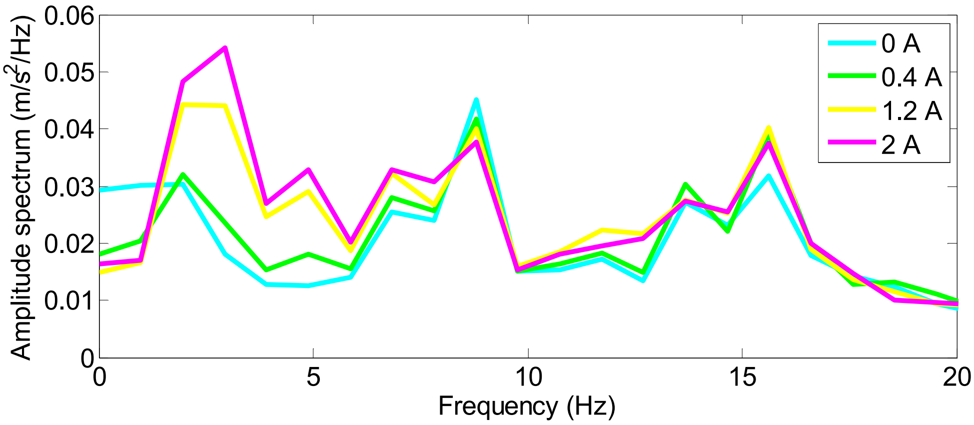

Figure 3.47 Amplitude spectrum of lateral acceleration of car body at speed of 160 km/h

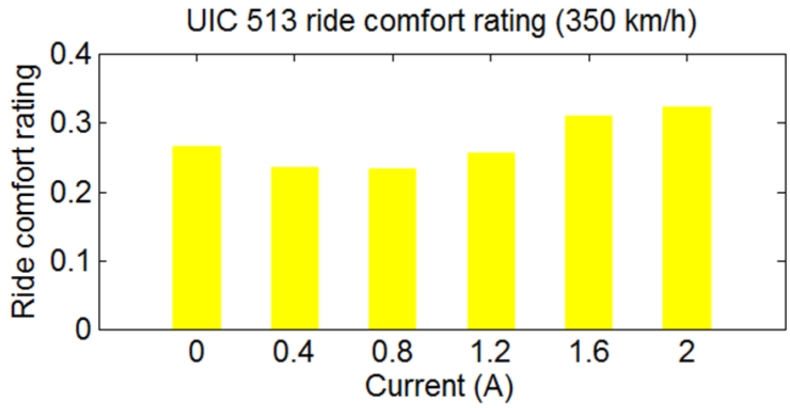

Figure 3.48 Ride comfort rating at speed of 350 km/h

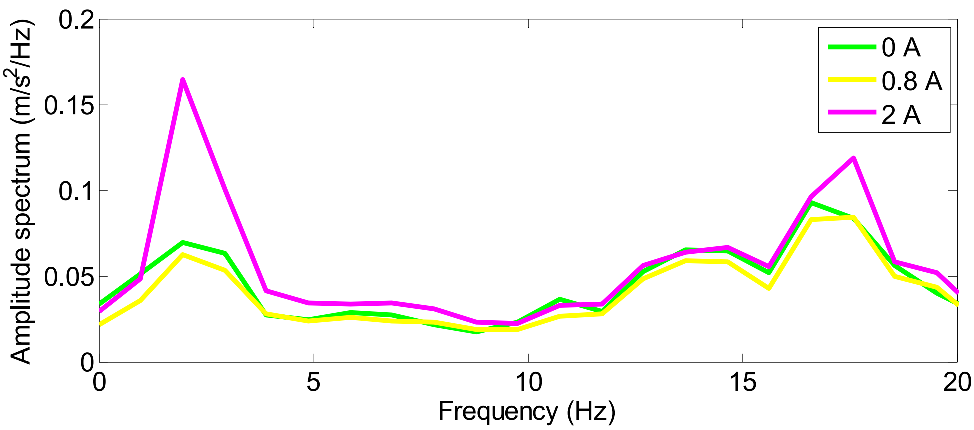

Figure 3.49 Amplitude spectrum of lateral acceleration of car body at speed of 160 km/h

CHAPTER 4

PARAMETRIC MODELING OF MR DAMPER

4.1 Introduction

The last chapter has illustrated the possibility of MR dampers for vibration attenuation for high-speed trains. However, prior to implementation, it is essential to establish an effective MR model that thoroughly characterizes the inherent strong nonlinear properties of the MR damper, which is beneficial both for the system dynamic prediction, and the control application afterwards. An effective model for MR damper usually involves the forward and the inverse characterization. The forward model is capable of calculating the damper force with the measured damper motions, i.e., the displacement and velocity across the damper. It is important for system integration and dynamic behavior prediction. On the other hand, an inverse model determines the control signal, i.e., current or voltage, to the MR damper to track the desired control force, which is usually necessary when constructing a damper controller.

The subject of MR damping modeling has been under study for decades, with the major review paper presented by Sahin et al (2010) and Wang and Liao (2011). It can be categorized into parametric and nonparametric models. The most popular parametric model for implementation of vibration control is the modified Bouc-Wen model (also called phenomenological model) proposed by Spencer et al. (1997). This model can accurately reproduce the highly nonlinear hysteresis of MR damper, especially the roll-off phenomenon in the low velocity region. However, the model contains fourteen parameters to be adapted. The associated identification is very computationally expensive, yet the uniqueness of the parameters cannot be guaranteed. Moreover, the model is governed by nonlinear differential equations, therefore, solving the equations to obtain the damper response usually requires integration-step rate up to 1 kHz to ensure the numerical stability. All these limit the use of the phenomenological model in real-time control. Alternatively, nonparametric models, such as neural networks (Weber et al. 2014; Chen et al. 2015, 2016) and fuzzy logic (Truong and Ahn 2011; Zong et al. 2012), have been of great interest recently for tuning and controlling the MR dampers. They build the underlying relationship between inputs and outputs. In this process, model parameters that have physical meanings or a priori physical knowledge of the system are even not necessary. Although nonparametric models are effective in system modeling, few models have been built by using experimental data, since the system noise will make the training process very difficult. Additionally, overfitting or generalization issue occurred in the model training has been rarely addressed, which might compromise the system stability or reliability. Their real-time application is still under development.

On the other hand, there have been few effective inverse models developed in terms of parametric models to date, because it is usually difficult to formulate a parametric model representing the relationship between the commanded current (or voltage) and the desired damper force due to the highly nonlinear properties of MR dampers. Therefore, most of the damper controllers are constructed based on the Bingham model (Tsang et al. 2006; Reader et al. 2009), with force feedback controller (Dyke et al. 1996;

Liao and Wang 2003, 2009). However, due to its insufficient characterization of pre-yield hysteretic behavior, the capability of accurate damper force tracking is rather difficult. What is worse, the system is rather more complicated since force transducer is involved. Instead, soft computing techniques (Metered et al. 2010; Bhowmik et al. 2013; Chen et al. 2015) are of great interest to establish the damper controller. However, the methodologies are identical to those that build the forward model, and the weakness is likewise similar. Thus, there are few attempts that apply experimental data in the data training process.

This chapter is concerned with the parametric modeling of the newly developed MR dampers for use in high-speed train secondary suspension. Firstly, the prototypes of the newly designed MR damper with the self-sensing functionality are introduced. The MR dampers are exclusively designed and manufactured for high-speed rail CRH3 EMU, with the passive-off damping, the suitable control force range, and feedback sensing etc. Subsequently, the dynamic tests on the MR dampers are performed to fully understand their hysteretic behaviors and controllability under a broad range of operating conditions. Then, the obtained dynamic behavior in terms of displacement, frequency and current input excitations is presented respectively. Focusing on the current- and the excitation condition-dependence acquired from the experimental data, an enhanced viscoelastic-plastic based model is proposed to directly characterize the MR damper dynamics. The describing model is established using a small portion of experimental data. And its prediction capability is subsequently validated by using the experimental data independent of those associated with model identification. Lastly, with the measured data obtained from the feedback sensing, i.e., the force transducer and the

LVDT, the damper controller is built to command the damper current according to a desirable control force.

4.2 Self-sensing MR damper

In Chapter 3, the rolling-vibration experiments are conducted on three types of MR suspensions (type-*A*, type-*B*, type-*C*). It can be observed that, the damping of type-*A* MR dampers was so stiff that they worked more like the spring components rather than the energy dissipative ones; type-*B* MR dampers failed to provide sufficient damper force at high running speeds where excessive vibrations occurred; while type-*C* suspension outperformed the others since the obvious pattern of car body vibration can be identified as tuning the damper current input, and optimal current input can be recognized. Therefore, type-*C* MR damper is considered suitable for controlling the vibrations of the car body of the CRH3 EMU. And the study on the vibration attenuation for the high-speed train car body is conducted in terms of the integration of type-*C* MR dampers.

The prototypes of type-*C* MR damper are shown in **Figure 4.1**. The cylinder is 79 mm in diameter. The damper is 587 mm long in its extended position, and 412 mm long in the compressed position, having a 175 mm stroke. The cylinder houses the piston, the magnetic circuit, an accumulator and the MR fluids. The accumulator is charged with 110 psi Nitrogen for restoring the MR fluids in operation. The power supply of the damper is 12 V, and the current input to the damper can be tuned between 0 A to 2 A.

To facilitate the damper controller, transducers are equipped with MR dampers for force and displacement feedback, as shown in **Figure 4.2**. Two strain gauges are mounted on the rod in parallel with the damper central axis, and build a half-bridge circuit to measure the damper force. The motion sensing element, a LVDT, is also equipped to measure the displacement across the damper. The transducer is assembled in parallel with damper axis. The body is clamped with the damper cylinder, while the extension rod is screwed to plate that is fixed to the damper rod. Thus, the extension rod moves as the damper piston motions, equivalently outputting the displacement of the damper. The MR dampers are pinned between the car body and the bogie of the train vehicle via secondary suspension in the lateral direction. **Figure 4.3** shows the installation of a self-sensing MR damper within the train vehicle secondary suspension. One end of the MR damper connects with the truck, and the other connects with the car body. In this way, the LVDT measures the relative displacement between the truck and the car body, namely the motion of the MR damper. And the force transducer measures the damper force to the vehicle.

4.3 Dynamic behaviors of type-*C* damper

The displacement-controlled experiment on the MR damper is conducted on a MTS test system (**Figure 4.4**). The damper is driven by the sinusoidal displacement with different amplitudes and at a series of frequencies. The current input to the damper is controlled by the AC/DC converter, seen in **Figure 4.5**. The excitation conditions are listed in **Table 4.1**. The dynamic behaviors of the MR damper is demonstrated in terms of the hysteresis loops of force-displacement and force-velocity under different driven conditions, i.e., current, amplitude and frequency.

4.3.1 Current dependence

Figures 4.6 and **4.7** show the force-displacement and force-velocity hysteresis loops at a frequency 3 Hz, with an amplitude 4 mm and for current levels 0 A, 0.4 A, 0.8 A, 1.0 A, 1.6 A and 2 A. It can be observed from the force-displacement loops that, the damper hysteresis loops progress along a counterclockwise path with increasing time. The damper force increases with current levels. The area enclosed by the force-displacement trajectory is larger with increasing current, indicating more energy dissipated by the MR damper. For 0 A current level, the damper force is mainly consisted of the viscous properties of the MR fluids and the fiction force between the damper rod and the seal element. As shown by the force-velocity trajectories, there are two distinct operating stages: pre-yield stage and post-yield stage. At small velocities, the MR damper operates at pre-yield stage and exhibits the visco-elastic behavior, as evident from the hysteretic behavior at this stage, while at post-yield region, the MR damper exhibits almost plastic behavior with the non-zero yield force. The increase rate of the peak damper force gradually slows down as the control current increases to the maximum, indicating the saturated behavior of the MR fluids.

4.3.2 Displacement amplitude and frequency dependence

Figures 4.8 and **4.9** display the force-displacement and force-velocity trajectories at a frequency 3 Hz, for a current level 0.8 A, with amplitudes 2 mm, 4 mm and 6 mm. **Figures 4.10** and **4.11** displays the force-displacement and force-velocity responses with an amplitude 4 mm, for a current level 0.8 A, at a series of frequencies 1 Hz, 3 Hz and 5 Hz. It can be observed that, the dynamic behavior of the MR damper is significantly dependent on the displacement amplitude and frequency excitations. As the frequency (or the displacement amplitude) increases, it can be observed from the force-displacement trajectories that, the peak damper force slightly increases, and the area captured by the hysteresis loop gets larger, indicating that the more energy is dissipated by the MR damper in one cycle; for the force-velocities trajectories, the pre-yield hysteretic slope decreases; the post-yield viscosity generally stays unchanged; and the yield force is independent on the frequencies and displacement amplitudes, and solely dependent on the current input.

Figures 4.12 and **4.13** provide two comparisons on the hysteresis responses of the MR damper subjected to the equal velocity amplitude excitations for the same current level, i.e., comparison 1 of scenario 1 at a frequency 2 Hz, with an amplitude 4 mm and for a current level 0.8 A, and scenario 2 at a frequency 4 Hz, with an amplitude 2 mm and for a current level 0.8 A; and comparison 2 of scenario 1 at a frequency 2 Hz, with an amplitude 6 mm and for a current level 0.6 A, and scenario 2 at a frequency 3 Hz, with an amplitude 4 mm and for a current level 0.6 A. It can be observed that, the force-velocity hysteresis loops of the two operating scenarios are almost the same, including the peak damper force, yield force, post-yield viscous coefficient and the pre-yield hysteresis. There is only slight difference in pre-yield hysteresis slope for comparison 1. It can be implied that, the damper response is dependent on the displacement amplitude and frequency, or equivalently the velocity amplitude dependence, instead of the velocity itself.

4.4 Parametric modeling

4.4.1 Viscoelastic-plastic based model

The hysteretic dynamics of the MR dampers are generally identified as three distinct rheological regions: pre-yield, yield and post-yield. In the pre-yield region, the MR fluids exhibit the strong hysteretic behavior which is typical of the viscoelastic materials; the yield region portrays the viscoelastic plastic dynamics; while the post-yield region is plastic with non-zero yield force, and the force to yield the damper increases as the current input is tuned louder. Based on these distinct dynamic behaviors, a variety of viscoelastic-plastic models (Kamath and Wereley 1997; Pang et al. 1998; Li et a. 2000; Snyder et al. 2001) have been proposed, which tended to provide the more straightforward and explicit expressions for MR damper characterization and prediction. Focusing on the pre-yield and post-yield dynamic behaviors, Li et al. (2013) proposed a simple mechanical model for the MR dampers using the steady measured data obtained from the MTS system. In their work, the viscoelastic behavior of the pre-yield region is represented by a Maxwell model composed of a viscous damper in series with a spring, while the visco-plastic behavior in the post-yield condition is represented by a Bingham plastic model composed of a viscous dashpot with a non-zero yield force. The two models fuse together, shown in **Figure 4.14**, to capture the distinct characteristics of MR damper.

The damper force generated by the model is given by

$$f_d = k(x - y) + f_0 = c\dot{y} + f_c tanh(\alpha\dot{y}) + f_0 \tag{4.1}$$

where k represents the stiffness in the pre-yield region; c is the viscous damping coefficient in the post-yield region; f_c is the yield force, which is dependent on the applied current; α is the scale factor that determines the hysteresis slope associated with pre-yield characteristics; the overall damper force is shifted by the offset f_0 that is determined by the initial displacement; x is the displacement across the damper; and y is the internal variable. It is worth noting that, the model employs the hyperbolic tangent function tanh(·) to describe the transition from pre-yield to post-yield region, whereas others e.g. the viscoelastic-plastic model by Pang et al. (1998) used three shape functions to capture the transition from viscoelastic to plastic.

The captured model is simple in mathematical expression. It is determined by only four parameters. Each parameter represents the specific dynamic characteristics in the associated condition. Generally, their values can be approximately estimated by steady experimental data. However, on the other hand, the simple expression also delivers a major shortcoming that the model usually works well when the operating condition (i.e., frequency or displacement amplitude) of the validation data is closed to that of training data, or equivalently the model is generally less adaptable in a wide range of operating conditions.

4.4.2 Current-frequency-amplitude-dependent viscoelastic-plastic model

4.4.2.1 Parameter analysis

The viscoelastic-plastic model by Li et al. (2013) is capable of capturing the unique hysteretic dynamics of the MR damper, including the pre-yield viscoelasticity (represented by hysteresis width and inclination), yield and post-yield viscosity. Additionally, it has only five parameters to be adapted, and the expression is quite straightforward for MR damper characterization. All these are beneficial for control applications. However, it is usually inadequate to work with a wide range of damper operating conditions. It is mainly because the model only takes into account the effect of the current inputs on the hysteretic behavior, as noted by the current-dependent model parameters in the representation equations (Li et al. 2013), while ignores the effect of the excitation displacement amplitude and frequency, or equivalently the velocity amplitude, which is readily revealed by **Figures 4.8** and **4.13**. Therefore, the dependence of the model parameters on the current input, displacement amplitude, and frequency to the MR damper is closely examined in the following, to develop an enhanced viscoelastic-plastic model that is more applicable to a broad variety of damper operations, while maintains the representation in a straightforward manner.

In parameter analysis, a group of experimental data with the increasing velocity amplitudes is involved, which are data from excitation conditions of frequency and stroke: 1 Hz and 2 mm, 2 Hz and 2 mm, 3 Hz and 2 mm, 4 Hz and 2 mm, 5 Hz and 2 mm, 3 Hz and 4 mm, 4 Hz and 4 mm, 3 Hz and 6 mm, 5 Hz and 4 mm, corresponding to increasing velocity amplitudes v_m: 12.57 mm/s, 25.13 mm/s, 37.70 mm/s, 50.27 mm/s, 62.83 mm/s, 75.40 mm/s, 100.53 mm/s, 113.10 mm/s, and 125.66 mm/s. It should be noted that, the data used in this process is the steady measured data obtained from the displacement-driven experiments. The model parameters in Equation (4.1) are calculated for each excitation condition. Their underlying relation with the varying control current and excitation condition is then minutely analyzed. The parameter estimation is done using MATLAB Simulink Optimization Toolbox.

(1) Yield force f_c

The experimental data in **Figure 4.15** suggests a strong dependence of yield force f_c on the applied current input I. The yield force begins with a non-zero value, and then generally increases in a linear relation with the increasing control current from 0 A to 2 A. Additionally, the obtained variation trend is all identical for different excitation conditions, v_m. Therefore, it can be concluded that, the yield force variation is not relevant to excitation conditions. It is reasonable, since the yield force is the unique feature of the MR fluids, which is determined by the rheological state of the fluids, and controlled solely by the surrounding magnetic field, or equivalently the current input. Consequently, the yield force can be expressed in a function of the control current by

$$f_c = d_1 i + d_0 \tag{4.2}$$

where d_1 and d_0 are the positive constants, delivering the linear rise of the yield force.

(2) Pre-yield hysteresis slope α

The hysteresis slope α refers to the low-velocity inclination of the force-velocity trajectory. **Figures 4.16** and **4.17** illustrates the variation in the hysteresis slope with the current input i and the excitation condition v_m, respectively. The result depicted in **Figure 4.16** shows that, the hysteresis slope generally rises when the control current is imposed, then followed by a slight variation to a steady value, which corresponds to the trend observed from the detailed experimental data in **Figure 4.7**. Generally, the current-induced variations are small, and can be assumed as a constant. The estimated data depicted in **Figure 4.17** suggests a rapid decaying variation for the hysteresis slope α in relation with v_m. Considering the influence of i and v_m together, the pre-yield hysteresis slope can be given by:

$$\alpha = \frac{\alpha_0}{1 + \alpha_1 v_m} \tag{4.3}$$

where α_0 and α_1 are positive constants used to adjust the decreasing curve of α; v_m denotes the maximum velocity. The experimental data observed from **Figures 4.8-4.13** clearly illustrate the dependence of damper hysteresis on the frequency and displacement amplitude. Herein, these two excitation conditions are expressed by the maximum velocity. It should be noted that, the maximum velocity cannot be measured directly. For harmonic motion, the maximum velocity is equivalently the velocity amplitude, which can be expressed by $v_m = a_m \cdot 2\pi \cdot f$, ($a_m$ = displacement amplitude). In random oscillation case, the magnitude of v_m can be obtained from the instantaneous position, x, (Wang et al. 2003), which is given by

$$v_m = \sqrt{\dot{x}^2 - \ddot{x} \cdot x} \tag{4.4}$$

where x, $\dot{x}$, and $\ddot{x}$ are the instantaneous displacement, velocity, and acceleration across the MR damper, respectively. It should be noted that, the velocity across the damper is obtained by differentiating from the measured displacement by 5$^{\text{th}}$-order Runge-Kutta method.

(3) Post-yield viscous damping c

Figure 4.18Figures 4.18 and **4.19** portray the current- and excitation condition-induced variations in post-yield viscous damping. It can be observed from **Figure 4.18** that, the post-yield viscous damping c gradually rises with increasing current input i, and then reaches a steady value. The nonlinear incremental behavior with increasing current also suggests a quadratic function of control current. The trend is identical for different excitation conditions v_m. It is worth noting that, most of the curves begin approximately at the same point, indicating that the damping coefficient at the beginning point (at the damper passive-off state) is almost identical. Focusing on the excitation condition-induced variations (**Figure 4.19**), a general rapid decaying trend is suggested for non-zero current levels. For current level of 0 A, i.e., passive-off damper, the value is approximately unchanged with the rising velocity amplitude, which accords with the evidence observed earlier in **Figure 4.18**. Consequently, the evolution of c in relationship with i and v_m is a combination of the current-induced and the velocity amplitude-induced variations, given by

$$c = c_i \cdot c_v \tag{4.5}$$

The current-induced component c_i is a quadratic function of current i, given by

$$c_i = c_{i2} i^2 + c_{i1} i + c_0 \tag{4.6}$$

where c_{i2}, c_{i1}, c_0 are constants. Particularly, c_0 is the viscous damping coefficient at the damper passive-off state, i.e., $i = 0$. In other words, it is the slope of the centerline of the post-yield hysteresis loop. It should be noted that, the data that outputs the force-velocity hysteresis loop is obtained at the steady state. Therefore, the viscous damping can be calculated directly from experimental force-velocity hysteresis loop. As shown in **Figure 4.20**, points X_{u1} and X_{u2} locates at the upper branch of the force-velocity hysteresis loop near the peak velocity, which is expressed by coordinate $(\dot{x}_{u1}, f_{u1})$ and $(\dot{x}_{u2}, f_{u2})$ respectively; while points X_{l1} and X_{l2} locates at the lower branch of the force-velocity hysteresis loop near the peak velocity, which is expressed by coordinate ($\dot{x}_{l1}, f_{l1}$) and ($\dot{x}_{l2}, f_{l2}$) respectively; and thus the viscous damping coefficient is the average of the slope of the upper and lower branches of post-yield hysteresis loop, which is given by

$$c_0 = \frac{f_{u2} - f_{u1} + f_{l2} - f_{l1}}{\dot{x}_{u2} - \dot{x}_{u1} + \dot{x}_{l2} - \dot{x}_{l1}} \tag{4.7}$$

where $\dot{x}_2$ and $\dot{x}_1$ are the velocities at two different point near the peak velocity; f_2 and f_1 are the measured damper force obtained for the specified velocity $\dot{x}_2$ and $\dot{x}_1$, respectively; subscript u and l denotes the upper and lower branch of the force-velocity hysteresis loop, respectively.

The excitation condition-induced component c_v can be expressed as

$$c_v = \frac{c_{v0}}{1 + c_{v1} v_m} \tag{4.8}$$

where c_{v0} and c_{v1} are positive constants; v_m is the maximum velocity.

Therefore, the current-velocity amplitude-dependent post-yield viscous damping is devolved into

$$c = (c_{i2} i^2 + c_{i1} i) \cdot \frac{c_{v0}}{1 + c_{v1} v_m} + c_0 \tag{4.9}$$

(4) Pre-yield stiffness k

The pre-yield stiffness k is the stiffness at the pre-yield state derived from the force-displacement loop. In view of that the data that outputs the force-velocity hysteresis loop is obtained at the steady state, the pre-yield stiffness can be calculated directly from experimental force-displacement trajectory. Given two points X_1 and X_2 at the pre-yield region of the force-displacement trajectory (seen in **Figure 4.21**), which is denoted by coordinates ($x1$, $f1$) and ($x2$, $f2$) respectively, pre-yield stiffness can be directly estimated by experimental data

$$k = \frac{f_2 - f_1}{x_2 - x_1} \tag{4.10}$$

where x_1 and x_2 are the displacement at two different points in the pre-yield branch of force-displacement trajectory; f_1 and f_2 are the measured damper force for the specified displacement x_1 and x_2, respectively. It can be observed from the current-, frequency- and amplitude-dependence force-displacement hysteresis loops (**Figures 4.6**, **4.8** and **4.10**), the slope at the pre-yield regions is almost identical. It can be explained by the fact that, the pre-yield stiffness primarily comes from the Nitrogen gas-charged accumulator in the MR damper, which is not relevant to the control current and excitation condition. Therefore, pre-yield stiffness k can be set as a constant.

4.4.2.2 Model synthesis

The last section minutely examines the dependence of the model parameters on the excitation conditions. By integrating these enhanced parameters into describing Equation (4.11), the overall current-frequency-amplitude dependent model can be formulated as:

$$f_d = k(x - y) + f_0 = c\dot{y} + f_c tanh(\alpha\dot{y}) + f_0 \tag{4.11}$$

where

$$c = (c_{i2}i^2 + c_{i1}i) \cdot \frac{c_{v0}}{1 + c_{v1}v_m} + c_0 \tag{4.12}$$

$$f_c = d_1 i + d_0 \tag{4.13}$$

$$\alpha = \frac{\alpha_0}{1 + \alpha_1 v_m} \tag{4.14}$$

$$v_m = \sqrt{\dot{x}^2 - \ddot{x} \cdot x} \tag{4.15}$$

Amongst these, x, i.e., the displacement across the MR damper, and f_d, i.e., the damper force, are measurable, while y is evolutionary variable, which can not be measured in the dynamic tests. Therefore, there are a total of 10 parameters in the characterization model to be identified, which are f_0, k, c_{i1}, c_{i2}, c_{v0}, c_{v1}, c_0, d_1, d_0, α_0, and α_1. It should be noted that, k is associated with the pre-yield stiffness, which can be calculated by Equation (4.10); c_0 represents the viscous damping coefficient at damper passive-off state (I = 0 A), which can be directly calculated from force-velocity hysteresis loop, as seen in Equation (4.7); d_0 refers to yield force at damper passive-off state, which can be estimated from force-velocity hysteresis loop; f_0 is the offset of the damper force, which is determined by the installation of the MR damper, and can be measured at the very beginning. Therefore, there are 7 parameters left in Equation (4.11) to be adopted, i.e., c_{i1}, c_{i2}, c_{v0}, c_{v1}, d_1, α_0, and α_1. The corresponding parameter identification is done by using a portion of steady experimental data in MATLAB Simulink Optimization Toolbox.

4.4.2.3 Formulation of inverse dynamics

This section concerns the construction of the MR damper controller which commands the current input to the MR damper with regards to the desired damper force. Equation (4.11) presents the forward relationship between the current input and the damper force for the type-C MR damper. Focusing on the current-dependent components and the current-independent components for damper force f_d, Equation (4.11) can be re-expressed as follow:

$$f_d = u_2 i^2 + u_1 i + u_0 \tag{4.16}$$

where u_2, u_1 and u_0 are constants, formulated as:

$$u_2 = \frac{c_{i2} \cdot c_{v0}}{1 + c_{v1} \cdot v_m} \cdot \dot{y} \tag{4.17}$$

$$u_1 = c_{i1} + d_1 \tanh(\alpha \dot{y}) \tag{4.18}$$

$$u_0 = d_0 \tanh(\alpha \dot{y}) + c_0 \dot{y} + f_0 \tag{4.19}$$

$$y = x - \frac{f_d}{k} \tag{4.20}$$

In view of that the real-time damper force and damper displacement (or velocity) is measurable from feedback sensing, the current input can be obtained by solving Equation (4.16). However, it should be noted that, the damper response is path-dependent, especially in roll-off region (Spencer et al. 1997). Therefore, the command current should be determined by tracking whether the damper force is within the upper branch or the lower branch in the force-velocity loop.

4.5 Validation

A group of experimental data acquired under different currents and excitation conditions is selected to identify the model parameters of the MR damper, which are data of 1 Hz and 2 mm, 3 Hz and 4 mm, and 5 Hz and 4 mm. The parameter estimation is done by using MATLAB Simulink Optimization Toolbox. The parameters are summarized in **Table 4.2**.

The developed current-excitation-dependent model is applied to predict the damper force under a wide range of excitation conditions and control currents. Due to a large amount of experimental data, the measured and simulated damper force is compared for some selected case. The selection is made such that the predicted data is independent of the one associated with the parameter identification. **Figures 4.20** and **4.21** compare the measured data and experimental data in terms of force-displacement and force-velocity hysteresis loops (5 cycles) under the excitation conditions: frequency = 2 Hz, amplitude = 6 mm, and frequency = 4 Hz, amplitude = 2 mm, respectively. The comparisons show a good agreement between the prediction and the measurement.

4.6 Summary

The forward and inverse parametric modeling for type-*C* MR damper equipped with damper force and displacement feedback is presented in this chapter. The model focuses on the representation of the two rheological regions of the MR fluid, i.e., pre-yield and post-yield regions. The pre-yield hysteresis is expressed by a Maxwell model composed of a viscous damper in series with a spring, while the visco-plastic dynamics in the post-yield phrase is formulated by a Bingham plastic model composed of a viscous dashpot with a non-zero yield force. By minutely examining the dependence of the pre-yield stiffness, pre-yield stiffness, pre-yield hysteresis slope, yield force and post-yield viscous damping on the operating conditions which are current input, excitation frequency and amplitude respectively, it can be observed that, the captured parameters are generally relevant not only to the current input, but to the velocity across the damper. Thus, a current-frequency-amplitude dependent viscoelastic plastic model is established to fully capture the hysteretic behavior of the MR damper. Taking advantage of the damper force and displacement feedback sensing, a path-dependent inverse model is obtained directly by solving the parametric forward model. Two independent groups of steady experimental data are selected for model identification and corresponding validation of MR damper. It is validated that, the developed model can accurately predict the damper dynamics in a wide range of operating conditions.

Figure 4.1 Four prototypes of new MR damper exclusive for CRH3 EMU

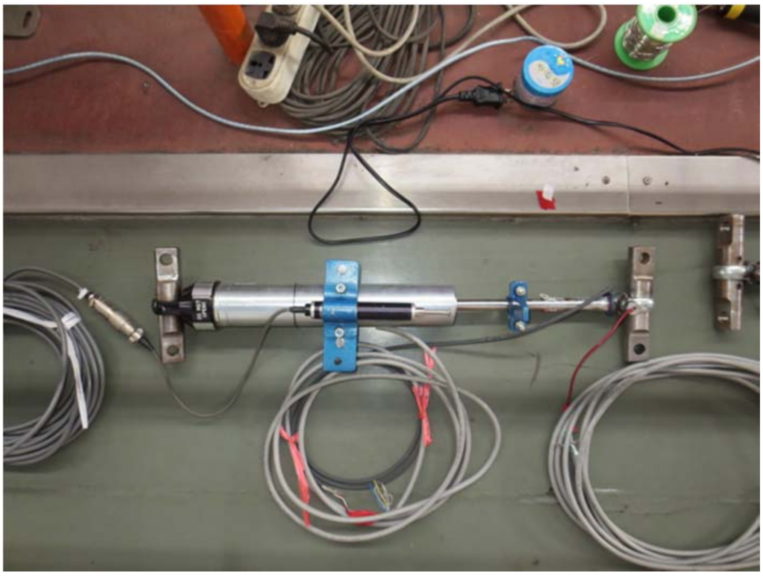

Figure 4.2 Self-sensing MR dampers

Figure 4.3 Installation of MR damper

Figure 4.4 Dynamic tests on MR damper

Figure 4.5 AC/DC converter

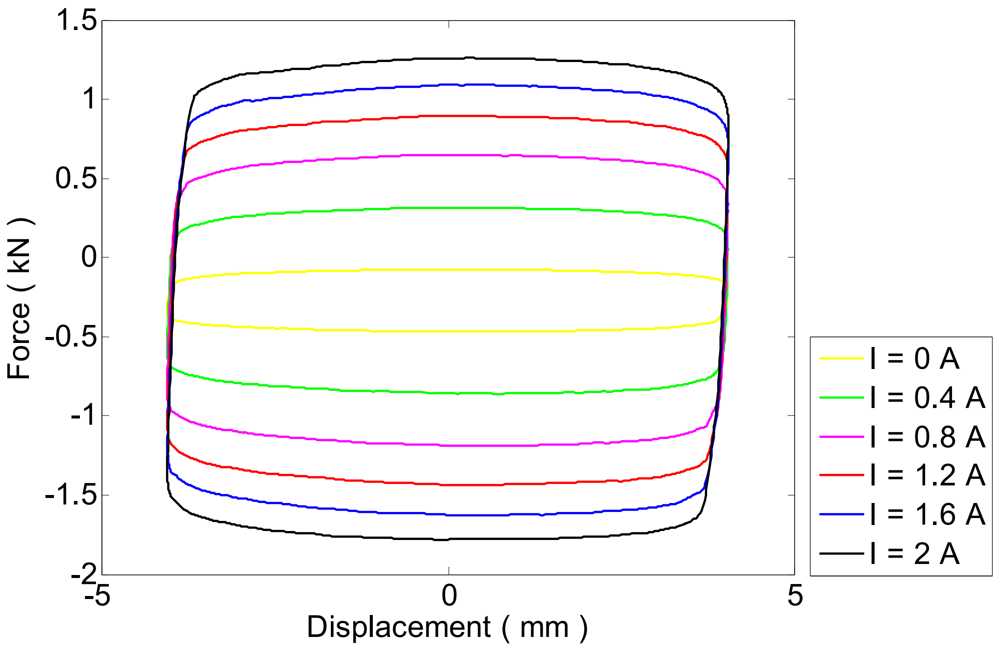

Figure 4.6 Force-displacement trajectories at a frequency 3 Hz and with an amplitude 4 mm

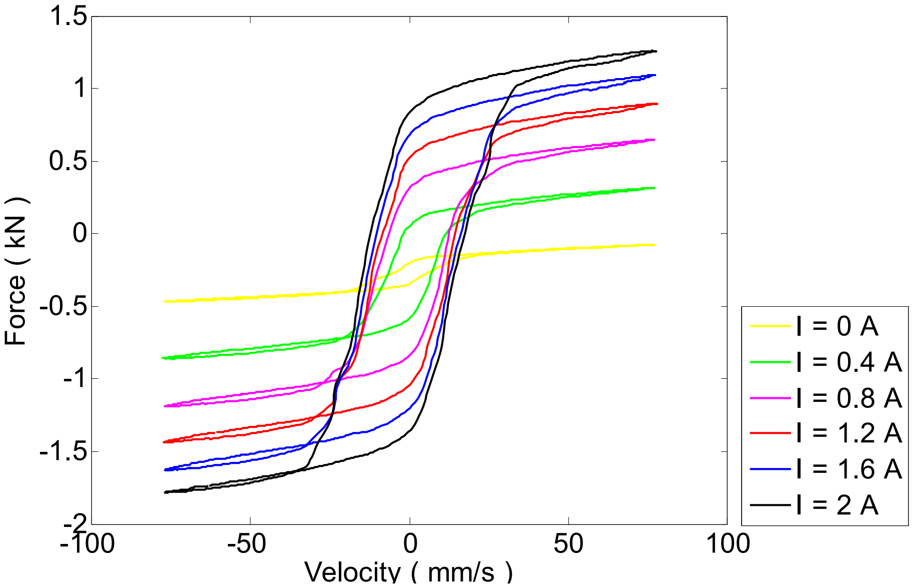

Figure 4.7 Force-velocity trajectories at a frequency 3 Hz and with an amplitude 4 mm

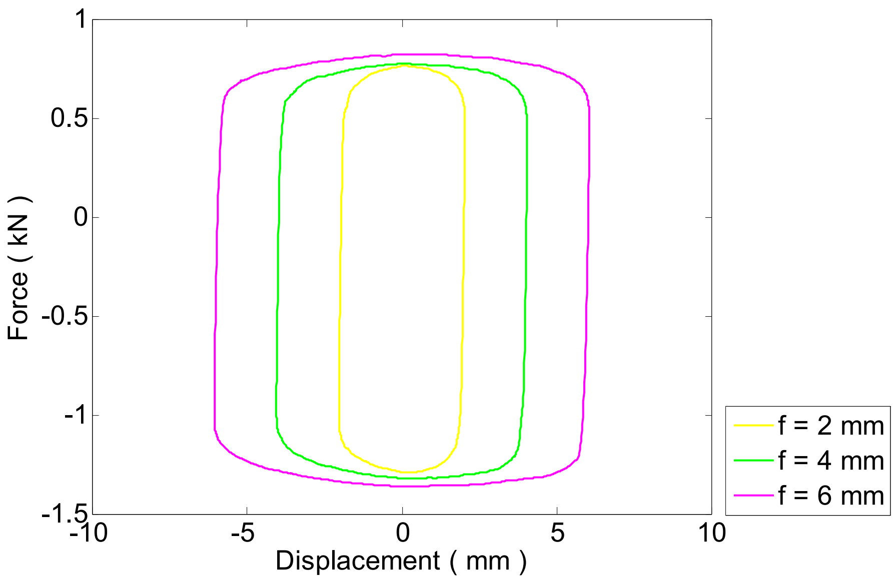

Figure 4.8 Force-displacement trajectories at a frequency 3 Hz and for a current level 1 A

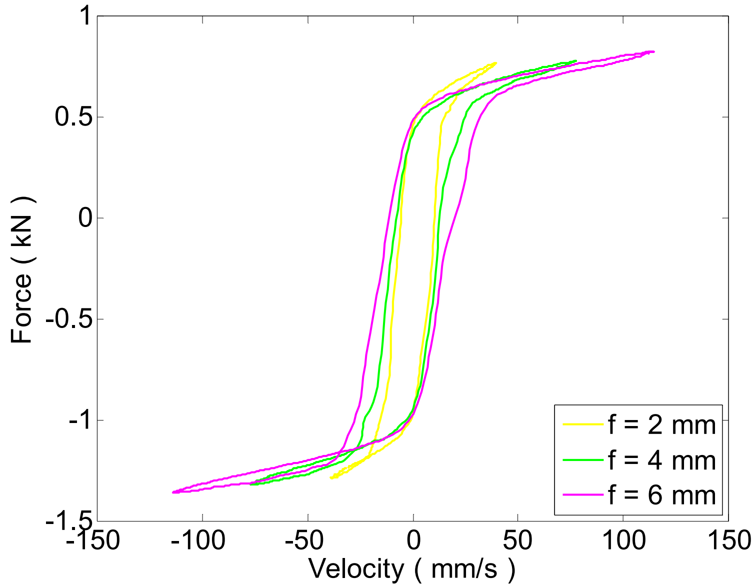

Figure 4.9 Force-velocity trajectories at a frequency 3 Hz and for a current level 1 A

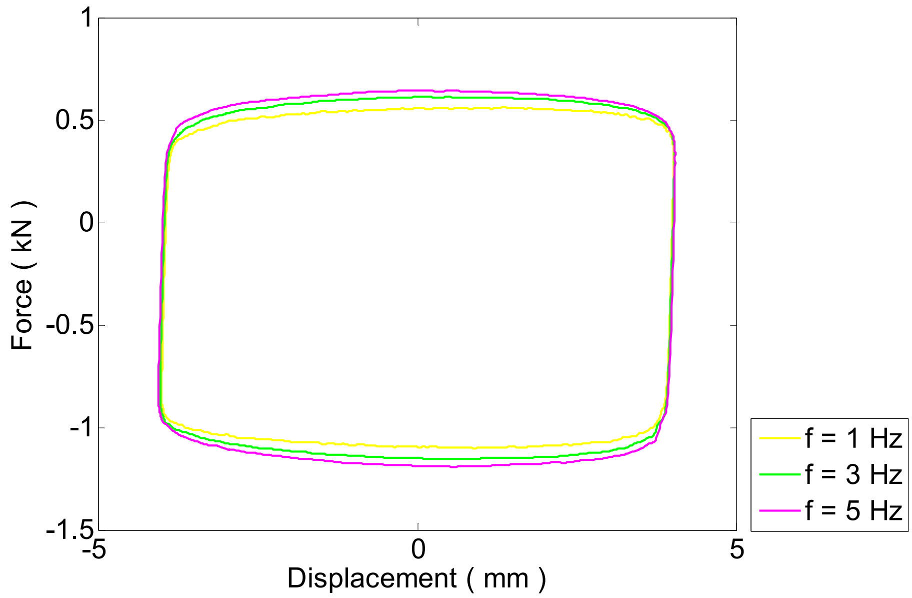

Figure 4.10 Force-displacement trajectories with an amplitude 4 mm and for a current level 0.8 A

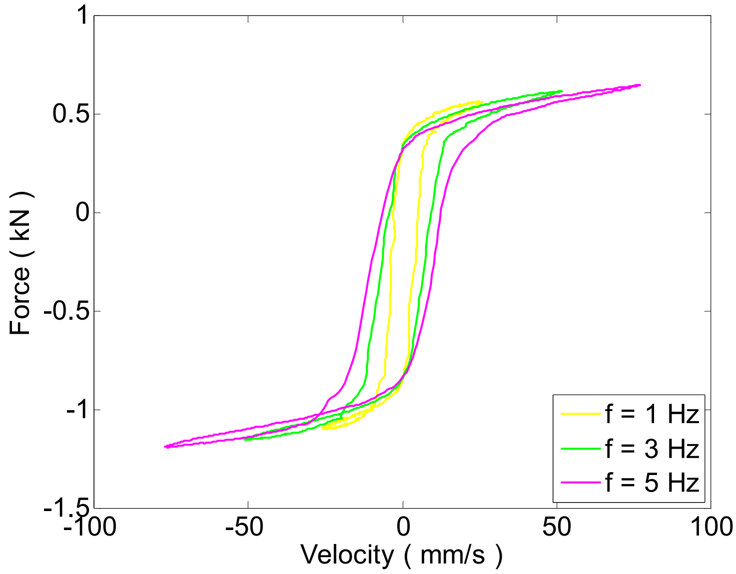

Figure 4.11 Force-velocity trajectories with an amplitude 4 mm and for a current level 0.8 A

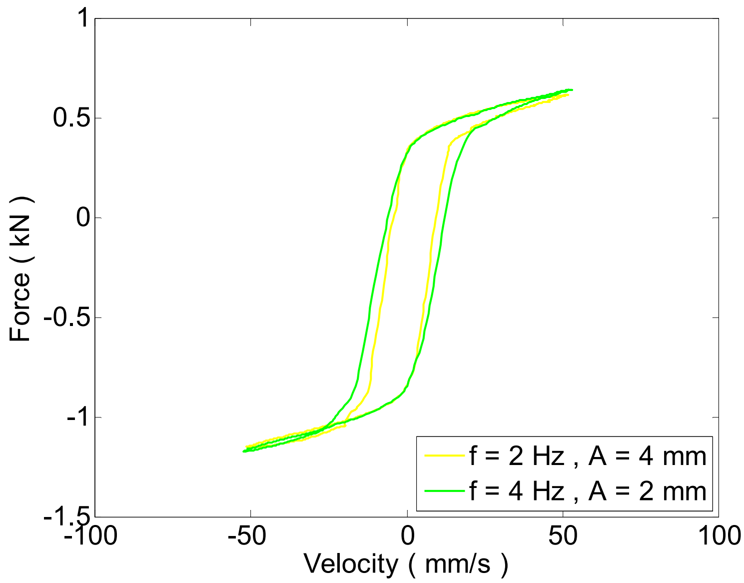

Figure 4.12 Comparison 1 of hysteresis responses for two working scenarios with same velocity amplitude excitation (Scenario 1: f = 2 Hz, A = 4 mm, I = 0.8 A; Scenario 2: f = 4 Hz, A = 2 mm, I = 0.8 A)

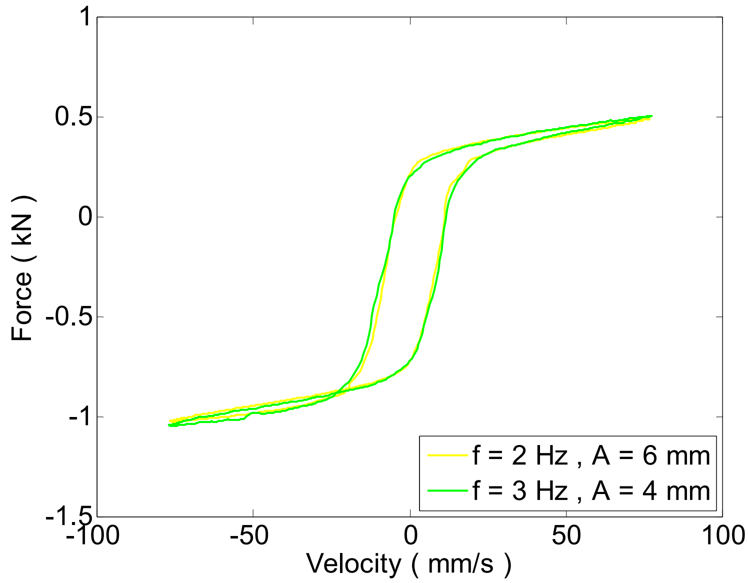

Figure 4.13 Comparison 2 of hysteresis responses for two working scenarios with same velocity amplitude excitation (Scenario 1: f = 2 Hz, A = 6 mm, I = 0.6 A; Scenario 2: f = 3 Hz, A = 4 mm, I = 0.6 A)

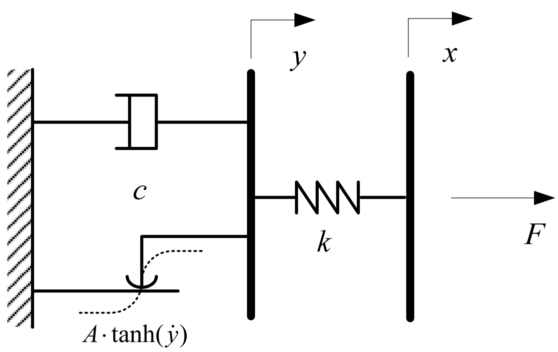

Figure 4.14 Schematic of viscoelastic-plastic model by Li et al. (2013)

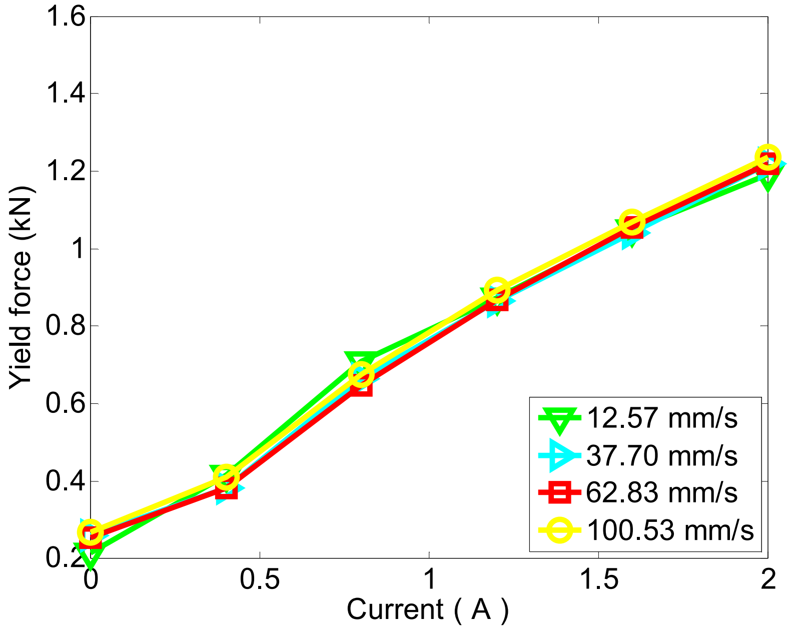

Figure 4.15 Variation in yield force with control currents

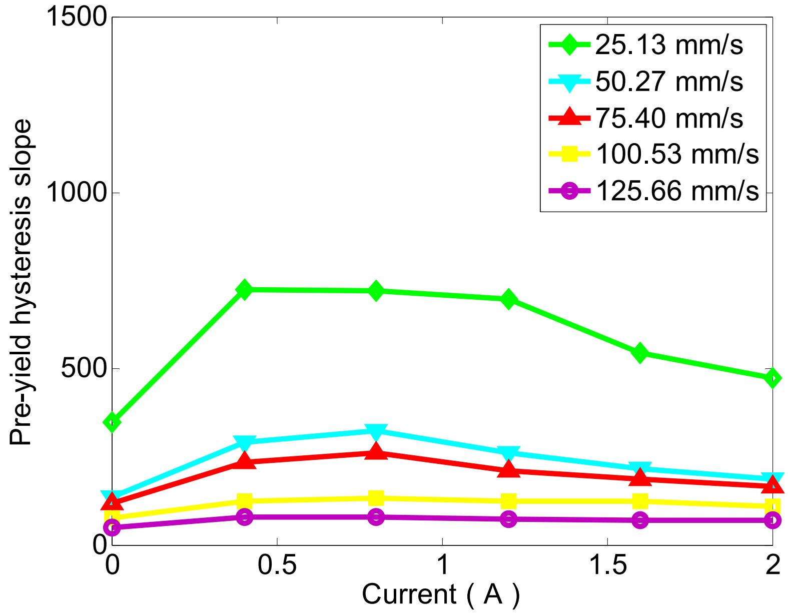

Figure 4.16 Variation in pre-yield hysteresis slope with control currents

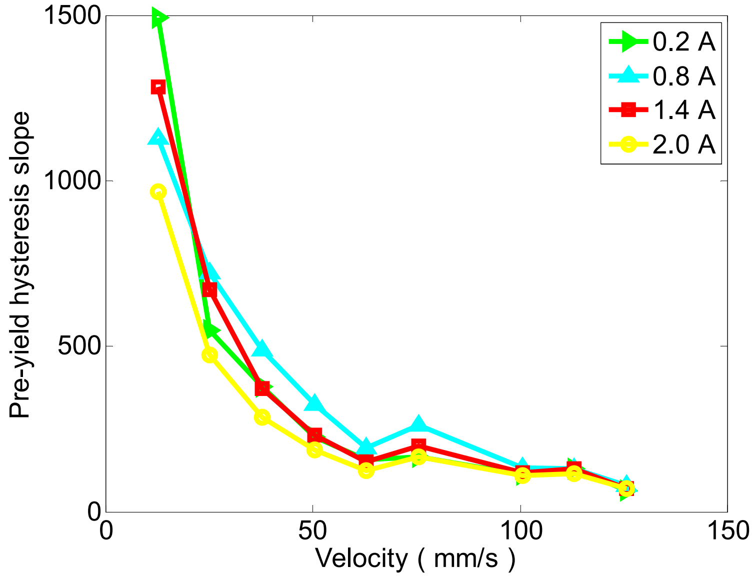

Figure 4.17 Variation in pre-yield hysteresis slope with excitation conditions

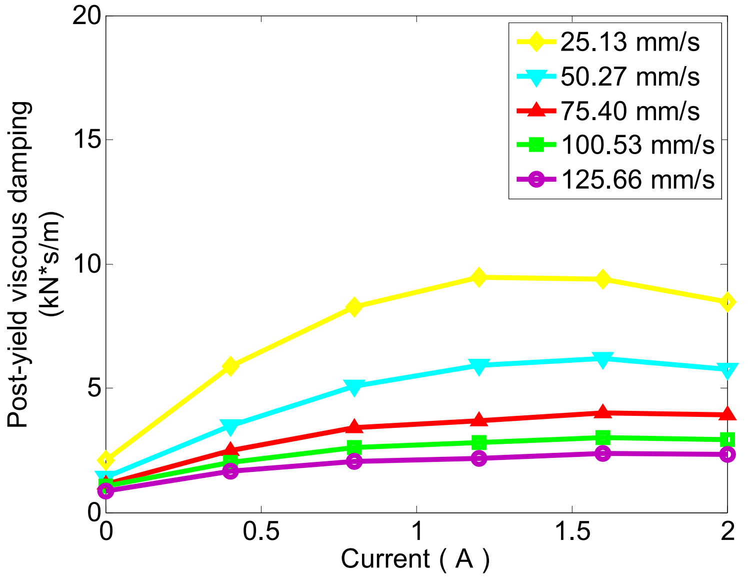

Figure 4.18 Variation in post-yield viscous damping with control currents

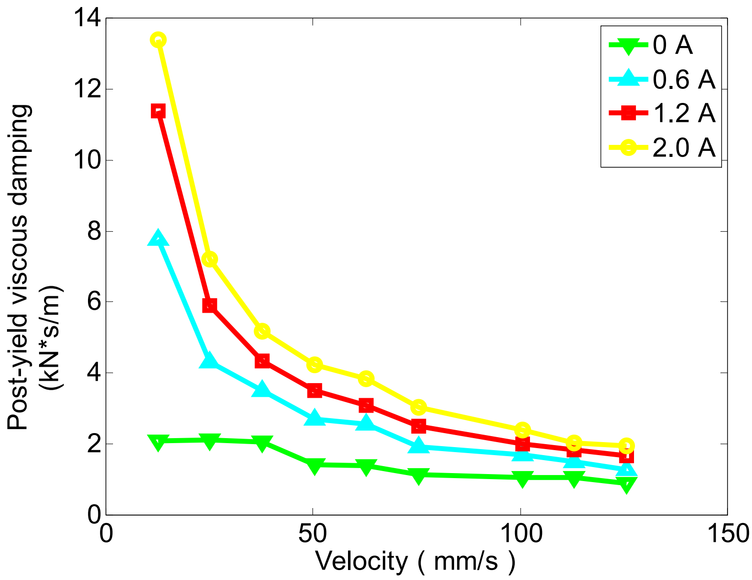

Figure 4.19 Variation in post-yield viscous damping with excitation conditions

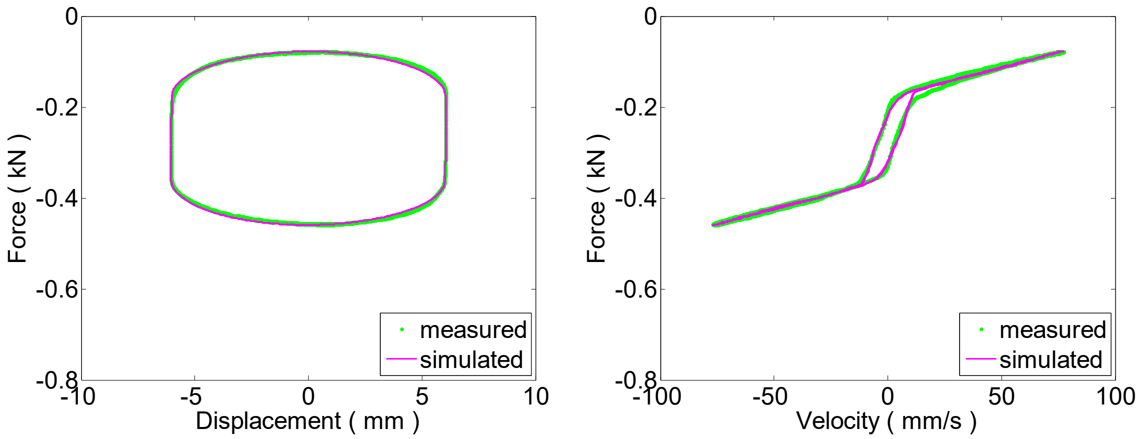

(a) $I = 0$ A

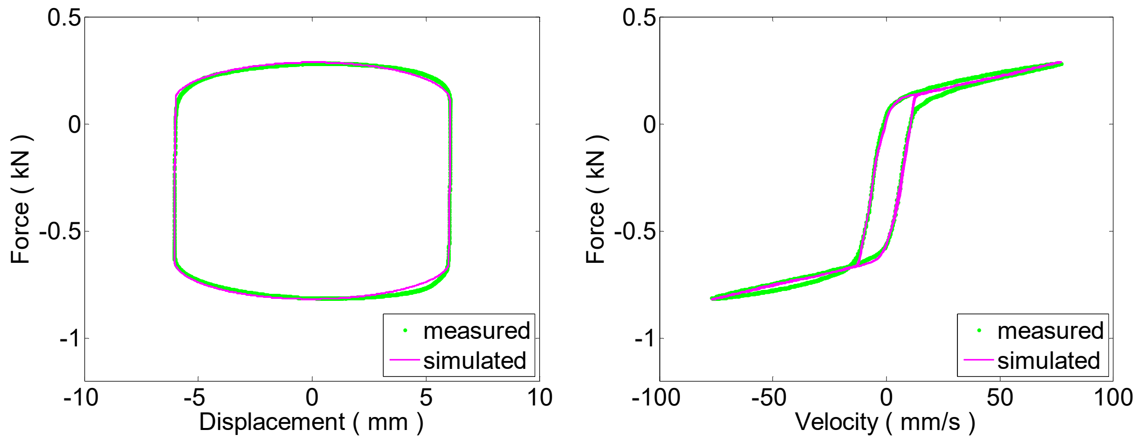

(b) $I = 0.4$ A

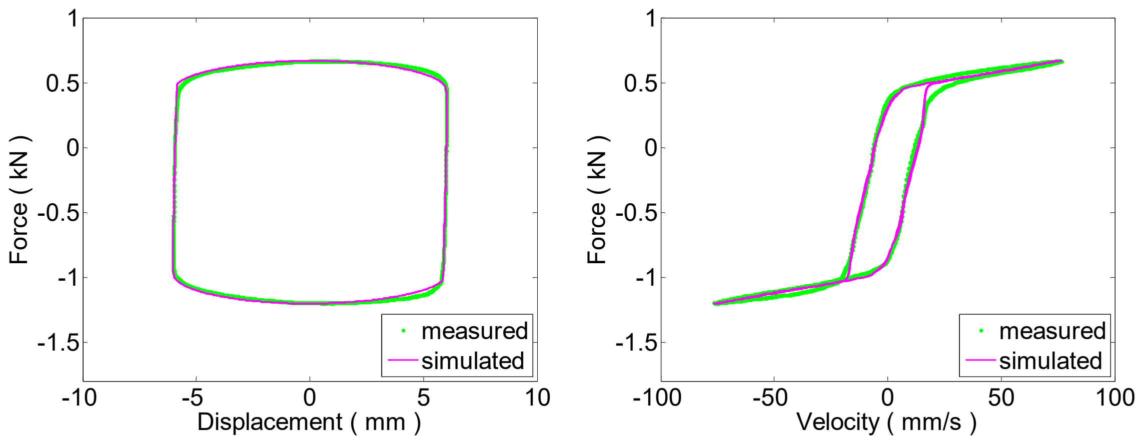

(c) $I = 0.8$ A

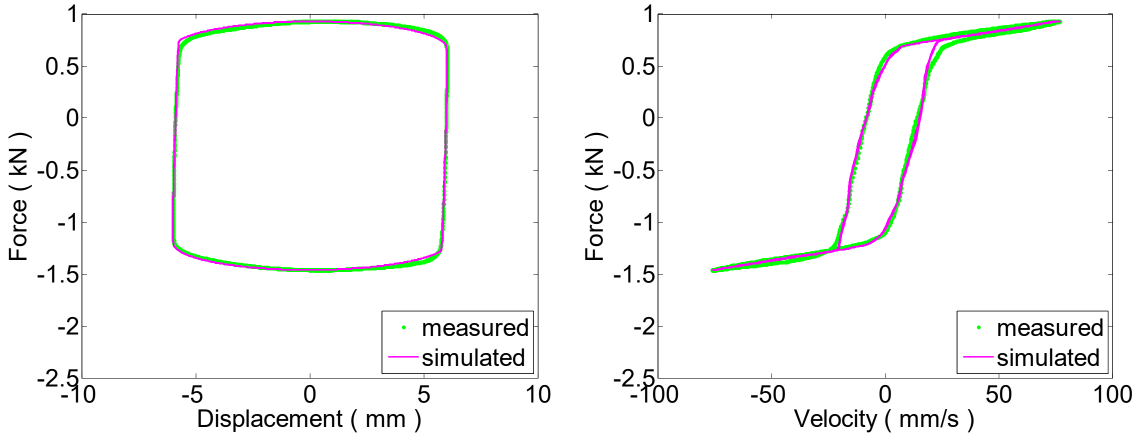

(d) I = 1.2 A

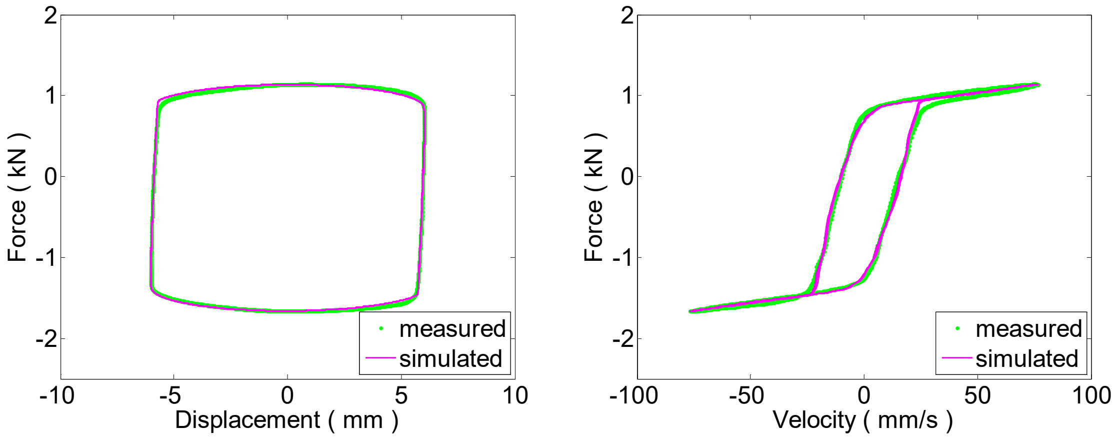

(e) I = 1.6 A

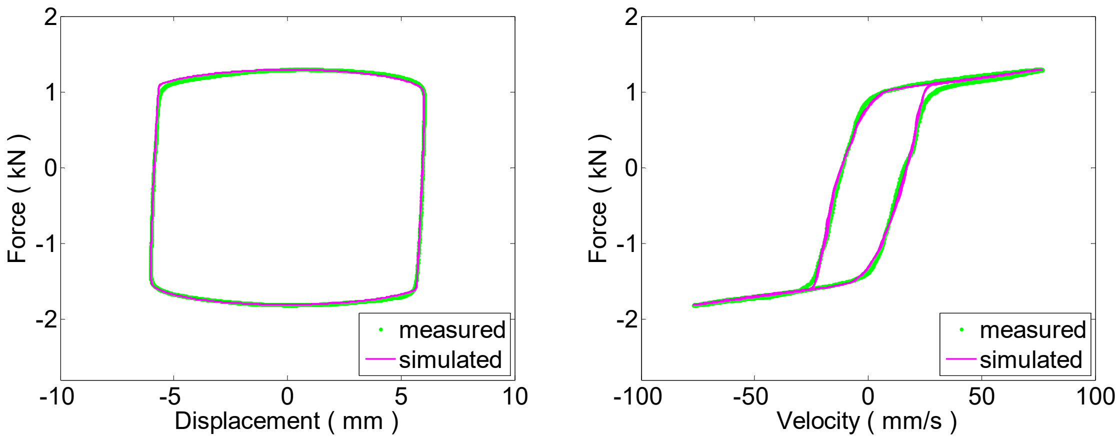

(f) I = 2 A

Figure 4.20 Comparison of measured and predicted force-displacement and force-velocity trajectories for excitation condition frequency = 2 Hz, amplitude = 6 mm

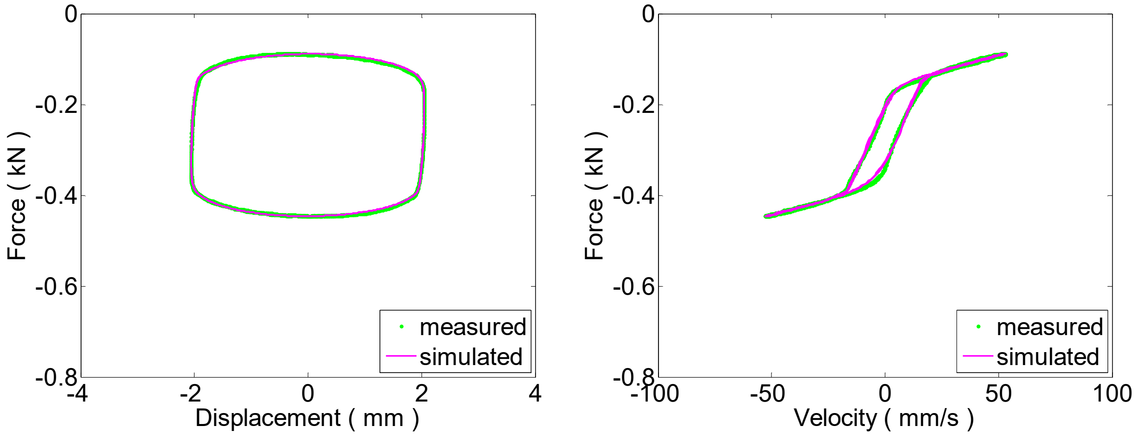

(a) $I = 0$ A

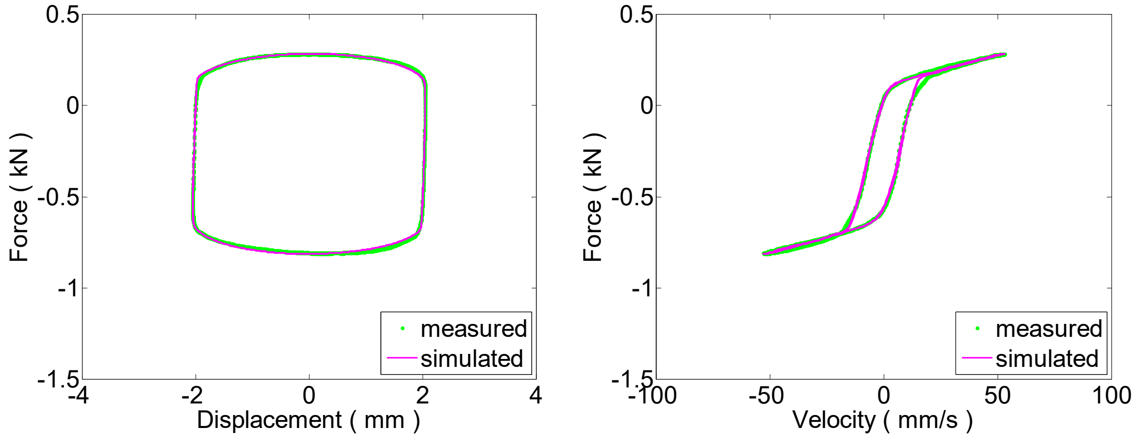

(b) $I = 0.4$ A

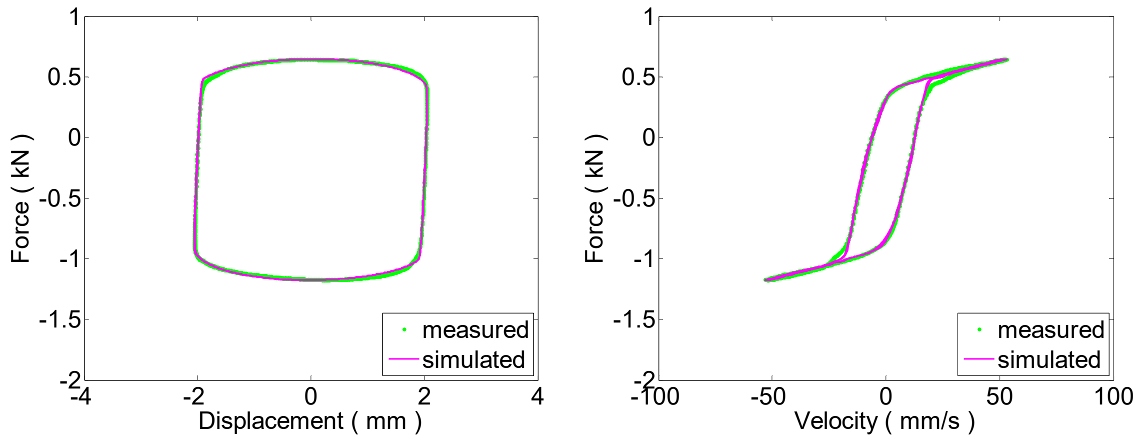

(c) $I = 0.8$ A

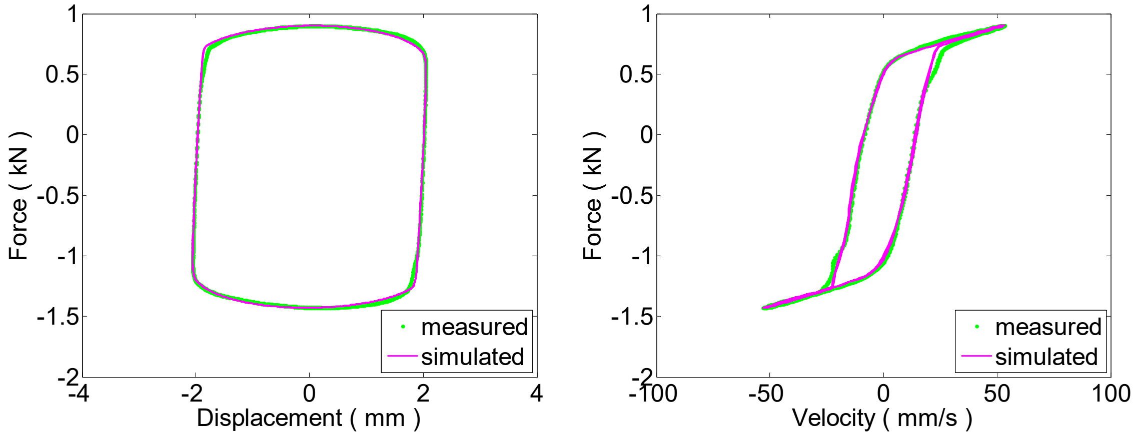

(d) $I = 1.2$ A

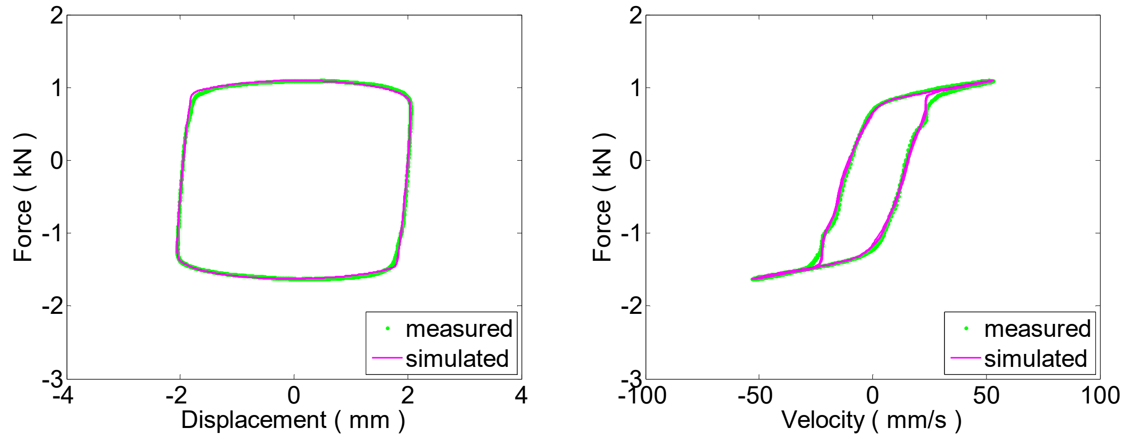

(e) $I = 1.6$ A

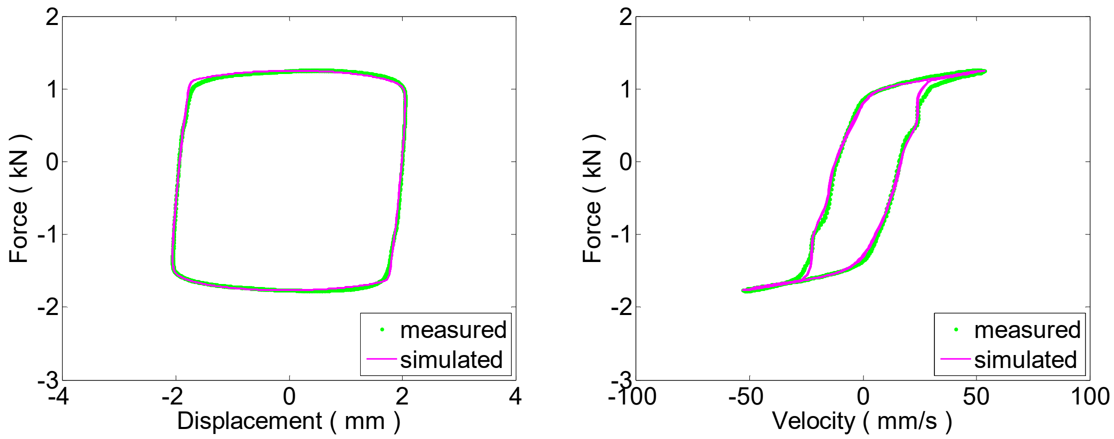

(f) $I = 2$ A

Figure 4.21 Comparison of measured and predicted force-displacement and force-velocity trajectories for excitation condition frequency = 4 Hz, amplitude = 2 mm

Table 4.1 Measured data for MR damper dynamic tests

Displacement (mm)	Frequency (Hz)	Control current (A)
(sin) 2	1, 2, 3, 4, 5	0, 0.2, 0.4, 0.6, 0.8, 1, 1.2, 1.4, 1.6, 1.8, 2
(sin) 4	1, 2, 3, 4, 5	0, 0.2, 0.4, 0.6, 0.8, 1, 1.2, 1.4, 1.6, 1.8, 2
(sin) 6	1, 2, 6	0, 0.2, 0.4, 0.6, 0.8, 1, 1.2, 1.4, 1.6, 1.8, 2
(sin) 8	1, 2	0, 0.2, 0.4, 0.6, 0.8, 1, 1.2, 1.4, 1.6, 1.8, 2
(sin) 10	1	0, 0.2, 0.4, 0.6, 0.8, 1, 1.2, 1.4, 1.6, 1.8, 2

Table 4.2 Identified model parameters of MR damper

Parameter	Value	Parameter	Value
k	1.260	d_0	221
c_0	1023	d_1	751.1
c_{i1}	1.279	α_0	0.940
c_{i2}	7.285	α_1	5.296
c_{v0}	0.977	f_0	-258.9
c_{v1}	0.4		

CHAPTER 5

VIBRATION MITIGATION FOR HIGH-SPEED TRAIN USING SEMI-ACTIVE NEGATIVE STIFFNESS EMULATED BY MR DAMPERS

5.1 Introduction

The railway vehicle running on a track is one of the most complicated dynamic systems in engineering. There are many degrees of freedom and nonlinear interaction between wheel and rail. Therefore, sophisticated design on rail suspension for vibration attenuation has been of great significance. Especially for high-speed train today whose running speed accelerates unprecedentedly, the vehicle dynamic responses induced by the track irregularities will be tremendously aggravated, leading to problems concerning passenger ride comfort, vehicle stability, and cost of track maintenance, etc. This difficult situation motivates the investigation of controllable suspensions, which is capable of diverse performance that is not possible with passive suspension.

In recent years, the dynamic performance of the controlled suspensions strongly relies on actuators and sensors. More recently, MR damper, emerging as a promising semi-active actuators, have attracted substantial research interests in railway industrial, as well as other fields such as civil engineering (Gordaninejad et al. 2002; Loh et al. 2007; Aly et al. 2010; Rodriguez et al. 2012), automobiles (Choi et al. 2000; Gopala

Rao and Narayanan 2008). Although MR damper is being implemented in many context, the accompanying control strategies are still of great interest. The state-of-the-art points out that, most of the controllers for railway vehicles are established according to skyhook damping (Choi et al. 2001a; Reader et al. 2009; Sun et al. 2013), LQG control (Wang and Liao 2009a, b; Zhao and Cao 2012) etc. On the other hand, it has been observed that, active control, such as skyhook control and LQG control, outputs damper forces with apparent negative stiffness characteristics. However, the effect of negative stiffness on structural vibration control has not been fully understood, since the outcome control force can be directly commanded, rather than the negative stiffness properties itself. Nevertheless, it still suggests the applications of control devices with negative stiffness. Iemura et al. (2005, 2008, 2009) proposed a pseudo-negative stiffness algorithm for seismic response control. The effectiveness was validated on cables, buildings and highway bridges. Hogberg (2011) introduced the equivalent negative stiffness to buildings vibration suppression. The results demonstrated a potential increase in damping efficiency with negative stiffness. Weber et al. (2011) presented an innovative tuned mass damper for cable control with positive/negative stiffness. Yang et al. (2014) proposed a novel magnetorheological elastomer isolator with negative changing stiffness for automobile suspension. Negative stiffness components have shown great potential for vibration reduction. However, there are few applications for high-speed train suspension.

Investigation presented in this chapter is concerned with the performance of the negative stiffness properties on railway vehicle vibration attenuation. The negative stiffness with viscous damping and friction damping is first introduced respectively.

The integrations with quarter car and 15-DOF train vehicle are demonstrated subsequently for evaluating their effectiveness.

5.2 Simulations on a Quarter Car Incorporated with Negative Stiffness

For ease of illustration, the following numerical analysis is conducted on a typical quarter car model integrated with a MR damper. The vehicle model, as seen in **Figure 5.1**, consists of a sprung mass, m_s, and an unsprung mass, m_u. The motion is described by vertical displacement of sprung mass and unsprung mass, i.e., x_s and x_u, respectively. The MR suspension comprises an air spring and an MR damper that replaces the passive hydraulic damper, accounting for attenuating the vibrations induced by the vertical track irregularities, x_t. The equations of motion can be expressed as:

$$m_s\ddot{x}_s + k_s(x_s - x_u) = f_{mr} \tag{5.1}$$

$$m_u\ddot{x}_u + k_p(x_u - x_t) - k_s(x_s - x_u) + c_p(\dot{x}_u - \dot{x}_t) = -f_{mr} \tag{5.2}$$

where x_s and x_u are the sprung mass and unsprung mass displacements, respectively; f_{mr} represents the damper force generated by the MR damper; k_s is the air spring stiffness in the secondary suspension; k_p and c_p are the primary suspension stiffness and damping, respectively; x_t is the track irregularities. The parameters for the quarter car model are shown in **Table 5.1**. The equations can be rewritten in the form of

$$\mathbf{M\ddot{q}} + \mathbf{C\dot{q}} + \mathbf{Kq} = \mathbf{u} + \mathbf{w} \tag{5.3}$$

where

$$\mathbf{q} = \begin{bmatrix} x_s \\ x_u \end{bmatrix} \tag{5.4}$$

$$\mathbf{M} = \begin{bmatrix} m_s & 0 \\ 0 & m_u \end{bmatrix} \tag{5.5}$$

$$\mathbf{K} = \begin{bmatrix} k_s & -k_s \\ -k_s & k_s + k_p \end{bmatrix} \tag{5.6}$$

$$\mathbf{C} = \begin{bmatrix} 0 & 0 \\ 0 & c_p \end{bmatrix} \tag{5.7}$$

$$\mathbf{u} = \begin{bmatrix} -f_{mr} \\ f_{mr} \end{bmatrix} \tag{5.8}$$

$$\mathbf{w} = \begin{bmatrix} 0 \\ k_p x_t + c_p \dot{x}_t \end{bmatrix} \tag{5.9}$$

5.2.1 Skyhook control

Prior to directly applying negative stiffness dynamics to the system, let's examine the negative stiffness effect which is inherent in the skyhook control. Skyhook control is widely known as an effective tool of reducing the absolute response of a suspension system. Skyhook damping is employed herein to attenuate the vertical vibrations of the car body, m_s. The damper force is commanded according to the imaginary skyhook damper against a reference point in the sky, as seen in **Figure 5.2**. The damper force is thus expressed as

$$f_{sh} = c_{sh} \dot{x}_s \tag{5.10}$$

where c_{sh} refers to a prescribed skyhook damping; $\dot{x}_s$ is the absolute velocity of sprung mass, which is usually obtained by integrating the measured acceleration of sprung mass.

Numerical analysis of the quarter car model with the skyhook conducted is then conducted. The skyhook damping is selected as 50 kN·s/m. The sinusoidal wave with the displacement amplitude of 10 mm and at a frequency of 2 Hz is adopted as the track excitation. The comparisons of the sprung mass responses between skyhook and viscous damping are depicted in **Figure 5.3**. The force-displacement and force-velocity loops are depicted in **Figure 5.4 Force-displacement and force-velocity of damper**. Note that the *x*-axle of the force-displacement loops is the displacement across the damper, equivalently the relative displacement between the sprung mass and the unsprung mass; similarly, the *x*-axle of the force-velocity loops is the velocity across the damper. The force-displacement and force-velocity trajectories both progress along a clockwise path with increasing time. It can be observed that, the skyhook control can effectively reduce the sprung mass's responses, compared with the passive damper. Up to 25% and 26% reduction in the maximum displacement and acceleration of the sprung mass are achieved, respectively. Additionally, evident from **Figure 5.4**, the apparent negative stiffness properties superimposed with the viscous damping is illustrated in skyhook control.

It can be observed that, skyhook damping is capable of excellent performance vibration suppression. However, it should be noted that, implementation of skyhook control requires the absolute velocity of the sprung mass, seen in Equation (5.10), which is usually difficult to acquire. And this motivates the alternative use of negative stiffness properties appeared in skyhook damping, which whereas only requires the relative displacement velocity between the sprung mass and the unsprung mass that is much easier to obtained.

5.2.2 Negative stiffness with viscous damping

Apparently, a negative stiffness properties superimposed with viscous damping appears in skyhook damping, as demonstrated in last section. It is intuitive to emulate the skyhook damping by a negative stiffness with viscous damping (short for NSV). The damper force can be expressed as

$$f_{nsv} = k_{nsv}(x_s - x_u) + c_{nsv}(\dot{x}_s - \dot{x}_u) \tag{5.11}$$

where k_{nsv} and c_{nsv} are the emulated stiffness and viscous damping, respectively. In particular, the stiffness k_{nsv} is a negative constant. Focusing on skyhook damping case presented in Section 5.2.1, the equivalent dynamic properties of Equation (5.11) are identified by data fitting as k_{nsv} = −140 kN/m and c_{nsv} = 18 kN·s/m. Numerical simulation is then conducted with the same sinusoidal excitation. The responses of the sprung mass are depicted in **Figure 5.5**. The force-displacement and force-velocity trajectories are illustrated in **Figure 5.6**. Both the force-displacement and force-velocity loops progress along a clockwise path with increasing time. It can be observed that, the emulated negative stiffness with viscous damping can fully represent the skyhook damping.

Numerical simulation is further conducted with an even lower negative stiffness property and the same viscous damping. and **Figure 5.7** show the responses of the sprung mass with suspension properties k_{nsv} = –300 kN/m and c_{nsv} = 18 kN·s/m. Up to 52% and 52% reduction in the maximum displacement and acceleration of the sprung mass are achieved, respectively, compared to the passive damping. Additionally, comparing sprung mass responses of imposed negative stiffness −140 kN/m (**Figure 5.5**) and –300 kN/m (**Figure 5.7**), an obvious phase ahead exhibits for the case k_{nsv} = –300 kN/m. It can be implied that, damping efficiency increases with decreasing stiffness. The quantitative study is conducted immediately in the next section.

The cases above refer to fully active control which can output the exact desired force. However, it should be noted that, the semi-active dampers can only generate dissipative force, i.e., the force in the same direction with velocity across the damper. Therefore, the active force, as portray in 2nd and 4th quadrants of force-displacement loop (**Figure 5.8**(a)), has to be clipped accordingly. Therefore, the semi-active control scheme for the emulated negative stiffness superimposed with viscous damping using MR damper is devolved into

$$f_{nsv} = \begin{cases} k_{nsv}(x_s - x_u) + c_{nsv}(\dot{x}_s - \dot{x}_u) & f_{des} \cdot (\dot{x}_s - \dot{x}_u) > 0 \\ f_{mr}(I = 0) & f_{des} \cdot (\dot{x}_s - \dot{x}_u) < 0 \end{cases} \tag{5.12}$$

where f_{mr} (I=0) represents the passive-off state of the MR damper; f_{des} indicates the desired control force calculated by Equation (5.11). The semi-active strategy of negative stiffness with viscous damping is equivalent to the semi-active skyhook control. It only requires the relative displacement feedback between the sprung mass and the unsprung mass, i.e., the displacement across the MR damper. **Figure 5.9** shows the responses of the sprung mass. Fluttering in accelerations of the sprung mass, or equivalently applied force, occurs due to the clipping. Around 28% and 17% reduction in the maximum displacement and acceleration are obtained. Although the clipped case still outperforms the passive suspension, the performance is considerably degraded compared to the unclipped case which obtains up to 52% and 52% reduction in the maximum displacement and acceleration.

5.2.3 Dynamic analysis of vehicle structure featuring negative stiffness with viscous damping

This section presents a quantitative analysis on the dynamics of the quarter car in terms of the imposed negative stiffness. The negative stiffness is assumed to be emulated by the actively control actuator, which indicates that no clipping action is required, and thus the system is linear. Focusing on a quarter car incorporating the active force emulated by negative stiffness with viscous damping, the equations of motion (Equation (5.3)) can be rewritten as

$$\mathbf{M}\ddot{\mathbf{q}} + \mathbf{C}\dot{\mathbf{q}} + \mathbf{K}\mathbf{q} = \mathbf{w} \tag{5.13}$$

Matrices **M**, **C**, and **K**, and vectors **q** and **w** are formulated as

$$\mathbf{q} = \begin{bmatrix} x_s \\ x_u \end{bmatrix} \tag{5.14}$$

$$\mathbf{M} = \begin{bmatrix} m_s & 0 \\ 0 & m_u \end{bmatrix} \tag{5.15}$$

$$\mathbf{K} = \begin{bmatrix} k_s + k_{nsv} & -k_s - k_{nsv} \\ -k_s - k_{nsv} & k_s + k_{nsv} + k_p \end{bmatrix} \tag{5.16}$$

$$\mathbf{C} = \begin{bmatrix} c_{nsv} & -c_{nsv} \\ -c_{nsv} & c_{nsv} + c_p \end{bmatrix} \tag{5.17}$$

$$\mathbf{w} = \begin{bmatrix} 0 \\ k_p x_t + c_p \dot{x}_t \end{bmatrix} \tag{5.18}$$

where k_{nsv} is the imposed negative stiffness and c_{cnv} is the viscous damping coefficient. Looking into the undamped system, which is described by

$$\mathbf{M}\ddot{\mathbf{q}} + \mathbf{K}\mathbf{q} = 0 \tag{5.19}$$

The eigenvalue problem is formulated by:

$$(\mathbf{K} - \omega^2 \mathbf{M})\mathbf{A} = 0 \tag{5.20}$$

The eigenvalues ω of the system can be obtained by solving this eigenvalue problem. Therefore, the natural frequencies of the sprung mass and unsprung mass of the quarter car are

$$f_s = \frac{1}{2\pi}\sqrt{\frac{\widetilde{\omega}_u^2 + \widetilde{\omega}_s^2}{2} + \sqrt{\Delta(\widetilde{\omega}_s^2, \widetilde{\omega}_u^2)}} \tag{5.21}$$

$$f_u = \frac{1}{2\pi}\sqrt{\frac{\widetilde{\omega}_u^2 + \widetilde{\omega}_s^2}{2} - \sqrt{\Delta(\widetilde{\omega}_s^2, \widetilde{\omega}_u^2)}} \tag{5.22}$$

where

$$\widetilde{\omega}_s = \sqrt{\frac{k_s + k_{nsv}}{m_s}} \tag{5.23}$$

$$\widetilde{\omega}_u = \sqrt{\frac{k_s + k_{nsv} + k_p}{m_u}} \tag{5.24}$$

$$\Delta = \left(\frac{\widetilde{\omega}_u^2 - \widetilde{\omega}_s^2}{2}\right)^2 + \frac{(k_s + k_{nsv})^2}{m_u m_s} \tag{5.25}$$

$\widetilde{\omega}_i^2$ ($i = u$, s) is the natural frequency of the constraint substructure of the sprung mass and the unsprung mass, respectively.

The natural frequency of sprung mass varies with increasing stiffness, as presented in **Figure 5.10**. It can be implied that, it is favorable to adjust the emulated stiffness properties to avoid the resonant motion of the entire structure. The damping ratio of sprung mass increases as stiffness component decreases, as presented in **Figure 5.11**. Likewise, incorporation of the negative stiffness into the quarter car can enhance the energy dissipating capability.

5.2.4 Negative stiffness with friction damping

The negative stiffness superimposed with viscous damping inevitably involves clipping, to deal with active force which cannot be realized by a semi-active damper. The energy spillover associated with the clipped action would be introduced into the dynamic system, which results in exciting other vibrating modes, and degrading the suspension performance. It is rational to avoid this by introducing friction damping to replace the viscous damping; thus, the damper force has an expression as

$$f_{nsf} = k_{nsf}(x_s - x_u) + f_c sign(\dot{x}_s - \dot{x}_u) \tag{5.26}$$

where f_c denotes the Coulomb friction force; function sign(·) takes the sign of the velocity across the damper. Let x_{su} be the damper displacement amplitude. Then if k_{nsf} $x_{su} < f_c$, the generated force only exhibits dissipative value; otherwise, Equation (5.12) will have to be clipped, to deal with the non-dissipative force. The semi-active scheme for negative stiffness with friction damping becomes

$$f = \begin{cases} k_{nsf}(x_s - x_u) + f_c sign(\dot{x}_s - \dot{x}_u) & f_{des} \cdot (\dot{x}_s - \dot{x}_u) > 0 \\ f_{mr}(I = 0) & f_{des} \cdot (\dot{x}_s - \dot{x}_u) < 0 \end{cases} \tag{5.27}$$

Considering the lower-bound force at the passive-off state of the MR damper introduced in Chapter 4, the parameters are selected as $k_{nsf} = -140$ kN/m and f_{fri} = 1.8 kN, to avoid the clipping action. **Figure 5.12** and **Figure 5.13** show the responses of the sprung mass, and the force-displacement displacement and force-velocity loops of the damper, respectively. 32% and 17% reduction in the maximum displacement and acceleration are observed. The effectiveness slightly outperforms in comparison with the case of clipped negative stiffness with viscous damping. The fluttering of acceleration is avoided. In addition, there exhibits a release as the acceleration or the damper force of the sprung mass reaches its maximum and the displacement reaches its minimum.

5.2.4 Simulations

In order to investigate and compare the effectiveness of the negative stiffness component on the vibration attenuation for rail vehicle, numerical analysis is conducted on three kinds of suspensions, i.e., viscous damping, clipped negative stiffness with viscous damping (semi-active skyhook damping), and non-clipped negative stiffness with friction damping. The vehicle runs at a speed of 200 km/h on a straight track with random track irregularities. The random track irregularities adopted are collected from the Qinhuangdao-Shenyang Railway Line, China. The simulation is performed in MATLAB Simulink. The simulation time period is 30 s. The fixed-step time is set as 0.001 s. Therefore, there are 30001 samples in total. The obtained root mean square (RMS) of the displacement and acceleration is shown in **Table 5.2**. The index frequency count of response that is grouped according to the spaced numeric ranges is adopted to quantify the performance of the three suspensions. **Figure 5.14** and **Figure 5.15** shows the frequency counts of the displacements and accelerations of the car body, respectively. Improvements in response suppression can be observed both for clipped negative stiffness with viscous damping and negative stiffness, compared with the solely viscous damping. It is worth noting that, with respect to the displacement responses, a slightly better performance can be achieved by clipped negative stiffness and viscous damping in small displacements. The displacement response of the sprung mass appears mostly below 3 mm. It implies that, the energy is mostly dissipated. On the other hand, focusing on the acceleration response, the non-slipped negative stiffness with friction damping outperforms the others. The friction damping can effectively avoid the fluttering of the damper forces to the sprung mass, or equivalently, the acceleration responses, which is consistent with the illustration with sinusoidal excitation. The negative stiffness with friction damping can better facilitate the passenger ride comfort of a railway vehicle.

5.3 Simulation of a full-scale railway vehicle incorporated with negative stiffness

5.3.1 15-DOF vehicle model for full-scale high-speed train integrated with MR dampers

As shown in **Figure 5.16**, a 15-DOF vehicle model for full-scale high-speed train integrated with MR dampers is established. The captured model consists of a car body, two truck frames, and four wheelsets. The primary suspension connects the wheelsets and the truck frame, while the secondary suspension connects the truck frame and the car body. The wheels of the train make contact with the indeterministic track (i.e., straight track). The MR dampers are installed within the secondary suspension in the lateral direction to replace the existing passive dampers. They are considered to account for the attenuation of the car body lateral vibrations induced by the random track irregularities. Since the lateral dynamics of the train is of primary concern in this research, only the lateral translation, yaw motion and roll motion which are relevant to the lateral dynamics are included in model dynamics representation, while the vertical dynamics (i.e., vertical translation and pitch motion) and the longitudinal motion are ignored. The 15 DOFs of the train model are detailed in **Table 5.3**. Amongst, the lateral motions of car body, trucks, and wheelsets are measureable, and the other (yaw and roll motion) can be calculated from the measured lateral motions. The parameters for the railway vehicle are listed in **Table 5.4**. The governing equations of the motion of the high-speed train car body, bogie and wheelsets are formulated as followed.

(1) Car body dynamics

The car body dynamic behavior is characterized by the lateral translation (y_c), yaw motion (φ_c) and roll motion (θ_c). The equations of motion are as follow.

$$m_c\ddot{y}_c = F_{syll} + F_{sylr} + F_{sytl} + F_{sytr} \tag{5.28}$$

$$\begin{aligned} I_{cz}\ddot{\varphi}_c = &\left(F_{syll} + F_{sylr}\right)l - \left(F_{sytl} + F_{sytr}\right)l + (F_{sxll} - F_{sxlr})d_s \\ &+(F_{sxtl} - F_{sxtr})d_s \end{aligned} \tag{5.29}$$

$$\begin{aligned} I_{cx}\ddot{\theta}_c = &(F_{szlr} - F_{szll})d_s + (F_{sztr} - F_{sztl})d_s - \left(F_{sylr} + F_{syll}\right)h_{cs} \\ &-\left(F_{sytr} + F_{sytl}\right)h_{cs} \end{aligned} \tag{5.30}$$

(2) Truck dynamics

The high-speed train includes two truck frames, identified as front truck and rear truck, as depicted in **Figure 5.16**. The truck dynamics of the high-speed train is described by the lateral translation (y_{ti}) and yaw motion (θ_{ti}), in which the subscript i = 1, 2 (1 denotes the front truck and 2 the rear truck).

The governing equations of the front truck dynamics are formulated as follow.

$$m_{t1}\ddot{y}_{t1} = -\left(F_{syll} + F_{sylr}\right) + F_{py1l} + F_{py1r} + F_{py2l} + F_{py2r} \tag{5.31}$$

$$\begin{aligned} I_{t1}\ddot{\varphi}_{t1} = -(F_{sxll} - F_{sxlr})d_s + \left(F_{px1l} - F_{px1r}\right)d_p + \left(F_{px2l} - F_{px2r}\right)d_p \\ +\left(F_{py1l} + F_{px1r}\right)b - \left(F_{py2l} + F_{py2r}\right)b \end{aligned} \tag{5.32}$$

The governing equations of the rear truck dynamics are formulated as followed.

$$m_{t2}\ddot{y}_{t2} = -\left(F_{sytl} + F_{sytr}\right) + F_{py3l} + F_{py3r} + F_{py4l} + F_{py4r} \tag{5.33}$$

$$\begin{aligned} I_{t2}\ddot{\varphi}_{t2} = -(F_{sxtl} - F_{sxtr})d_s + \left(F_{px3l} - F_{px3r}\right)d_p + \left(F_{px4l} - F_{px4r}\right)d_p \\ +\left(F_{py3l} + F_{px3r}\right)b - \left(F_{py4l} + F_{py4r}\right)b \end{aligned} \tag{5.34}$$

(3) Wheelset dynamics

The presented railway vehicle consists of four wheelset, two connecting to the leading truck and the other two connecting to the trailing truck. The wheelsets are considered to make contact with the straight tracks. The dynamic behavior of the wheelsets is characterized by the lateral translation (y_{wi}) and yaw motion (φ_{wi}), in which subscript i =1, 2, 3, 4 (1 denotes the front truck leading wheetset, 2 the front truck trailing wheelset, 3 the rear truck leading wheelset, and 4 the rear truck trailing wheetlset).

The equations of motion for the front truck leading wheelset are given by

$$m_{w1}\ddot{y}_{w1} = -\left(F_{py1l} + F_{py1r}\right) + F_{ty1l} + F_{ty1r} \tag{5.35}$$

$$I_{w1}\ddot{\varphi}_{w1} = -(F_{px1l} - F_{px1r})d_p \tag{5.36}$$

The equations of motion for the front truck trailing wheelset are given by

$$m_{w2}\ddot{y}_{w2} = -\left(F_{py2l} + F_{py2r}\right) + F_{ty2l} + F_{ty2r} \tag{5.37}$$

$$I_{w2}\ddot{\varphi}_{w2} = -(F_{px2l} - F_{px2r})d_p \tag{5.38}$$

The equations of motion for the rear truck leading wheelset are given by

$$m_{w3}\ddot{y}_{w3} = -\left(F_{py3l} + F_{py3r}\right) + F_{ty3l} + F_{ty3r} \tag{5.39}$$

$$I_{w3}\ddot{\varphi}_{w3} = -(F_{px3l} - F_{px3r})d_p \tag{5.40}$$

The equations of motion for the rear truck trailing wheelset are given by

$$m_{w4}\ddot{y}_{w4} = -\left(F_{py4l} + F_{py4r}\right) + F_{ty4l} + F_{ty4r} \tag{5.41}$$

$$I_{w4}\ddot{\varphi}_{w4} = -(F_{px4l} - F_{px4r})d_p \tag{5.42}$$

(4) Suspension forces

The suspension forces of the secondary suspension system are given by

$$F_{sxll} = -k_{sx}(\varphi_c - \varphi_{t1})d_s - c_{sx}(\dot{\varphi}_c - \dot{\varphi}_{t1})d_s \tag{5.43}$$

$$F_{sxlr} = k_{sx}(\varphi_c - \varphi_{t1})d_s + c_{sx}(\dot{\varphi}_c - \dot{\varphi}_{t1})d_s \tag{5.44}$$

$$F_{sxtl} = -k_{sx}(\varphi_c - \varphi_{t2})d_s - c_{sx}(\dot{\varphi}_c - \dot{\varphi}_{t2})d_s \tag{5.45}$$

$$F_{sxtr} = k_{sx}(\varphi_c - \varphi_{t2})d_s + c_{sx}(\dot{\varphi}_c - \dot{\varphi}_{t2})d_s \tag{5.46}$$

$$F_{syll} = -k_{sy}(y_c - y_{t1} + \varphi_c l - \theta_c h_{cs}) - c_{sy}\left(\dot{y}_c - \dot{y}_{t1} + \dot{\varphi}_c l - \dot{\theta}_c h_{cs}\right) - f_{syll} \tag{5.47}$$

$$F_{sylr} = -k_{sy}(y_c - y_{t1} + \varphi_c l - \theta_c h_{cs}) - c_{sy}\left(\dot{y}_c - \dot{y}_{t1} + \dot{\varphi}_c l - \dot{\theta}_c h_{cs}\right) - f_{sylr} \tag{5.48}$$

$$F_{sytl} = -k_{sy}(y_c - y_{t2} - \varphi_c l - \theta_c h_{cs} l) - c_{sy}\left(\dot{y}_c - \dot{y}_{t2} - \dot{\varphi}_c l - \dot{\theta}_c h_{cs}\right) - f_{sytl} \tag{5.49}$$

$$F_{sytr} = -k_{sy}(y_c - y_{t2} - \varphi_c l - \theta_c h_{cs} l) - c_{sy}\left(\dot{y}_c - \dot{y}_{t2} - \dot{\varphi}_c l - \dot{\theta}_c h_{cs}\right) - f_{sytr} \tag{5.50}$$

$$F_{szll} = k_{sz}\theta_c d_s + c_{sz}\dot{\theta}_c d_s \tag{5.51}$$

$$F_{szlr} = -k_{sz}\theta_c d_s - c_{sz}\dot{\theta}_c d_s \tag{5.52}$$

$$F_{sztl} = k_{sz}\theta_c d_s + c_{sz}\dot{\theta}_c d_s \tag{5.53}$$

$$F_{sztl} = -k_{sz}\theta_c d_s - c_{sz}\dot{\theta}_c d_s \tag{5.54}$$

The suspension forces of the primary suspension are given by

$$F_{px1l} = -k_{px}(\varphi_{t1} - \varphi_{w1})d_p - c_{px}(\dot{\varphi}_{t1} - \dot{\varphi}_{w1})d_p \tag{5.55}$$

$$F_{px1r} = k_{px}(\varphi_{t1} - \varphi_{w1})d_p + c_{px}(\dot{\varphi}_{t1} - \dot{\varphi}_{w1})d_p \tag{5.56}$$

$$F_{px2l} = -k_{px}(\varphi_{t1} - \varphi_{w2})d_p - c_{px}(\dot{\varphi}_{t1} - \dot{\varphi}_{w2})d_p \tag{5.57}$$

$$F_{px2r} = k_{px}(\varphi_{t1} - \varphi_{w2})d_p + c_{px}(\dot{\varphi}_{t1} - \dot{\varphi}_{w2})d_p \tag{5.58}$$

$$F_{px3l} = -k_{px}(\varphi_{t2} - \varphi_{w3})d_p - c_{px}(\dot{\varphi}_{t2} - \dot{\varphi}_{w3})d_p \tag{5.59}$$

$$F_{px3r} = k_{px}(\varphi_{t2} - \varphi_{w3})d_p + c_{px}(\dot{\varphi}_{t2} - \dot{\varphi}_{w3})d_p \tag{5.60}$$

$$F_{px4l} = -k_{px}(\varphi_{t2} - \varphi_{w4})d_p - c_{px}(\dot{\varphi}_{t2} - \dot{\varphi}_{w4})d_p \tag{5.61}$$

$$F_{px4r} = k_{px}(\varphi_{t2} - \varphi_{w4})d_p + c_{px}(\dot{\varphi}_{t2} - \dot{\varphi}_{w4})d_p \tag{5.62}$$

$$F_{py1l} = -k_{py}(y_{t1} - y_{w1} + \varphi_{t1}b) - c_{py}(\dot{y}_{t1} - \dot{y}_{w1} + \dot{\varphi}_{t1}b) \tag{5.63}$$

$$F_{py1r} = -k_{py}(y_{t1} - y_{w1} + \varphi_{t1}b) - c_{py}(\dot{y}_{t1} - \dot{y}_{w1} + \dot{\varphi}_{t1}b) \tag{5.64}$$

$$F_{py2l} = -k_{py}(y_{t1} - y_{w2} - \varphi_{t1}b) - c_{py}(\dot{y}_{t1} - \dot{y}_{w2} - \dot{\varphi}_{t1}b) \tag{5.65}$$

$$F_{py2r} = -k_{py}(y_{t1} - y_{w2} - \varphi_{t1}b) - c_{py}(\dot{y}_{t1} - \dot{y}_{w2} - \dot{\varphi}_{t1}b) \tag{5.66}$$

$$F_{py3l} = -k_{py}(y_{t2} - y_{w3} + \varphi_{t2}b) - c_{py}(\dot{y}_{t2} - \dot{y}_{w3} + \dot{\varphi}_{t2}b) \tag{5.67}$$

$$F_{py3r} = -k_{py}(y_{t2} - y_{w3} + \varphi_{t2}b) - c_{py}(\dot{y}_{t2} - \dot{y}_{w3} + \dot{\varphi}_{t2}b) \tag{5.68}$$

$$F_{py4l} = -k_{py}(y_{t2} - y_{w4} - \varphi_{t2}b) - c_{py}(\dot{y}_{t2} - \dot{y}_{w4} - \dot{\varphi}_{t2}b) \tag{5.69}$$

$$F_{py4r} = -k_{py}(y_{t2} - y_{w4} - \varphi_{t2}b) - c_{py}(\dot{y}_{t2} - \dot{y}_{w4} - \dot{\varphi}_{t2}b) \tag{5.70}$$

(5) Track irregularities

Forces transmitted from irregular track are given by

$$F_{ty1l} = -k_{ty}(y_{w1} - y_{e1l}) \tag{5.71}$$

$$F_{ty1r} = -k_{ty}(y_{w1} - y_{e1r}) \tag{5.72}$$

$$F_{ty2l} = -k_{ty}(y_{w2} - y_{e2l}) \tag{5.73}$$

$$F_{ty2r} = -k_{ty}(y_{w2} - y_{e2r}) \tag{5.74}$$

$$F_{ty3l} = -k_{ty}(y_{w3} - y_{e3l}) \tag{5.75}$$

$$F_{ty3r} = -k_{ty}(y_{w3} - y_{e3r}) \tag{5.76}$$

$$F_{ty3l} = -k_{ty}(y_{w4} - y_{e4l}) \tag{5.77}$$

$$F_{ty3r} = -k_{ty}(y_{w4} - y_{e4r}) \tag{5.78}$$

In Equations (5.14) – (5.56), F with different subscripts represents the suspension forces in different directions. In the subscripts of F, the first letter (s or p) represents the secondary or primary suspension, respectively; the second letter (x, y or z) represents the direction of the suspension force; the third letter (l, t, 1, 2, 3, or 4) represents vehicle components, i.e., 'l' is leading truck, 't' is trailing truck, '1' is the front wheel of the leading truck, '2' is the rear wheel of the leading truck, '3' is the front wheel of the trailing truck, and '4' is the rear wheel of the trailing truck. In Equations (33) – (36), f with similar subscripts represent the MR forces in the lateral direction. When the MR damper is installed to replace the existing passive damper, the c_{sy} which represents the damping coefficient of the passive damper is set as zero.

5.3.2 Semi-active Suspension systems for railway vehicle

Three kinds of suspension systems for railway vehicle using MR dampers are investigated in this section, including passive-off MR suspension, semi-active suspension with clipped negative stiffness superimposed with viscous damping, and semi-active suspension with negative stiffness superimposed with friction damping. The integrated vehicle runs on a straight track at a speed of 300 km/h with random irregularities inputs, which is collected from the Qinhuangdao-Shenyang Railway Line, China. The performance of the three suspensions are compared, by using simulated lateral, yaw and roll motion of car body, and lateral and yaw motion of trucks. The simulations are done in the context of MATLAB Simulink, as seen in **Figure 5.17**. The simulation time period is 30 s. The fixed-step time is set as 0.001 s. Therefore, there are 30001 samples in total.

5.3.2.1 MR suspension systems for railway vehicles

The MR dampers used in the simulations are the newly developed MR dampers introduced in Chapter 4. The Parameters are given in **Table 4.2**. The inverse dynamics of the captured MR dampers is employed to construct the damper controller, which emulate the desired dynamics. In this simulation, three kinds of suspensions are taken into account, which are:

(1) System *A*: passive suspension

The passive suspension is equipped with the existing passive hydraulic dampers of CRH3. The damping coefficient is 10 kN·s/m.

(2) System *B*: semi-active suspension with clipped negative stiffness properties with viscous damping

The damper force and displacement across the damper are monitored by the self-sensing MR damper and fed back to the damper controller to emulate the negative stiffness with viscous damping. Since the emulated dynamics inevitably involve active force, which is not possible with semi-active actuators, clipping action is required. According to clipping situation defined by Equation (5.11), the control current is tuned to zero, when the active force is desired.

In this case, the emulated negative stiffness is selected as -15 kN/s, around 10% of total stiffness of the secondary suspension in the lateral direction; the accompanying viscous damping is selected as 10 kN·s/m.

(3) System *C*: semi-active suspension with negative stiffness properties with friction damping

Likewise, the negative stiffness dynamics is emulated by the MR dampers with force and displacement feedback. Consider the lower force bound of the MR dampers, the negative stiffness is determined as the same with that of system B, and the friction damping is 500 N.

5.3.2.2 Simulations under random track irregularities

(1) Car body response

The RMS of vehicle body accelerations under random track irregularities is listed in **Table 5.5**. It is worth noting that, the roll motion of the three suspensions is way too small, compared to the other motions, i.e., lateral translation and yaw motion. It is probably because the vehicle is considered to run on a straight track, not to negotiate a curving, where roll motion strongly coupled with lateral translation is of significant. Therefore, roll motion is trivial in this case, and can be ignored. The acceleration time response within the given time range is showed in **Figure 5.18**. The amplitude spectrum of acceleration is portrayed in **Figure 5.19**.

It can be observed from **Table 5.5**, the RMS values of the lateral and yaw accelerations of vehicle body integrated with negative stiffness are lower than that of passive suspension, indicating the superior performance for vibration suppression of the integrated negative stiffness. Additionally, the RMS values of the systems *A* and *B*, which have the same stiffness property and yet different energy-dissipative patterns, are much similar. It is consistent with the time response histories portrayed in **Figure 5.18**. It implies that, the role of the negative stiffness in vibration suppression is of great importance.

Focusing on **Figure 5.19**, two resonant peaks of the lateral and the yaw motions of the vehicle body are all excited for the three suspensions. The two suspensions with emulated stiffness both work better than the passive-off suspension A in suppressing the two resonant modes simultaneously. There is no trade-offs between each other motions, which was observed in the full-scale demonstration experiments (in Chapter 3) when the control current is tuned louder. Likewise, the two suspensions with negative stiffness play the similar role in suppressing the motions.

(2) Damper motions

Figure 5.20 shows the outputting forces of the MR dampers (f_{syll} and f_{sylr}) installed within the leading truck of the three suspensions of railway vehicle under random irregularities inputs. **Figure 5.21** depicts the corresponding displacement across the MR dampers. And **Figure 5.22** shows the force-displacement loops of the MR dampers for the three suspensions over the entire simulation times.

Focusing on **Figure 5.20** and **Figure 5.21**, the three types of dampers behave similarly in terms of displacement, whereas the passive dampers output much larger damper forces than those of the other two. It is because that, the participation of negative stiffness lowers the outcome damper forces. Additionally, the MR dampers of System *C* output even lower damper force, compared with those of system *B*. Consider that their effectiveness on car body vibration mitigation is similar, it can be concluded that, the suspension *C* is more efficient than the suspension *B*. The negative stiffness properties of System *B* and *C* are illustrated in **Figure 5.22**.

(3) Truck responses

The RMS of vehicle body accelerations under random track irregularities is listed in **Table 5.6**. The amplitude spectrum of acceleration is portrayed in **Figure 5.23**.

It can be seen that, the RMS values of the lateral and yaw accelerations of truck for railway vehicle integrated with negative stiffness are larger than that of passive suspension, which behaves on the contrary to those obtained from vehicle body. It is consistent with amplitude spectrum showed in **Figure 5.23** that, the truck with passive system vibrates much less, while the trucks with emulated negative stiffness vibrate more intensively. It is beneficial for the objective of facilitating the passenger ride quality, by attenuating the vibrations of vehicle body.

5.4 Summary

In this chapter, negative stiffness properties emulated by MR damper are investigated for its vibration attenuation performance for train vehicle. Firstly, skyhook damping, negative stiffness with viscous damping, and negative stiffness with friction damping are demonstrated by integration with a quarter car. It is observed that, an apparent negative stiffness properties superimposed with the viscous damping is illustrated. All of these three strategies are capable of excellent performance vibration suppression. And direct emulation of negative stiffness outperforms skyhook damping, since implementation of skyhook control requires the absolute velocity of the sprung mass which is usually difficult to acquire, while application of direct negative stiffness only requires the relative displacement velocity between the sprung mass and the unsprung mass that is much easier to obtain. What is more, it can be observed that, introduction of negative stiffness properties is able to adjust the natural frequency of the entire structure, thereby avoiding resonant motion, and to enhance damping ratio of the structure.

Then the negative stiffness components are incorporated into secondary suspension for a CRH3 EMU. The motions of the railway vehicle were represented by a fifteen-degrees-of-freedom multi-body model. Numerical simulations investigated four types of suspensions, that is, passive-off suspension, passive-on suspension, semi-active skyhook suspension (equivalently negative stiff superimposed with viscous damping), and suspension with emulated negative stiffness superimposed with friction damping. The simulation results showed that, the fourth suspension outperformed the other three in reducing the lateral vibrations of the vehicle body. However, it also generates more vibrations in bogie than the other three suspensions. It is reasonable since the damper forces to car body and to bogie are a pair of action and reaction. A decrease in car body vibrations would cause an increase in bogie vibrations. On the other hand, MR damper, as a semi-active device, cannot generate active force. Therefore, emulation of negative stiffness properties usually involves clipping action. In view of this, negative stiffness superimposed with friction damping is capable of producing non-clipped semi-active force by adjusting yield force. Nevertheless, either clipping action or specific shaping would deteriorate its vibration attenuation performance to some extent.

To conclude, the introduction of the emulated dynamics would largely simplify the control implementation. In other words, the developed semi-active suspension was controlled to essentially vary its system characteristics, e.g. stiffness, according to the feedback within the vehicle system.

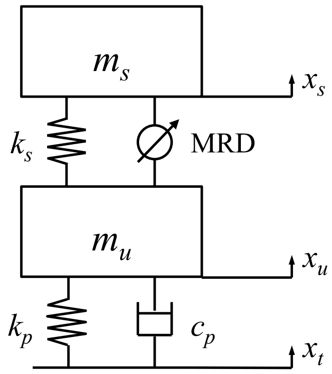

Figure 5.1 A quarter car incorporated with MR damper

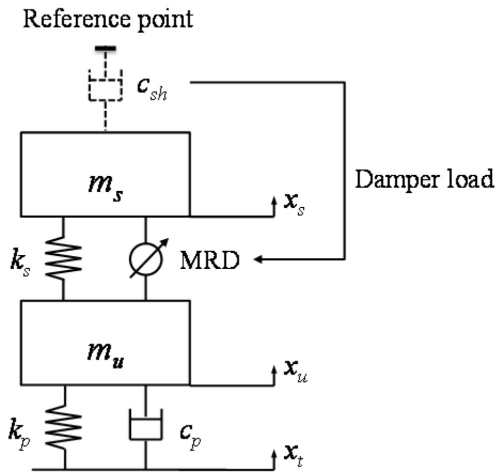

Figure 5.2 Skyhook control

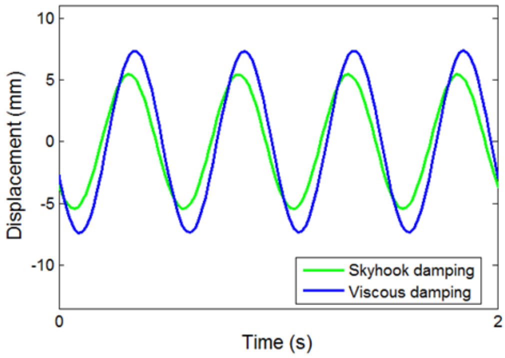

(a) Displacement of sprung mass

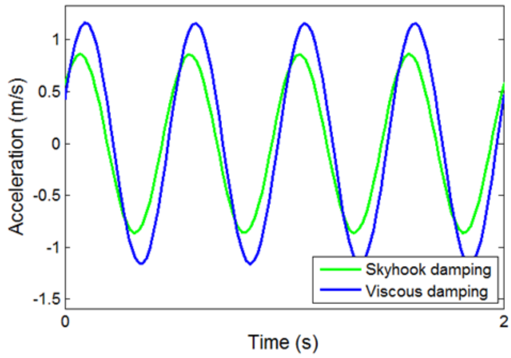

(b) Accelerations of sprung mass

Figure 5.3 Responses of sprung mass with skyhook damping

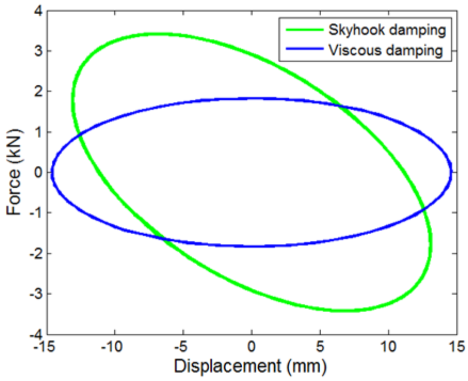

(a) Force versus displacement loop

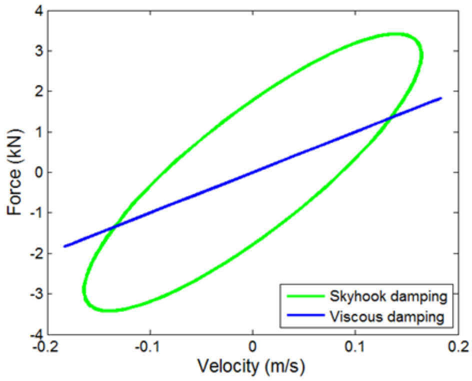

(b) Force versus velocity loop

Figure 5.4 Force-displacement and force-velocity of damper

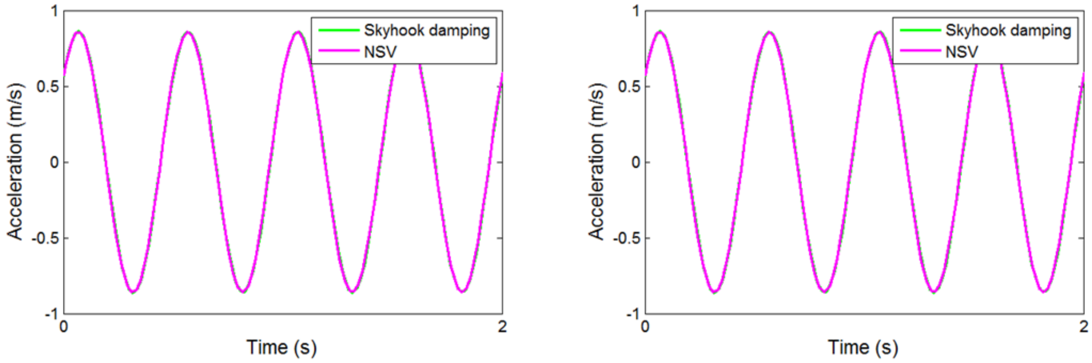

(a) Displacement of sprung mass (b) Accelerations of sprung mass

Figure 5.5 Responses of sprung mass with negative stiffness superimposed with viscous damping (*k* = - 140 kN/m)

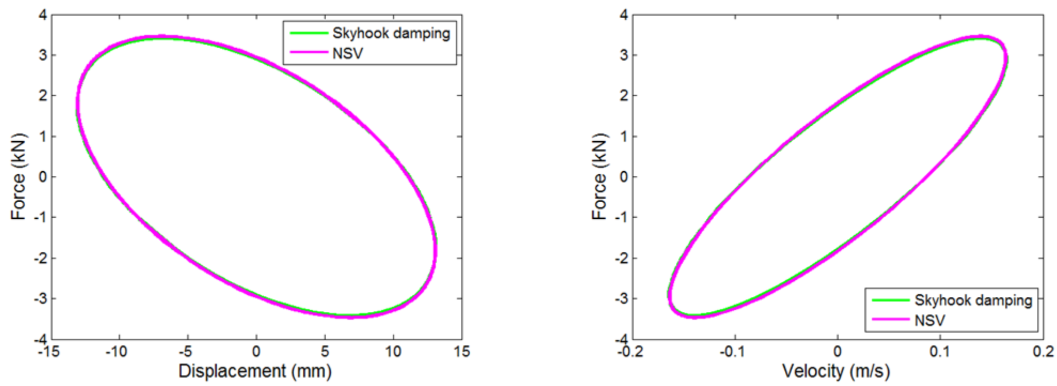

(a) Force versus displacement loop (b) Force versus velocity loop

Figure 5.6 Force-displacement and force-velocity of damper (*k* = - 140 kN/m)

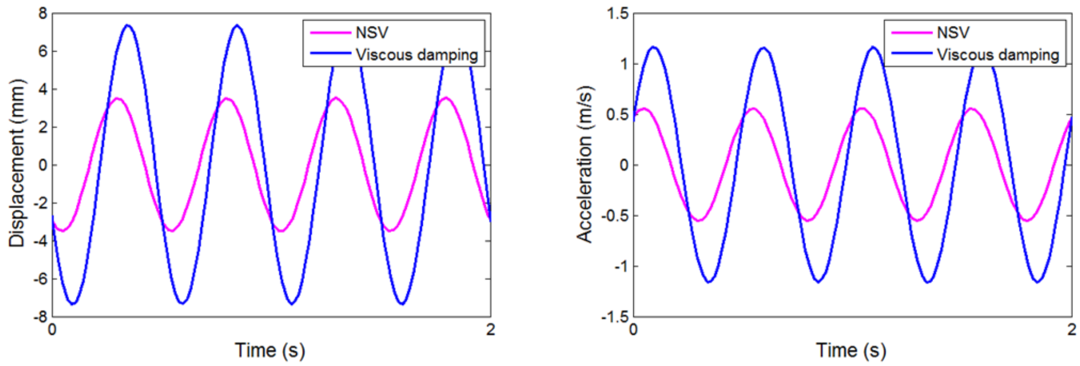

(a) Displacement of sprung mass (b) Accelerations of sprung mass

Figure 5.7 Responses of sprung mass with negative stiffness superimposed with viscous damping (*k* = - 300 kN/m)

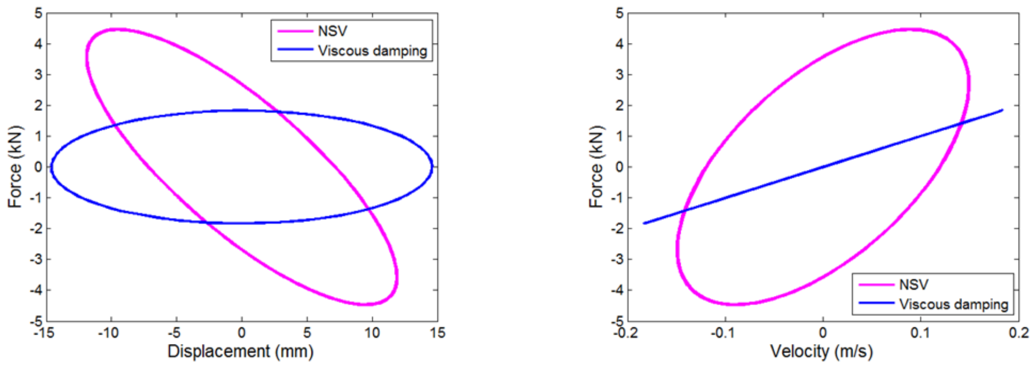

(a) Force versus displacement loop (b) Force versus velocity loop

Figure 5.8 Force-displacement and force-velocity of damper (*k* = - 300 kN/m)

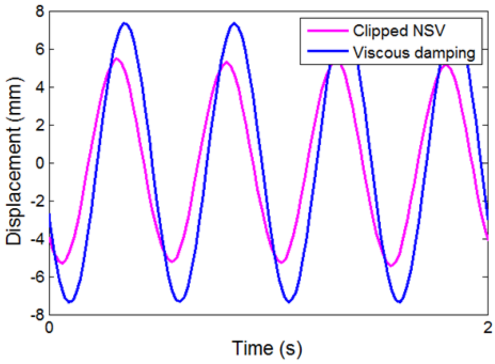

(a) Displacement of sprung mass

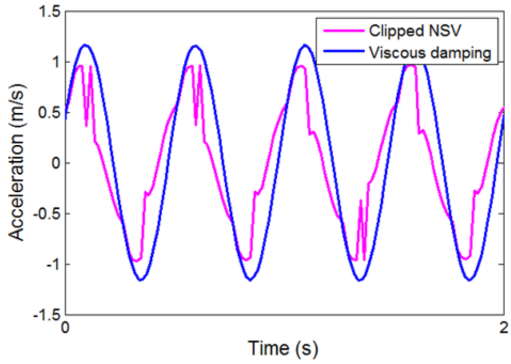

(b) Accelerations of sprung mass

Figure 5.9 Responses of sprung mass of clipped negative stiffness with viscous damping

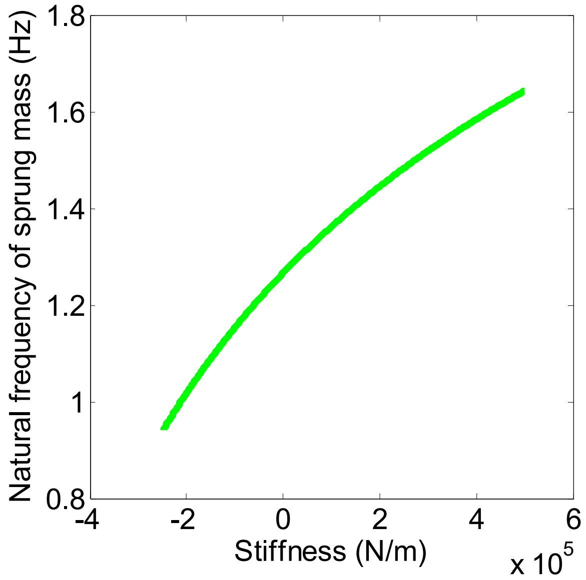

Figure 5.10 Varying natural frequency of sprung mass with increasing stiffness

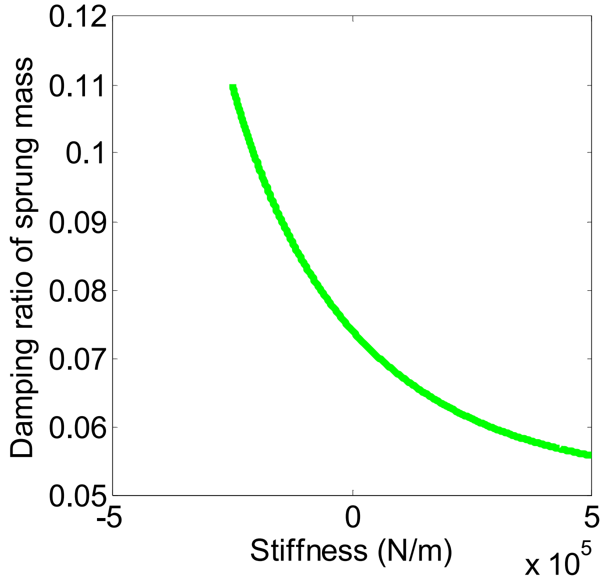

Figure 5.11 Varying damping ratio of sprung mass with increasing stiffness

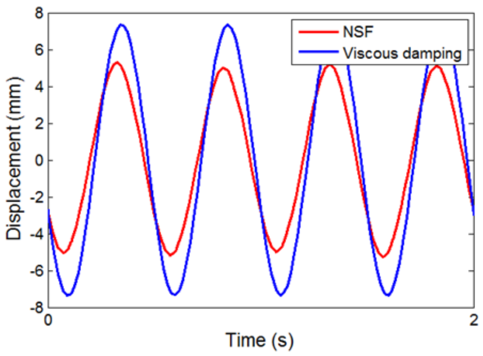

(a) Displacement of sprung mass

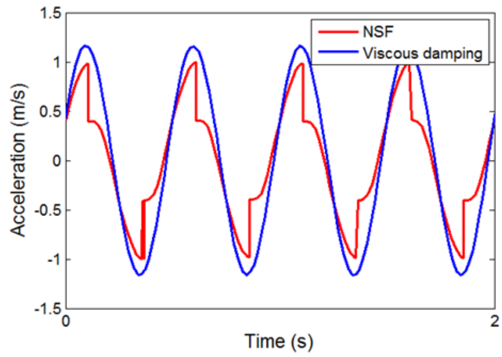

(b) Accelerations of sprung mass

Figure 5.12 Responses of sprung mass of clipped negative stiffness with friction damping

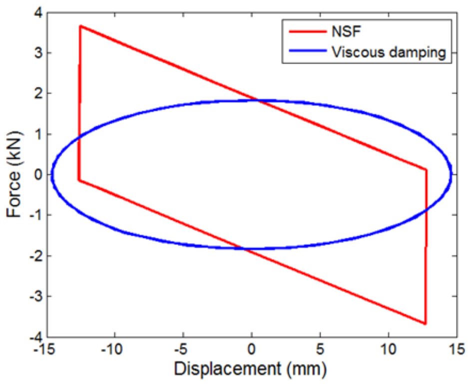

(a) Force versus displacement loop

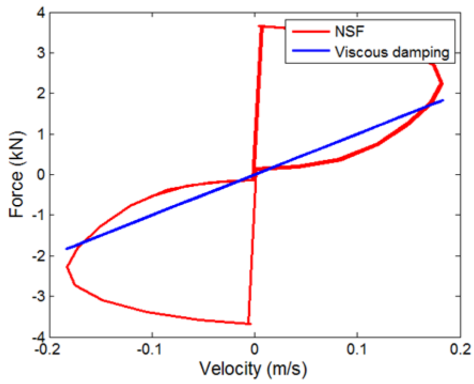

(b) Force versus velocity loop

Figure 5.13 Force-displacement and force-velocity loops of negative stiffness with friction damping

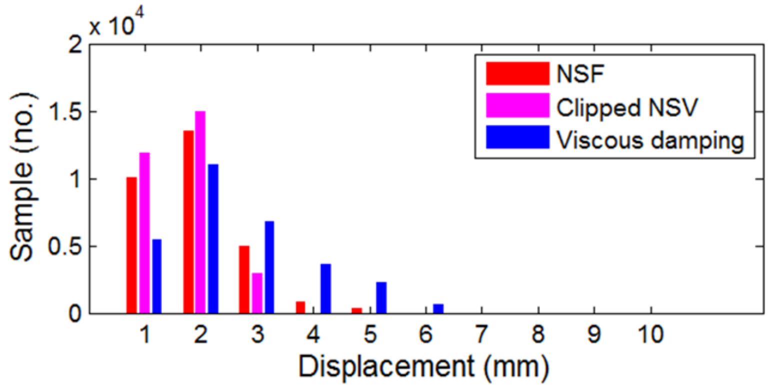

Figure 5.14 Frequency count of displacement responses of each spaced group

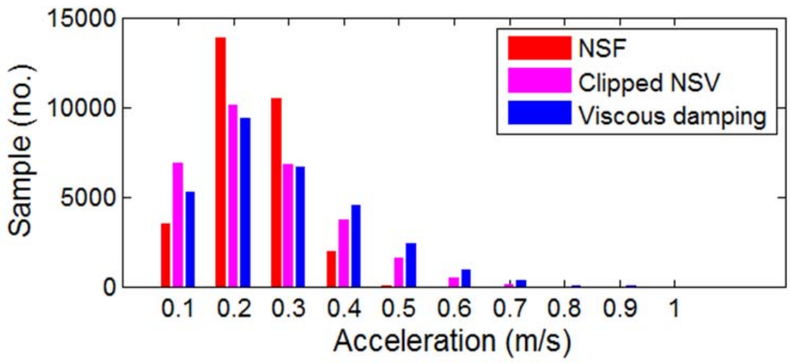

Figure 5.15 Frequency count of accelerations responses of each spaced group

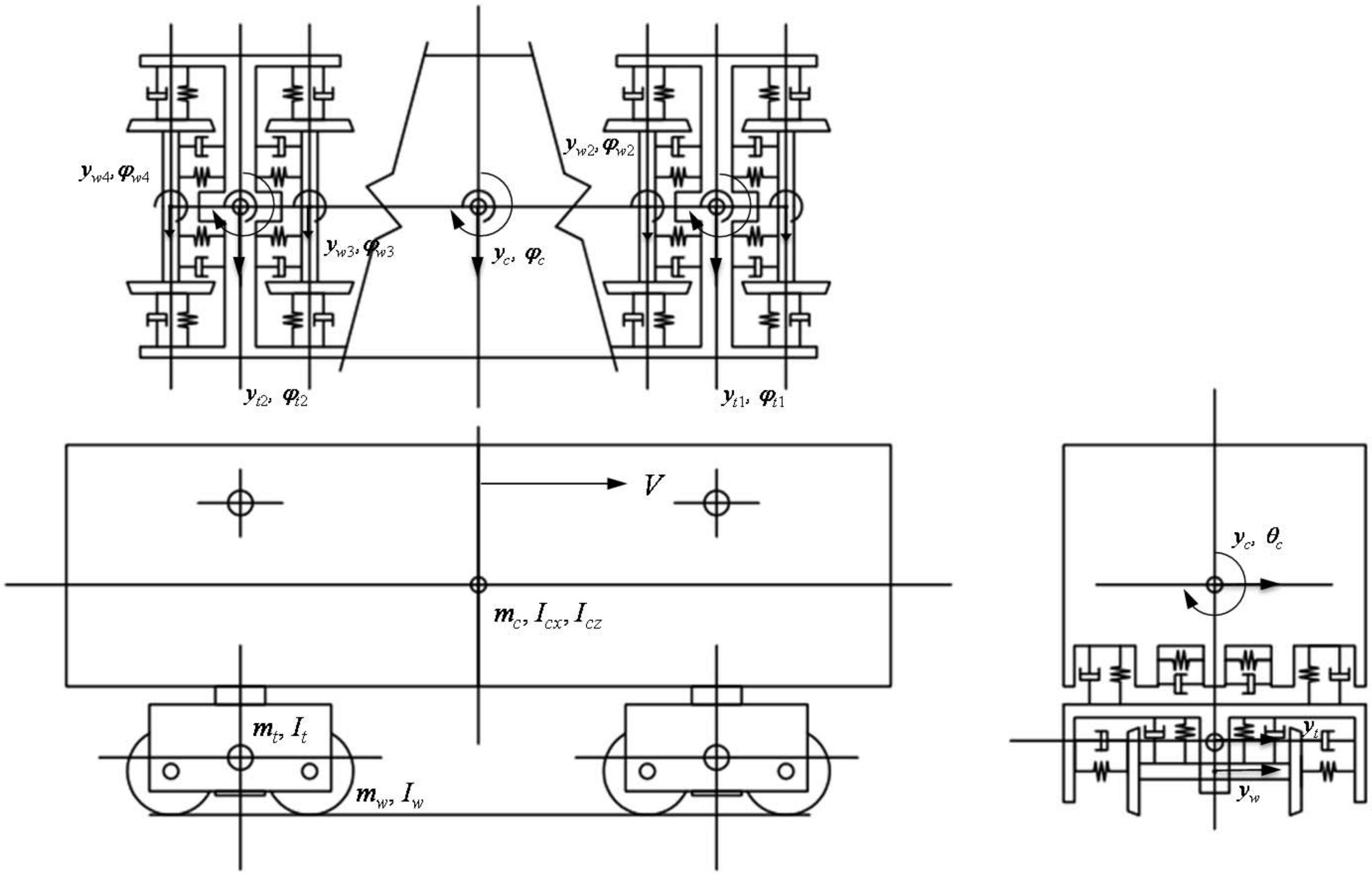

Figure 5.16 15-DOFs full-scale railway vehicle

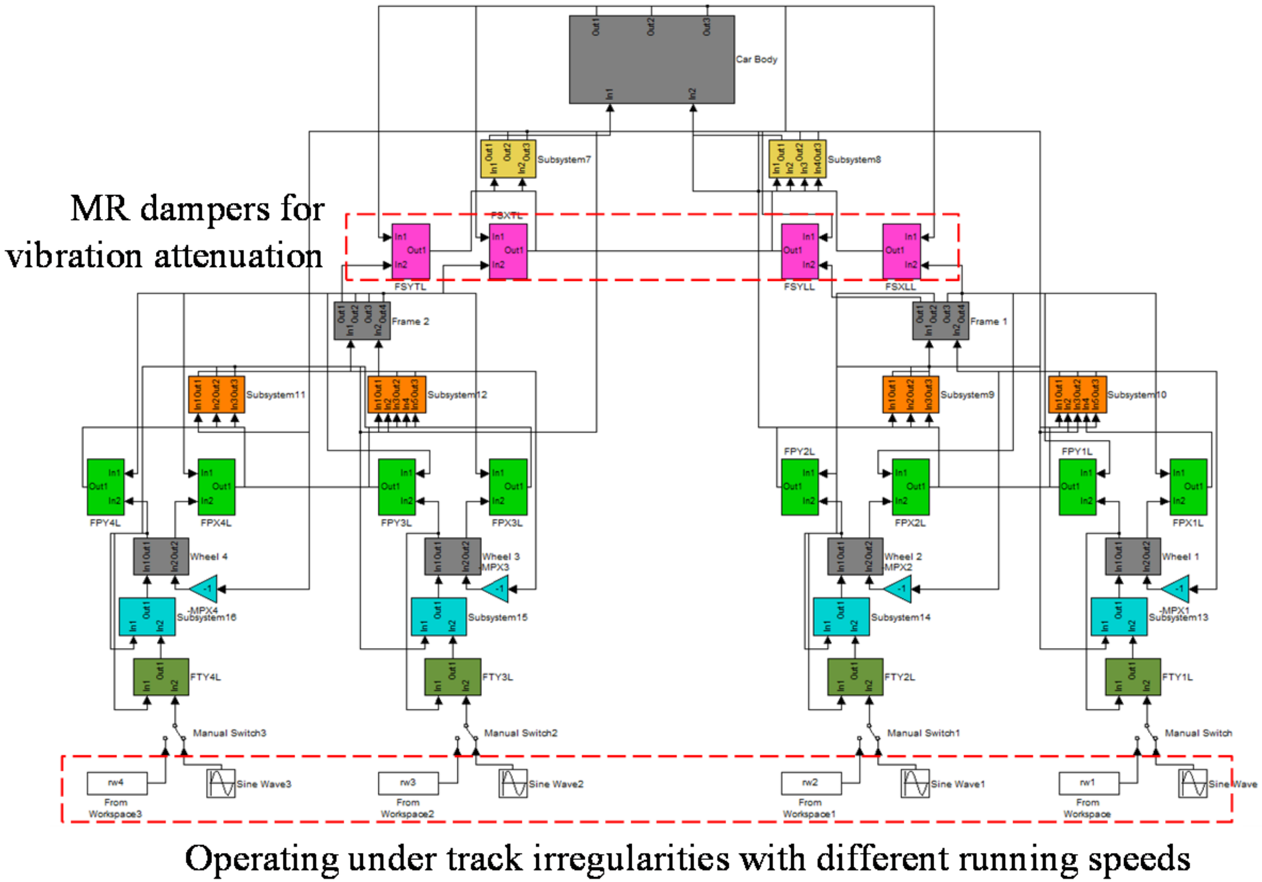

Figure 5.17 A 15-DOF railway vehicle model established by MATLAB Simulink

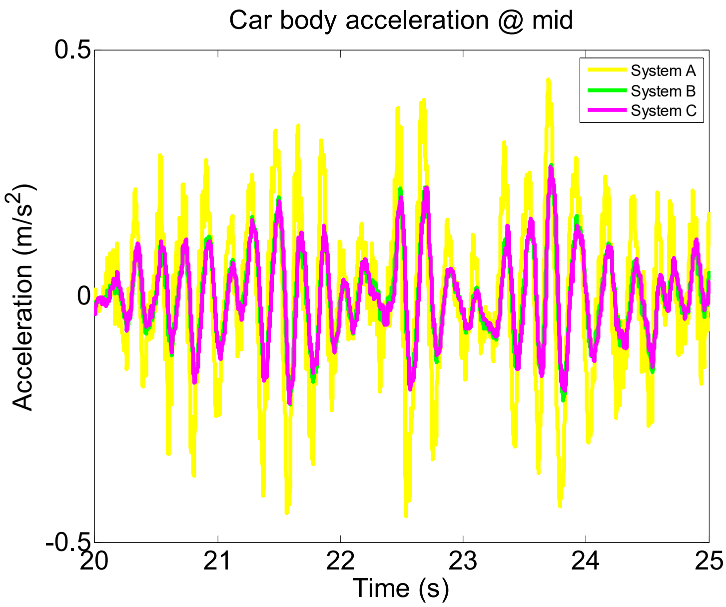

(a) Lateral acceleration responses

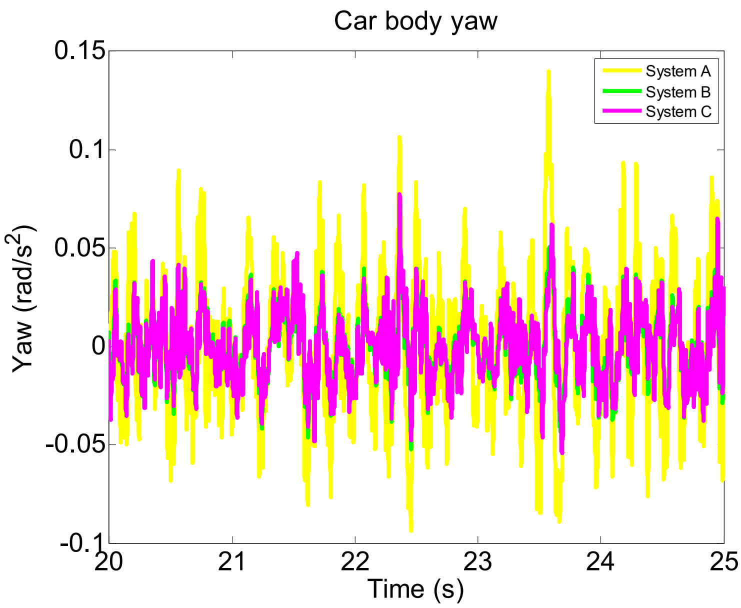

(b) Yaw acceleration responses

Figure 5.18 Time histories of car body accelerations under random track irregularities: (a) lateral acceleration, (b) yaw acceleration

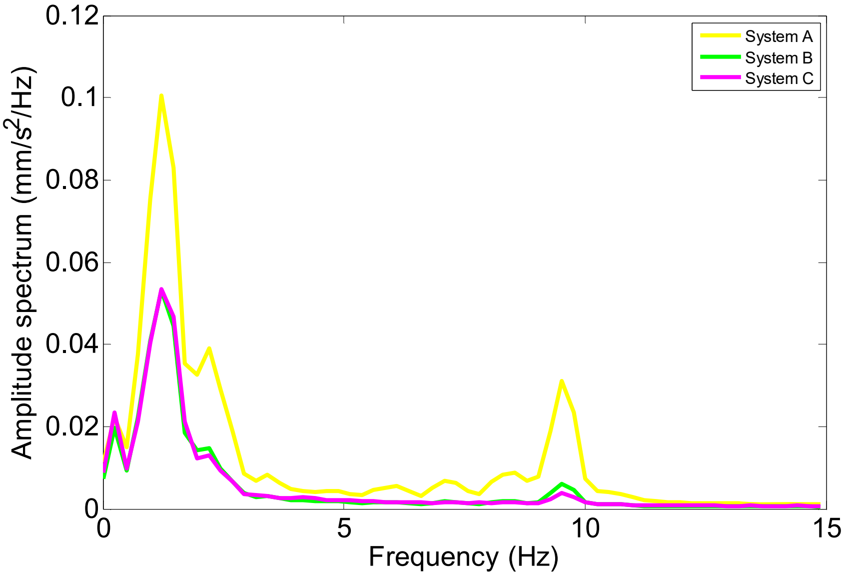

(a) Lateral acceleration

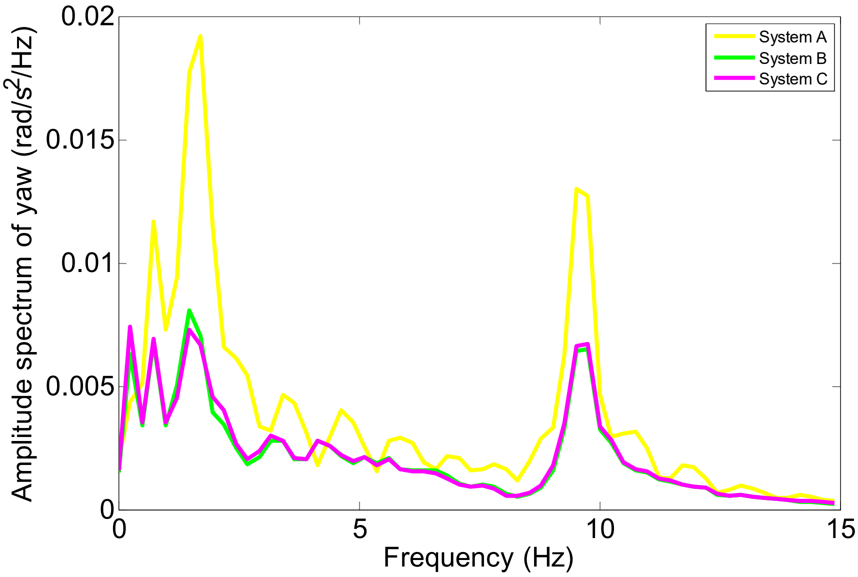

(b) Yaw acceleration

Figure 5.19 Amplitude spectrum of car body acceleration under random irregularities: (a) lateral acceleration, (b) yaw acceleration

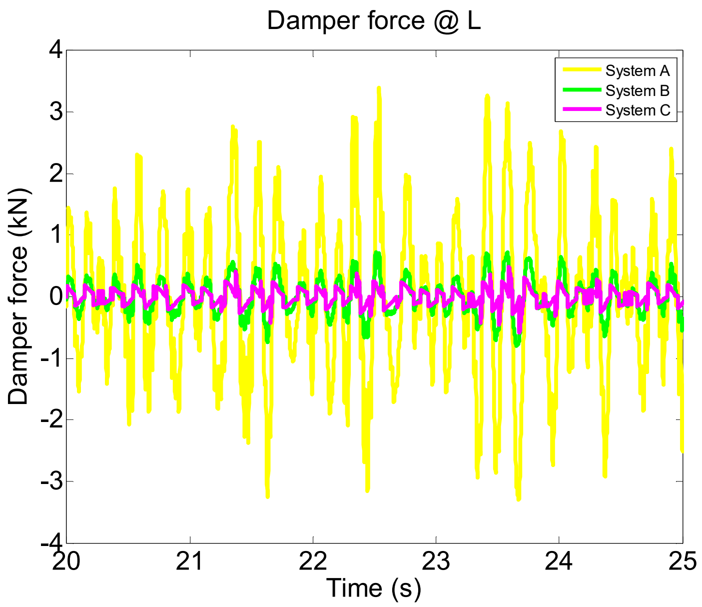

Figure 5.20 Time histories of damper force of MR dampers installed within front truck

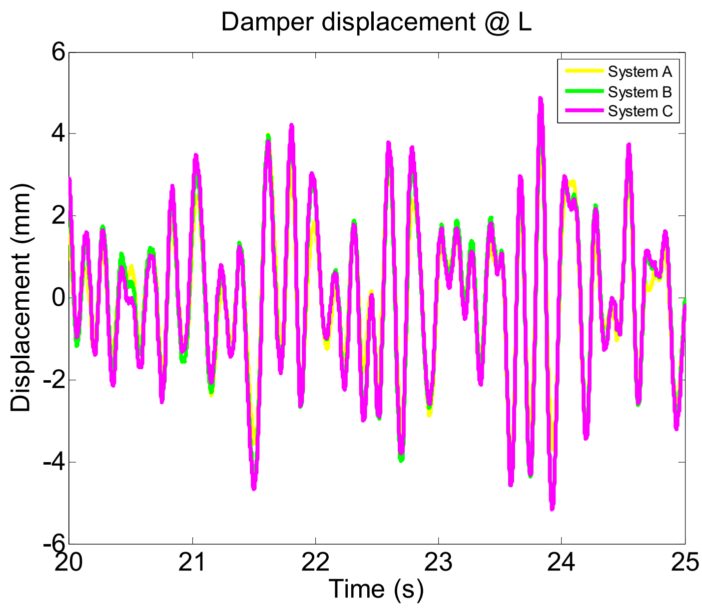

Figure 5.21 Time histories of displacement across MR dampers installed within front truck

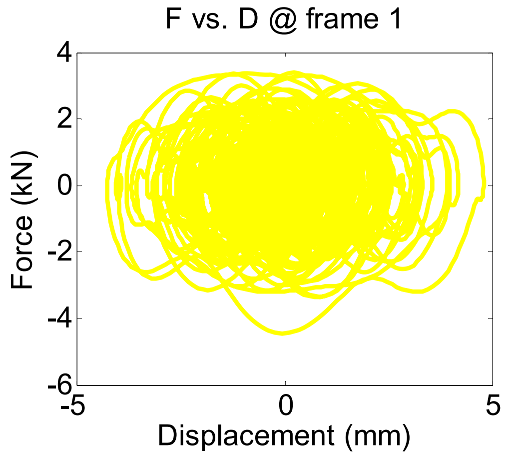

(a) System A: with passive dampers

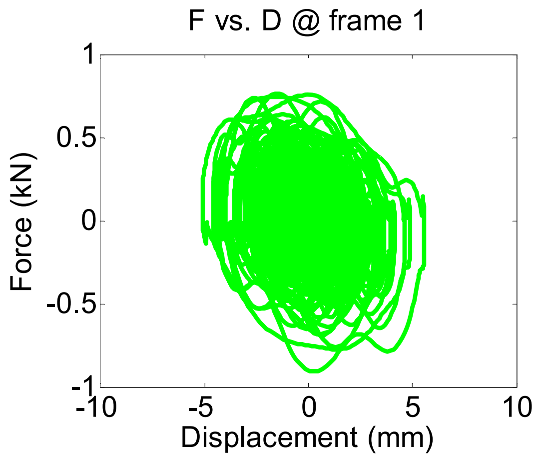

(b) System B: with clipped negative stiffness and viscous damping

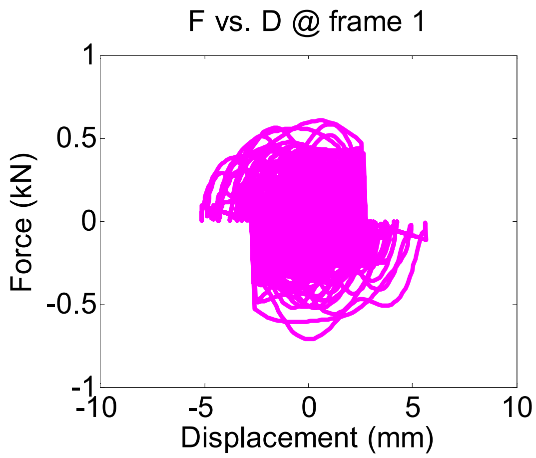

(c) System C: with negative stiffness and friction damping

Figure 5.22 Force-displacement trajectories of MR damper for three systems: (a) system A with passive dampers, (b) system B with clipped negative stiffness and viscous damping, and (c) system C with negative stiffness and friction damping

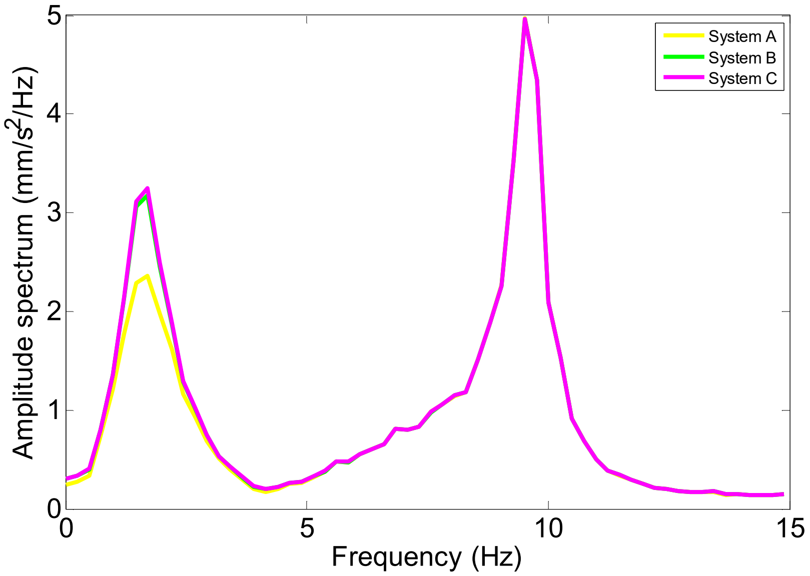

(a) Lateral acceleration

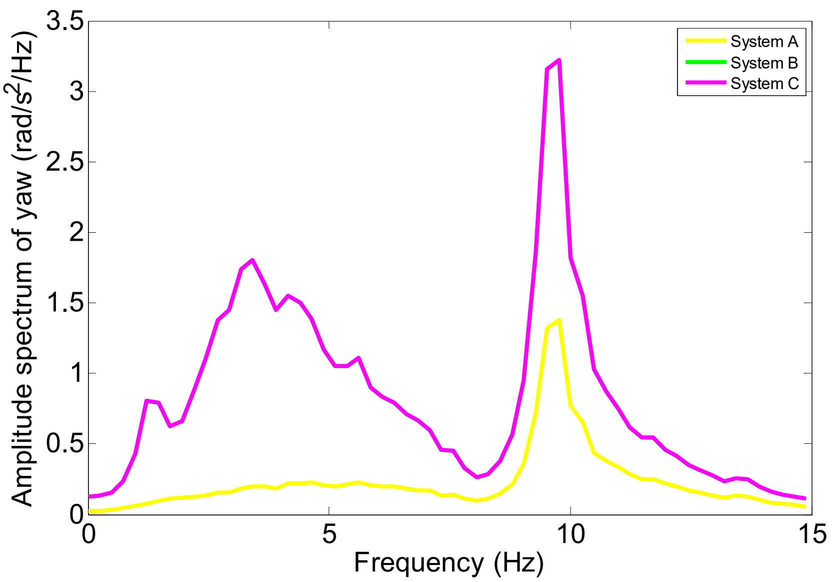

(b) Yaw acceleration

Figure 5.23 Amplitude spectrum of truck accelerations under random track irregularities: (a) lateral acceleration, (b) yaw acceleration

Table 5.1 Parameters of quarter car model

m_s (kg)	k_s (N/m)	c_s (N·s/m)	m_u (kg)	k_p (N/m)	c_p (N·s/m)
6500	5×10^5	10×10^3	1250	2.4×10^6	3×10^4

Table 5.2 RMS of car body for three suspensions

RMS	Viscous damping	Clipped negative stiffness with viscous damping	Non-clipped negative stiffness with friction damping
Displacement (mm)	0.0130	0.0059	0.0080
Acceleration (m/s^2)	0.0015	0.0012	0.0010

Table 5.3 Lateral motions of 15-DOF high-speed train model

Component		Motion		
		Lateral translation	Yaw motion	Roll motion
Car body		y_c (M)	φ_c (C)	θ_c (C)
Bogie	Front truck	y_{t1} (M)	φ_{t1} (C)	-
	Rear truck	y_{t2} (M)	φ_{t2} (C)	-
Wheelset	Front truck leading wheelset	y_{w1} (M)	φ_{w1} (C)	-
	Front truck trailing wheelset	y_{w2} (M)	φ_{w2} (C)	-
	Rear truck leading wheelset	y_{w3} (M)	φ_{w3} (C)	-
	Rear truck trailing wheetset	y_{w4} (M)	φ_{w4} (C)	-

Note that: M refers to DOF that is measureable; while C refers to that is calculated from measureable DOFs.

Table 5.4 Parameters for railway vehicle model CRH3

Nomenclature	Value	Unit
Centre distance between two trucks, $2l$	17500	*mm*
Wheel base, $2b$	2500	*mm*
Length of primary suspension, $2d_p$	2000	*mm*
Length of secondary suspension, $2d_s$	2460	*mm*
Length of car body and secondary suspension, h_{cs}	723	*mm*
Mass of car body, m_c	26.1	*t*
Moment of inertia of car body, I_{cz}	1102.73	$t{\cdot}m^2$
Moment of inertia of car body, I_{cx}	84.56	$t{\cdot}m^2$
Mass of truck, m_t	2.6	*t*
Moment of inertia of truck, I_t	2.6	$t{\cdot}m^2$
Mass of wheetset, m_w	2.1	*t*
Moment of inertia of wheetset, I_w	1.029	$t{\cdot}m^2$
Lateral steel spring in primary suspension, k_{py}	980	*kN/m*
Longitudinal steel spring in primary suspension, k_{px}	980	*kN/m*
Lateral damping in primary suspension, c_{py}	10	*kN·s/m*
Longitudinal damping in primary suspension, c_{px}	10	*kN·s/m*
Lateral air spring in secondary suspension, k_{sy}	158.76	*kN/m*
Longitudinal air spring in secondary suspension, k_{sx}	158.76	*kN/m*
Lateral hydraulic damper secondary suspension, c_{sy}	10	*kN·s/m*
Yaw damper, c_{sx}	440	*kN·s/m*

Table 5.5 RMS values of car body accelerations for three kinds of MR suspensions

	System A	System B	System C
Lateral (m/s^2)	0.1450	0.0740	0.0751
Yaw (rad/s^2)	0.0344	0.0177	0.0180
Roll (rad/s^2)	7.4148 – 005	1.1060 – 004	1.2597 – 004

Table 5.6 RMS values of car body accelerations for three kinds of MR suspensions

	System A	System B	System C
Lateral (m/s^2)	8.3311	8.8591	8.9024
Yaw (rad/s^2)	2.1157	6.6616	6.6616

CHAPTER 6

CONCLUSIONS

In this research, an innovative MR secondary suspension with emulated positive/negative stiffness dynamics is developed, with an aim to enhance the passenger ride comfort of the high-speed trains. The MR dampers are installed within the secondary suspension in the lateral direction, accounting for the augmented or diminished negative stiffness and energy dissipation. The research work was focused on (i) conducting the full-scale demonstration experiments on the MR secondary suspension, (ii) formulating the direct and inverse dynamic model for the devised MR damper, and (iii) numerically demonstrating the effectiveness of the proposed MR suspension on vehicle body vibration attenuation. The findings and conclusions of this research are summarized as follows.

(1) Full-scale demonstration experiments on MR secondary suspension

Two types of MR dampers (type-A and type-B) in different control ranges were designed, manufactured, and incorporated into the EMU secondary suspension of a high-speed train CRH3. The integrated train vehicle was tested on a roller rig to demonstrate the feasibility of the MR secondary suspension. For System A, the whole vehicle generally vibrated significantly. The type-A MR dampers probably worked in pre-yield region, since it performed like a spring element, rather than an energy dissipative component. For System B, the energy transmission among several frequency component oscillations was observed. The suppression of the low-frequency motions is significantly beneficial for passenger ride comfort enhancement.

To conclude, the full-scale demonstration verified the operational feasibility of the MR secondary suspension for high-speed trains. However, the control range of the MR damper needs to be refined.

(2) Modeling of MR damper dynamics

A new type of MR damper with damper force and displacement sensing was designed and manufactured. The damper can generate softer damping than that of type-A damper so as to be more capable of energy dissipation, and larger control force than that of type-B damper so as to be more competitive for high-speed operation. The minute examination on the damper dynamics, such as post-yield viscosity, yield force, force-velocity hysteresis width and inclination, indicated dependence on current input, as well as amplitude and frequency. Therefore, a current-amplitude-frequency dependent visco-elastic plastic model was proposed to forward dynamics representation. The simplified representation was derived ignoring the MR effect on the hysteresis width. The inverse model was obtained by analytically solving the simplified model.

Numerical simulation demonstrated the accuracy of the proposed direct model to predict the input/output relationship of the MR damper. However, there were inadequacies in low velocities when tracking the damper force, due to the assumption that the hysteresis width in force-velocity relationship remained unchanged with different current levels.

(3) Numerical simulation of MR suspension with emulated stiffness dynamics

The emulated positive or negative stiffness dynamics were incorporated into secondary suspension for a CRH3 EMU. The motions of the railway vehicle were represented by a fifteen-degrees-of-freedom multi-body model. The model consisted of a car body portrayed by lateral translation, yaw and rolling, two trucks by lateral translation and yaw, and four wheelsets by lateral translation and yaw. Numerical simulations investigated four types of suspensions, that is, passive-off suspension, passive-on suspension, semi-active skyhook suspension (equivalently negative stiff superimposed with viscous damping), and suspension with emulated negative stiffness superimposed with friction damping. The simulation results showed that, the fourth suspension outperformed the other three in reducing the lateral vibrations of the vehicle body. However, it also generates more vibrations in bogie than the other three suspensions. It is reasonable since the damper forces to car body and to bogie are a pair of action and reaction. A decrease in car body vibrations would cause an increase in bogie vibrations.

The introduction of the emulated dynamics would largely simplify the control implementation. In other words, the developed semi-active suspension was controlled to essentially vary its system characteristics, e.g. stiffness, according to the feedback within the vehicle system.

REFERENCES

Ai, H. X., Wang, D. H. and Liao, W. H. (2006), "Design and modeling of a magnetorheological valve with both annular and radial flow paths", *Journal of Intelligent Material Systems and Structures*, **17**(4), 327-334.

Aguirre, N., Ikhouane, F., Rodellar, J., Wagg, D. J. and Neild, S. A. (2010), "Viscous Dahl model for MR damper characterization: A real-time hybrid test (RTHT) validation", *Proceeding of 14th European Conference on Earthquake Engineering*, Ohrid, Republic of Macedonia.

Aguirre, N., Ikhouane, F., Rodellar, J. and Christenson, R. (2012), "Parametric identification of the Dahl model for large scale MR dampers", *Structural Control and Monitoring*, **19**(3), 332-347.

Ahn, K. K., Truong, D. Q. and Islam, M. A. (2009), "Modeling of a magnetorheological fluid damper using a self-tuning fuzzy mechanism", *Journal of Mechanical Science and Technology*, **23**(5), 1485-1499.

Aknin, P., Ayasse, J. B. and Devallez, A. (1991), "Active steering of railway vehicle wheelsets", *12th IAVSD Conference, Lyon*.

Aly, A. M., Zasso, A. and Resta, F. (2010), "On the dynamics of a very slender building under wind: response reduction using MR dampers with level mechanism", *The Structural Design of Tall and Special Building*, **20**(5), 539-551.

Ang, W. L., Li, W. H. and Du, H. (2004), "Experimental and modeling approaches of a MR damper performance under harmonic loading", *Journal of the Institute of Engineering*, **44**, 1-44.

Ashour, O., Rogers, C. A. and Kordonsky, W. (1996), "Magnetorheological fluids: materials, characterization and devices", *Journal of Intelligent Material Systems and Structures*, **7**, 123-130.

Askari, M. and Markazi, A. H. D. (2010), "A new evolving compact optimized Tagagi-Sugeno fuzzy model and its application to nonlinear system identification", *International Journal of System Science*, **43**(4), 776-785.

Bahar, A., Pozo, F., Acho, L., Rodellar, J. and Barbat, A. (2009), "Semiactive control of base-isolated structures using a new inverse model of MR dampers", *Proceedings of Europe Control Conference*, **88**(78), 1065-1070.

Bakar, S. A. A., Jamaluddin, H., Rahman, R. A., Samin, P. M., Jamaluddin, H., Rahman, R., Masuda, R., Hashimoto, H. and Inaba, T. (2011a), "Fuzzy semi-active damping force estimator (fSADE) and skyhook semi-active suspension systems", *Internation Journal of Vehicle Systems Modelling and Testing*, **6**(3-4), 232-249.

Bakar, S. A. A., Jamaluddin, H., Rahman, R. A., Samin, P. M., Jamaluddin, H., Rahman, R., Masuda, R., Hashimoto, H. and Inaba, T. (2011b), "Modeling of magnetorheological semi-active suspension system controlled by semi-active damping force estimator", *International Journal of Computer Applications in Technology*, **42**(1), 49-64.

Bai, X. X., Chen, P. and Qian, L. J. (2015), “Principle and validation of modified hysteretic models for magnetorheological dampers”, *Smart Materials and Structures*, **24**(8), 085014.

Bass, B. J. and Christenson, R. E. (2007), “System identification of a 200 kN magnetorheological fluid damper for structural control in large-scaled smart structures”, *Proceeding of American Control Conference*, 2690-2695.

Bhowmik, S., Weber, F. and Hogsberg, J. (2013), “Experimental calibration of forward and inverse neural networks for rotary type magnetorheological damper”, *Structural Engineering and Mechanics*, **46**(5), 673-693.

Bouc, R. (1971), “Mathematical model for hysteresis”, *Acustica*, **24**, 16-25.

Briginshaw, D. (2000), “AGV: The next generation – high speed trains”, *International Railway Journal*, **5**, 16.

Bruni, S., Goodall, R., Mei, T. X. and Tsunashima, H. (2007), “Control and monitoring for railway vehicle dynamics”, *Vehicle System Dynamics: International Journal of Vehicle Mechanics and Mobility*, **45**(7-8), 743-779.

Canudas-de-Wit, C., Olsson, H. Astrom, K. L. and Lischinsky, P. (1995), “A new model for control of systems with friction”, *IEEE Transactions on Automatic Control*, **40**(3), 419-425.

Carlson, J. D. and Jolly, M. R. (2000), “MR fluid, foam and elastomer devices”, *Mechatronics*, **10**(4-5), 555-569.

Carlson, J. D. and Weiss, K. D. (1994), “A growing attraction to magnetic fluids”, *Machine Design*, **8**, 61-64.

Carlson, J. D., Catanzarite, D. M. and Clair, K. A. St. (1996), "Commercial magneto-rheological fluid devices", *International Journal of Modern Physics B*, **10**(23-24), 2857-2865.

Carrella, A., Brennan, M. J. and Waters, T. P. (2007), "Optimization of a quasi-zero-stiffness isolator", *Journal of Mechanical Science and Technology*, **21**, 946-949.

Carrella, A., Brennan, M. J. and Waters, T. P. (2008), "Demonstrator to show the effects of negative stiffness on the natural frequency of a simple oscillator", *Proceeding of IMechE, Part C: Journal of Mechanical Engineering Science*, **222**, 1189-1192.

Ciocanel, C., Nguyen, T., Elahinia, M., Naganathan, N. G. (2006), "Squeeze-flow mode magnetorheological fluid mount", *Electrorheological Fluids and Magnetorheological suspensions, Proceedings of 10th International Conference on ERMR*, 570-576.

Chang, C. C. and Roschke, P. (1998), "Neural network modeling of a magnetorheological damper", *Journal of Intelligent Material Systems and Structures*, **9**(9), 351-358.

Cheli, F. and Corradi, R. (2011), "On rail vehicle vibrations induced by track unevenness: Analysis of the excitation mechanism", *Journal of Sound and Vibration*, **330**, 3744-3765.

Chen, J. Z. and Liao, W. H. (2010), “Design, testing and control of a magnetorheological actuator for assistive knee braces”, *Smart Materials and Structures*, **19**(3), 035029.

Chen, Z. H., Ni. Y. Q. and Or, S. W. (2015), “Characterization and modeling of a self-sensing MR damper under harmonic loading” *Smart Structures and Systems*, **15**(4), 1103-1120.

Chen, Z. H., Lam, K. H. and Ni, Y. Q. (2016), “Enhanced damping for bridge cables using a self-sensing MR damper”, *Smart Materials and Structures*, **25**(8), 085019.

Choi, S. B., Lee, S. K. and Chang, E. G. (2001a), “Field test results of a semi-active ER suspension system associated with skyhook controller”, *Mechatronics*, **11**, 345-353.

Choi, S. B., Lee, S. K. and Park, Y. P. (2001b), “A hysteresis model for the field-dependent damping force of a magnetorheological damper”, *Journal of Sound and Vibration*, **245**(2), 375-383.

Choi, S. B., Lee, S. K. and Park, Y. P. (2002), “H-infinity control performance of a full-vehicle suspension featuring magnetorheological dampers”, *Vehicle System Dynamics: International Journal of Vehicle Mechanics and Mobility*, **38**(5), 341-360.

Choi, S. B., Nam, M. H. and Lee, B. K. (2000), “Vibration control of a MR seat damper for commercial vehicles”, *Journal of Intelligent Material Systems and Structures*, **11**(12), 936-944.

Choi, Y. T., Cho, J. U. Choi, S. B. and Wereley, N. M. (2005), “Constitutive models of electrorheological and magnetorheological fluids using viscometers”, *Smart Materials and Systems*, **14**, 1025-1036.

Choi, Y. T. and Wereley, N. M. (2009), “Self-powered magnetorheological dampers”, *Journal of Vibration and Acoustics*, **131**(4), 323-329.

Dahl, P. R. (1976), “Solid friction damping of mechanical vibrations”, *AIAA Journal*, **14**(12), 1675-1682.

Diana, G., Bruni, S., Cheli, F. and Resta, F. (2002), “Active control of the running behavior of a railway vehicle: Stability and curving performance”, *Vehicle System Dynamics: International Journal of Vehicle Mechanics and Mobility*, 37(suppl), 157-170.

Dominguez, A., Sedaghati, R. and Stiharu, I. (2006a), “A new dynamic hysteresis model for magnetorheological dampers”, *Smart Materials and Structures*, **15**(5), 1179-1189.

Dominguez, A., Sedaghati, R. and Stiharu, I. (2006b), “Semi-active vibration control of adaptive structures using magnetorheological dampers”, *AIAA Journal*, **44**(7), 1563-1571.

Dominguez, A., Sedaghati, R. and Stiharu, I. (2008), “Modeling and application of MR dampers in semi-adaptive structures”, *Computers and Structures*, **86**(3), 407-415.

Du, H., Lam, J. and Zhang, N. (2006), “Modeling of a magnetorheological damper by evolving radial basis function networks”, *Engineering Applications of Artificial Intelligence*, **19**(8), 869- 881.

Du, H. and Zhang, N. (2008), "Application of evolving Takagi-Sugeno fuzzy model to nonlinear system identification", *Applied Soft Computing*, **8**(1), 676-686.

Dyke, S. J., Spencer, B. F., Sain, M. K. and Carlson, J. D. (1996), "Modeling and control of magnetorheological dampers for seismic response reduction", *Smart Materials and Structures*, **5**(5), 565-575.

Eslaminasab, N., Biglarbegian, M., Melek, W. W. and Golnaraghi, F. (2007), "A neural network based fuzzy control approach to improve ride comfort and road handling of heavy vehicles using semi-active dampers", *Int. J. Vehicle Systems*, **14**(2), 135-157.

Fulcher, B. A., Shahan, D. W., Haberman, M. R., Seepersad, C. C. and Wilson, P. S. (2014), "Analytical and experimental investigation of buckled beams as negative stiffness elements for passive vibration and shock isolation systems", *Journal of Vibration and Acoustics*, 136, 031009(12pp).

Gamota, D. R. and Filisko, F. E. (1991), "Dynamic mechanical studies of electrorheological materials: moderate frequencies", *Journal of Rheology*, **35**(3), 399-425.

Gao, F., Liu, Y. N. and Liao, W. H. (2017), "Optimal design of a magnetorheological damper used in smart prosthetic knees", *Smart Materials and Structures*, **26**, 035034.

Goodall, R. M. and Brown, S. (2001), "Tilt technology still evolving as the cost falls", *Railway Gazette International*, **157**(8), 521-525.

Goodall, R. M., Williams, R. A., Lawton, A. and Harborough, P. R. (1981), "Railway vehicle active suspensions in theory and practice", *Vehicle System Dynamics: International Journal of Vehicle Mechanics and Mobility*, **10**(2-3), 210-215.

Gopala Rao, L. V. V. and Narayanan, S. (2008), "Preview control of random response of a half-car vehicle model traversing rough road", *Journal of Sound and Vibration*, **310**, 352-365.

Gordaninejad, F., Saiidi, M., Hansen, B. C., Ericksen, E. O. and Chang, F. K. (2002), "Magnetorheological fluid dampers for control of bridges", *Journal of Intelligent Material System and Structures*, **13**(2-3), 167-180.

Gretzschel, M. and Bose, L. (1999), "A mechatronic approach for active influence on railway vehicle running behavior", *Vehicle System Dynamics: International Journal of Vehicle Mechanics and Mobility*, **33**(suppl), 418-430.

Gretzschel, M. and Bose, L. (2002), "A new concept for integrated guidance and drive of railway running gears", *Control Engineering Practice*, **10**, 1013-1021.

Guglielmino, E. (2005), "Conventional and non-conventional smart damping systems for ride control", *International Journal of Autonomous Systems*, **3**(2-4), 216-229.

Guo, S., Yang, S. and Pan, C. (2006), "Dynamic modeling of magnetorheological damper behaviors", *Journal of Intelligent Material Systems and Structures*, **17**(1), 3-14.

Hauser, G. (2006), "Anticipative tilt control", *Le Rail 4th Conference*, Paris, France.

Heo, S. J. and Park, K. (2000), "Performance and design consideration for continuously controlled semi-active suspension systems", *International Journal of Vehicle Design*, **23**(3-4), 376-389.

Herr, H. and Wilkenfeld, A. (2003), "User-adaptive control of a magnetorheological prosthetic knee", *Industrial Robot*, **30**(1), 42-55.

Hirani, H. and Manjunatha, C. S. (2007), "Performance evaluation of a magnetorheological fluid variable valve", *Journal of Automobile Engineering*, **221**(1), 83-93.

Hong, S. R., Werely, N. M., Choi, Y. T. and Choi, S. B. (2008), "Analytical and experimental validation of a nondimensional Bingham model of mixed-mode magnetorheological dampers", *Journal of Sound and Vibration*, **312**, 399-417.

Hogsberg, J. (2011), "The role of negative stiffness in semi-active control of magnetorheological dampers", *Structural Control and Health Monitoring*, **18**, 289-304.

Iemura, H. and Pradono, M. H.(2005), "Simple algorithm for semi-active seismic response control of cable-stayed bridges", *Earthquake Engineering and Structural Dynamics*, **34**, 409-423.

Iemura, H. and Pradono, M. H. (2009), "Advances in the development of pseudo-negative-stiffness dampers for seismic response control", *Structural Control and Health Monitoring*, **16**, 784-799.

Iemura, H., Toyooka, A., Kouciyama, O., and Higuchi, M. (2008), "Seismic response control with innovative negative stiffness dampers", *The 14th World Conference on Earthquake Engineering*, Beijing, China.

Ikhouane, F. and Dyke, S. J. (2007), "Modeling and identification of a shear mode magnetorheological damper", *Smart Materials and Structures*, **16**(3), 605-616.

Ismail, M., Ikhouane, F. and Rodellar, J. (2009), "The hysteretic Bouc-Wen model, a survey", *Archives of Computational Methods in Engineering*, **16**(2), 161-188.

Iwnicki, S. (2006), *Handbook of Railway Vehicle Dynamics*, Taylor and Francis.

Jakob, J. (2007), "FlexCompact – versatile, reliable and durable", *European Railway Review*, 13(2), 89-93.

Jiang, J. Z., Matamoros-Sanchez, A. Z., Goodall, R. M., and Smith, M. C. (2012), "Passive suspensions incorporating inerters for railway vehicle", *Vehicle System Dynamics: International Journal of Vehicle Mechanics and Mobility*, **50**(suppl), 263-276.

Jiang, Z. and Christenson, R. E. (2012), "A fully dynamic magnetorheological fluid damper model", *Smart Materials and Structures*, **12**(6), 65002-65013.

Jimenez, R. and Alvarez-Icaza, L. (2005), "LuGre friction model for a magnetorheological damper", *Structural Control and Health Monitoring*, **12**(1), 91-116.

Jolly, M. R., Bender, J. W. and Carlson, J. D. (1999), "Properties and applications of commercial magnetorheological fluids", *Journal of Intelligent Material Systems and Structures*, **10**(5), 5-13.

Kamath, G. M. and Wereley, N. M. (1997), “A nonlinear viscoelastic-plastic model for electrorheological fluids”, *Smart Materials and Structures*, 6, 351-359.

Karnopp, D. C., Croby, M. J. and Harwood, R. A. (1974), “Vibration control using semi-active force generators”, *Journal of Engineering for Industry*, **92**(2), 619-626.

Karakoc, K., Park, E. J. and Suleman, A. (2008), “Design considerations for an automotive magnetorheological brake”, *Mechatronics*, **18**, 434-447.

Kavlicoglu, N. C., Kavlicoglu, B. M., Liu, Y. M., Evrensel, C. A., Fuchs, A., Korol, G. and Gordaninejad, F. (2007), “Response time and performance of a high-torque magnetorheological fluid limited slip differential clutch”, *Smart Materials and Structures*, **16**, 149-159.

Kelso, S. P. and Gordaninejad, F. (1999), “Magnetorheological fluid shock absorbers for off-highway high-payload vehicles”, *Smart Structures and Materials: Passive Damping and Isolation, Proceedings of SPIE*, **3672**, 44-54.

Kwok, N. M., Ha, Q. P., Nguyen, T. H., Li, J. and Smali, B. (2006), “A novel hysteresis model for magnetorheological fluid dampers and parameter identification using particle swarm optimization”, *Sensors Actuators A*, **132**, 441-451.

Le, T. D. and Ahn, K. K. (2011), “A vibration isolation system in low frequency excitation region using negative stiffness structure for vehicle seat”, *Journal of Sound and Vibration*, 330, 6311-6335.

Le, T. D. and Ahn, K. K. (2013), “Experimental investigation of a vibration isolation system using negative stiffness structure”, *International Journal of Mechanical Sciences*, 70, 99-112.

Le, T. D. and Ahn, K. K. (2014), "Active pneumatic vibration isolation system using negative stiffness structures for a vehicle seat", *Journal of Sound and Vibration*, 333, 1245-1268.

Li, W. H. and Du, H. (2003), "Design and experimental evaluation of a magnetorheological brake", *International Journal of Advanced Manufacturing Technology*, **27**(7), 508-515.

Li, W. H., Yao, G. Z., Chen, G., Yeo, S. H. and Yap, F. F. (2000), "Testing and steady state modeling of a linear MR damper under sinusoidal loading", *Smart Materials and Structures*, **9**(1), 95-102.

Li, Z. J., Ni, Y. Q., Dai, H. Y. and Ye, S. Q. (2013), "Viscoelastic plastic continuous physical model of a magnetorheological damper applied in the high speed train", *China Science: Technological Science*, **56**(10), 2433-2446.

Lischisky, P., Canudas-de-Wit, C. and Morel, G. (1999), "Friction compensation for an industrial hydraulic robot", *IEEE Control Systems*, **19**(1), 25-32.

Liu-Henke, X., Luckel, J. and Jaker, K. P. (2002), "An active suspension/tilt system for mechatronic railway carriage", *Control Engineering Practice*, **10**(9), 991-998.

Loh, C. H., Lynch, J. P., Lu, K. C. and Wang, Y. (2007), "Experimental verification of a wireless sensing and control system for structural control using MR dampers", *Earthquake Engineering and Structural Dynamics*, **36**(10), 1303-1328.

Mastinu, G. R. M. and Gobbi, M. (2001), "On the optimal design of railway passenger vehicles", *Journal of Rail and Rapid Transit*, **215**, 111-124.

Mei, T. X. and Goodall, R. M. (1999), "Wheelset control strategies for a two-axle railway vehicle", *Vehicle System Dynamics: International Journal of Vehicle Mechanics and Mobility*, **33**(supp), 653-664.

Metered, H. (2012), "Application of nonparametric magnetorheological damper model in vehicle semi-active suspension system", *SAE International Journal of Passenger Cars – Mechanical Systems*, **5**(1), 715-726.

Metered, H., Bonello, P. and Oyadiji, S. (2009), "Nonparametric identification modeling of magnetorheological damper using Chebyshev polynomials fits", *SAE International Journal of Passenger Cars – Mechanical Systems*, **2**(1), 1125-1135.

Metered, H., Bonello, P. and Oyadiji, S. (2010), "The experimental identification of magnetorheological dampers and evaluation of their controllers", *Mechanical Systems and Signal Processing*, **24**(4), 976-994.

Metin, M. and Guclu, R. (2010), "Active vibration control with comparative algorithms of half rail vehicle model under various track irregularities", *Journal of Vibration and Control*, **17**(10), 1525-1539.

Orvnas, A., Stichel, S. and Persson, R. (2011), "Active lateral secondary suspension with H-infinity control to improve ride comfort: simulation on a full-scale model", *Vehicle System Dynamics: International Journal of Vehicle Mechanics and Mobility*, **49**(9), 1409-1422.

Pang, L., Kamath, G. M. and Wereley, N. M. (1998), "Analysis and testing of a linear stroke magnetorheological damper", *Proceeding of 39th*

AIAA/ASME/ASCE/AHS/ASC Structure, Structural Dynamics, and Material Conference and Exhibit, 2841-2856.

Persson, R., Goodall, R. M. and Sasak, K. (2009), "Carbody tilting – technologies and benefits", *Vehicle System Dynamics: International Journal of Vehicle Mechanics and Mobility*, 47, 949-981.

Qian, L. J., Liu, B., Chen, P. and Bai, X. X. (2016), "An inverse model for magnetorheological dampers based on a restructured phenomenological model", *Proceeding of SPIE, Active and Passive Smart Structures and Integrated Systems*, **9799**, 97993H1-8.

Rabinow, J. (1948), "The magnetic fluid clutch", *AIEE Transactions*, **67**, 1308-1315.

Reader, D., Southward, S. C. and Ahmadian, M. (2006), "Nonlinear MR model inversion for semi-active control enhancement", *Proceeding of SPIE, Active and Passive Smart Structures and Integrated Systems*, **7288**, 1-12.

Rodriguez, A., Pozo, F., Bahar, A., Acho, L., Vidal, Y. and Rodellar, J. (2012), "Force-derivative feedback semi-active control of base-isolated building using large-scale MR dampers", *Structural Control and Health Monitoring*, **19**(1), 120-145.

Sakai, C., Ohmori, H. and Sano, A. (2003), "Modeling of MR damper with hysteresis for adaptive vibration control", *Proceeding of 42nd IEEE Conference on Decision and Control*, **4**, 3840-3845.

Shieh, N. C., Lin, C. L., Lin, Y. C. and Liang, K. Z. (2005), "Optimal design for passive suspension of a light rail vehicle using constrained multiobjective evolutionary search", *Journal of Sound and Vibration*, **285**, 407-424.

Shin, Y. J., You, W. H., Hur, H. M. and Park, J. H. (2014), "H8 control of railway vehicle suspension with MR damper using scaled roller rig", *Smart Materials and Structures*, **23**(9), 095023.

Sezer, S. and Atalay, A. E. (2011a), "Dynamic modeling and fuzzy logic control of vibrations of a railway vehicle for different track irregularities", *Simulation Modelling Practice and Theory*, **19**, 1873-1894.

Sezer, S. and Atalay, A. E. (2011b), "Application of fuzzy logic based control algorithms on a railway vehicle considering random track irregularities", *Journal of Vibration and control*, **18**(8), 1177-1198.

Shen, G. and Goodall, R. M. (1997), "Active yaw relaxation for improved bogie performance", *Vehicle System Dynamics: International Journal of Vehicle Mechanics and Mobility*, **28**, 273-289.

Shinoda, N., Murakami, T., Toyama, H., Oomori, Y., Negoro, S., Koizumi, S., Matsui, T. and Osakada, J. (2003), "Tilt control system for railway vehicles using airsprings", *International Symposium on Speed-up and Service Technology for Railway and Maglev Systems*, 24-28.

Simon, D. and Ahmadian, M. (2001), "Vehicle evaluation of the performance of magnetorheological dampers for heavey truck suspensions", *Journal of Vibration and Acoustics*, **123**(7), 365-375.

Song, X., Ahmadian, M. and Southward, S. C. (2005), "Modeling magnetorheological dampers with application of nonparametric approach", *Journal of Intelligent Material Systems and Structures*, **16**(5), 421-432.

Spencer, B. F. Jr., Dyke, S. J., Sain, M. K. and Carlson, J. D. (1997), "Phenomenological model of a magnetorheological damper", *Journal of Engineering Mechanics*, **123**, 230-238.

Stanway, R., Sproston, J. L. and Stevens N. G. (1987), "Nonlinear modeling of an electrorheological vibration damper", *Journal of Electrostatics*, **20**, 167-184.

Stanway, R., Sproston, J. L. and El-Wahed, A. K. (1996), "Applications of electrorheological fluids in vibration control: a survey", *Smart Materials and Structures*, **5**, 464-482.

Stribersky, A., Kienberger, A., Wagner, G. and Muller, H. (1998), "Design and Evaluation of a semi-active damping system for rail vehicles", *Vehicle System Dynamics: International Journal of Vehicle Mechanics and Mobility*, **28**(supp), 669-681.

Snyder, R. A., Kamath, G. M. and Wereley, N. M. (2001), "Characterization and analysis of magnetorheological damper behavior under sinusoidal loading", *AIAA Journal*, **39**, 1240-1253.

Sugahara, Y., Takigami, T., Kazato, A., Koganei, R. and Sampei, M. (2008), "Suppression of vertical vibration in railway vehicles by damping force control of primary suspension using an LQG controller", *Journal of System Design and Dynamics*, **2**(1), 251-262.

Sugahara, Y., Watanabe, N., TakiGami, T. and Koganei, R. (2011), "Vertical vibration suppression system for railway vehicles based on primary suspension damping control – System development and vehicle running test results", *Quarterly Report of RTRI*, **52**(1), 13-19.

Sun. S., Deng, H., Li, W., Du, H., Ni, Y. Q., Zhang, J. and Yang, J. (2013), "Improving the critical speeds of high-speed trains using magnetorheological technology", *Smart Materials and Systems*, **22**, 115012.

Tanifuji, K., Sato, T. and Goodall, R. M. (2003), "Active steering of a rail vehicle with two-axle bogies based on wheelset motion", *Vehicle System Dynamics: International Journal of Vehicle Mechanics and Mobility*, **39**(4), 309-327.

Terasawa, T., Sakai, C., Ohmori, H. and Sano, A. (2004), "Adaptive identification of MR damper for vibration control", *Proceeding of 43rd IEEE Conference on Decision and Control*, **3**(15), 2297-2303.

Truong, D. Q. and Ahn, K. K. (2010), "Identification and application of black-box model for a self-sensing damping system using a magnetorheological fluid damper", *Sensors and Actuators A Physical*, **161**(1-2), 305-321.

Truong, D. Q. and Ahn, K. K. (2011), "Nonlinear black-box models and force-sensorless damping control for damping systems using magnetorheological fluid dampers", *Sensors and Actuators A Physical*, **167**(2), 556-573.

Tsang, H. H., Su, R. K. L. and Chandler, A. M. (2006), "Simplified inverse dynamics models for MR fluid dampers", *Engineering Structures*, **28**, 327-341.

Tsouroukdissian, A. R., Ikhouane, F., Roddellar, J., and Luo, N. (2009), "Modeling and identification of a small scale magnetorheological damper", *Journal of Intelligent Material Systems and Structures*, **20**(7), 825-835.

Tu, J. W., Qu, W. L. and Chen, J. (2011), "Design and fabrication of 500 kN large-scale MR damper", *Journal of Intelligent Material Systems and Structures*, **20**(5), 475-487.

Ubaidillah, Hudha, K. and Jamaluddin, H. (2011), "Simulation and experimental evaluation on a skyhook policy-based fuzzy logic control for semi-active suspension system", *International Journal of Structural Engineering*, **2**(3), 243-272.

Von Neumann, J. (1958), "The computer and the brain", *Yale University Press*.

Wang, D. H. and Liao, W. H. (2001), "Neural network modeling and controllers for magnetorheological fluid dampers", *10th IEEE International Conference on Fuzzy Systems*, **3**, 1323-1326.

Wang, D. H. and Liao, W. H. (2003), "Semiactive vibration control of train suspension systems via magnetorheological dampers", *Journal of Intelligent Material Systems and Structures*, **14**, 161-172.

Wang, D. H. and Liao, W. H. (2005), "Modeling and control of magnetorheological fluid dampers using neural networks", *Smart Materials and Structures*, **14**(1), 111-126.

Wang, D. H. and Liao, W. H. (2009a), "Semi-active suspension systems for railway vehicles using magnetorheological dampers. Part I: system integration and modeling”, *Vehicle System Dynamics: International Journal of Vehicle Mechanics and Mobility*, **47**(11), 1305-1325.

Wang, D. H. and Liao, W. H. (2009b), “Semi-active suspension systems for railway vehicles using magnetorheological dampers. Part I: system integration and modeling”, *Vehicle System Dynamics: International Journal of Vehicle Mechanics and Mobility*, **47**(12), 1439-1471.

Wang, D. H. and Liao, W. H. (2011), “Magnetorheological fluid dampers: a review of parametric modelling”, *Smart Materials and Structures*, **20**, 1-34.

Wang, E. R., Ma, X. Q., Rakhela, S. and Su, C. Y. (2003), “Modelling the hysteretic characteristics of a magnetorheological fluid damper”, *Proceedings of the institution of Mechanical Engineers Part D: Journal of Automobile Engineering*, **217**, 537-550.

Wang, J., Meng, G., Feng, N. and Hahn, E. J. (2005a), “Dynamic performance and control of squeeze mode MR fluid damper-rotor system”, *Smart Materials and Structures*, **14**(4), 529-539.

Wang, X. Y., Song, C., Chen, Z. Q., Sun, H. X. and Chen, P. H. (2009), “Test of a MR damper and its modeling using neural network”, *Journal of Vibration and Shock*, **28**(4), 42-46.

Wang, X. and Gordaninejad, F. (1999), “Flow analysis of field-controllable, electro- and magneto-rheological fluids using Herschel-Bulkley model”, *Journal of Intelligent Material Systems and Structures*, **10**, 601-608.

Wang, X. and Gordaninejad, F. (2000), "Study of field-controllable electro- and magneto-reheological fluid dampers in flow mode using Herschel-Bulkley theory", *Smart Structures and Materials Conference, Proceeding SPIE*, **3989**, 232-243.

Weber, F. (2013), "Bouc-Wen model-based real-time force tracking scheme for MR dampers", *Smart Materials and Structures*, **22**, 1-12.

Weber, F. (2014a), "Optimal semi-active vibration absorber for harmonic excitation based on controlled semi-active damper", *Smart Materials and Structures*, **23**, 095033(13pp).

Weber, F. (2014b), "Semi-active vibration absorber based on real-time controlled MR damper", *Mechanical Systems and Signal Processing*, **46**, 272-288.

Weber, F., Bhowmik, S., and Hogsberg, J. (2014), "Extended neural network-based scheme for real-time force tracking with magnetorheolgical dampers", *Structural Control and Health Monitoring*, **21**(2), 225-247.

Weber, F., Boston, C. and Maslanka, M. (2011), "An adaptive tuned mass damper based on the emulation of positive and negative stiffness with an MR damper", *Smart Materials and Structures*, **20**, 015012.

Weiss, K. D. and Dusclos, T. G. (1994), "Controllable fluids: the temperature dependence of post-yield properties", *Proceeding of 4th International Conference on ER Fluids*, 43-59.

Wen, Y. K. (1976), "Method for random vibration of hysteresis systems", *Journal of the Engineering Mechanics Division*, **102**, 249-263.

Wereley, N. M., Pang, L. and Kamath, G. M. (1998), “Idealized hysteresis modeling of electrorheological and magnetorheological dampers”, *Journal of Intelligent Material Systems and Structures*, **9**, 642-649.

Wereley, N. M., Cho, J. U., Choi, Y. T. and Choi, S. B. (2008), “Magnetorheological dampers in shear mode”, *Smart Materials and Structures*, **17**(1), 015022;

Wickens, A. H. (1994), “Dynamic stability of articulated and steered railway vehicles guided by lateral displacement feedback”, *Vehicle System Dynamics: International Journal of Vehicle Mechanics and Mobility*, **23**(suppl), 541-553.

Won, J. S. and Sunwoo, M. (2009), “Fuzzy modeling approach to magnetorheological dampers: forward and inverse model”, *Proceeding of the Institution of Mechanical Engineering, Part I: Journal of Systems and Control Engineerig*, **223**(8), 1055-1066.

Yang, G., Spencer, B. F. Jr., Carlson, J. D. ans Sain, M. K. (2002), “Large-scale MR fluid dampers: modeling and dynamic performance considerations”, *Engineering Structures*, **24**, 309-323.

Yang, G., Spencer, B. F. Jr., Jung, H. J. and Carlson, J. D. (2004), “Dynamic modeling of large-scale mangetorheological damper systems for civil engineering applications”, *Journal of Engineering Mechanics*, **130**, 1107-1114.

Yang, J., Sun, S. S., Du, H. P., Li, W. H., Gursel, A. and Deng, H. X. (2014), “A novel magnetorheological elastomer isolator with negative changing stiffness for vibration reduction”, *Smart Materials and Structures*, **23**(10), 105023(11pp).

Yang, Z., Zhang, B., Zhang, J. and Wang, C. (2011), "Research on semi-active control of high-speed railway vehicle based on neural network-PID control", *IEEE 7th International Conference on Natural Computation, Shanghai, China*.

Yoshida, O. and Dyke, S. J. (2004), "Seismic control of a nonlinear benchmark building using smart dampers", *Journal of Engineering Mechanics*, **130**(4), 386-392.

Yoshimura, T., Edokoro, K. and Ananthanarayana, N. (1993), "An active suspension model for rail/vehicle systems with preview and stochastic optimal control", *Journal of Sound and Vibration*, **166**(3), 507-519.

Zamzuri, H., Zolotas, A. C. and Goodall, R. M. (2006), "Intelligent control approaches for tilting railway vehicles", *Vehicle System Dynamics: International Journal of Vehicle Mechanics and Mobility*, **44**, 834-842.

Zhao, N. and Cao, D. Q. (2012), "Semi-active control and its robustness for a bogie model with uncertain parameters", *Proceeding of 1st IWHIR*, **1**, 15-29.

Zhou, Q., Nielsen, S. R. K. and Qu, W. L. (2006), "Semi-active control of three-dimensional vibrations of an inclined sag cable with magnetorheological dampers", *Journal of Sound and Vibration*, **296**(1-2), 1-22.

Zhou, R., Zolotas, A. and Goodall, R. (2011), "Integrated tilt with active lateral secondary suspension control for high-speed railway vehicles", *Mechatronis*, **21**, 1108-1122.

Zong, L. H., Gong, X. L., Guo, C. Y. and Xuan, S. H. (2012), "Inverse neuro-fuzzy MR damper model and its application in vibration control of vehicle suspension system", *Vehicle System Dynamics: International Journal of Vehicle Mechanics and Mobility*, **50**(7), 1025-1041.